Downloaded from orbit.dtu.dk on: Mar 30, 2019

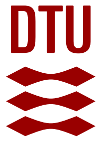

DTU Library

Deposition, Qiaracterization, and Electronic Applications of $YBa_2Cu_3O_7$ Thin Films

Kromann, Rasmus

Publication date:
1992

Document Version
Publisher's PDF, also known as Version of record

Link back to DTU Orbit

Citation (APA):
Kromann, R. (1992). Deposition, Qiaracterization, and Electronic Applications of YBa2Cu307 Thin Films. Roskilde: Risø National Laboratory.

General rights
Copyright and moral rights for the publications made accessible in the public portal are retained by the authors and/or other copyright owners and it is a condition of accessing publications that users recognise and abide by the legal requirements associated with these rights.

- Users may download and print one copy of any publication from the public portal for the purpose of private study or research.
- You may not further distribute the material or use it for any profit-making activity or commercial gain
- You may freely distribute the URL identifying the publication in the public portal

If you believe that this document breaches copyright please contact us providing details, and we will remove access to the work immediately and investigate your claim.

DK9300013

RISØ

Risø-R-642(EN)

Deposition, Characterization, and Electronic Applications of $YBa_2Cu_3O_7$ Thin Films

Rasmus Kromann

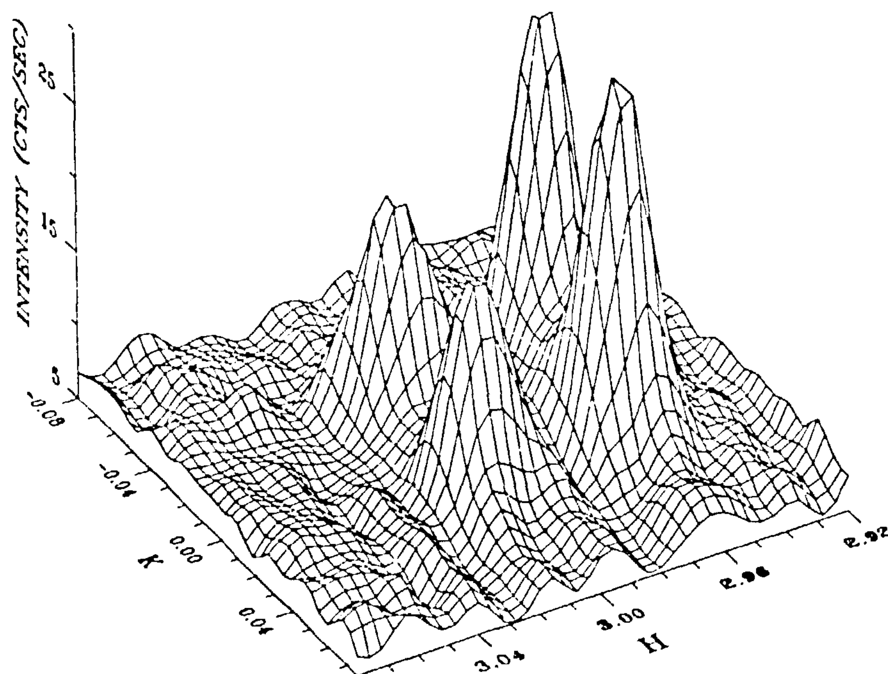

Risø National Laboratory, Roskilde, Denmark
September 1992

Deposition, Characterization, and Electronic Applications of $YBa_2Cu_3O_7$ Thin Films

Risø-R-642(EN)

Rasmus Kromann

Risø National Laboratory, Roskilde, Denmark
September 1992

Abstract

This report contains the results of an experimental study of $YBa_2Cu_3O_7$ thin films. The study involved deposition methods, structural characterization, and application of the thin films for SQUID devices.
Chapter 1 describes the principles of thin film deposition by RF sputtering, followed by an account of the optimization procedure for the YBCO thin films. The sputter system was used in two different configurations. The first of these, a parallel plate geometry with an unheated, rotating substrate table, was abandoned relatively early because of the poor quality of post annealed films as compared to films made by an in-situ technique. The second configuration of the sputter system involved an inverted cylindrical magnetron gun in combination with a heated substrate table. By varying the deposition parameters (such as the deposition temperature and the gas composition) systematically, it was possible to obtain films that were fully superconducting at 77 K and with an X-ray spectrum consisting of essentially only (00*l*) reflections from the 1:2:3 phase of YBCO. The composition of the films were analyzed by EDX and the results showed that the films contained excess Ba. The relatively low T_c is ascribed to this fact. In the last part of Chapter 1 thin film deposition by laser ablation is described. This technique was used for the SQUID devices described in Chapter 3.
Chapter 2 presents the results of an X-ray diffraction study of the structure of laser ablated YBCO thin films. Four films were examined, two of which were deposited on MgO, while the other two were deposited on $SrTiO_3$. The two films on MgO differ by 75 % in the critical current density and this is ascribed to the fact that about 5 % of the grains in the low J_c film grow 45° misoriented with respect to the dominant orientation in the a-b plane. The low J_c film also has a higher density of small-angle grain boundaries as evidenced by transmission electron microscopy. The two films on $SrTiO_3$ differ by 70 % in J_c and this is ascribed to the presence of 8.3 % a-axis oriented material in the low J_c film as compared to only 0.6 % in the high J_c film. In general, the critical current density is higher in the films on $SrTiO_3$ than in the films on MgO and this is attributed to the closer lattice match between $SrTiO_3$ and YBCO.

(continued on next page)

ISBN 87-550-1827-0
ISSN 0106-2840

Grafisk Service, Risø, 1992

Chapter 3 contains the results of the effort to fabricate SQUIDs and magnetometers based on YBCO thin films. Various ways of achieving a 45° grain boundary by a bi-epitaxial process on MgO substrates are described. A detailed account of the optimization of the deposition of the chosen sequence of thin film layers is given. It is demonstrated that the SQUIDs exhibit critical current modulation in a magnetic field at temperatures up to 80 K. The spectral density of the noise in the SQUIDs is measured both in the flux locked loop mode of operation and by double modulation. It is shown that the 1/f noise can be reduced by a factor of 3 by the double modulation technique, indicating that the dominant contribution to the 1/f noise comes from critical current fluctuations. Subsequently, a bi-epitaxial process to create 45° grain boundaries on YSZ substrates is described. SQUIDs based on these junctions exhibit critical current modulation up to 77 K. The noise level in these devices is found to be comparable to the noise level in SQUIDs on MgO substrates. The high level of 1/f noise from critical current fluctuations is ascribed to the nature of the 45° grain boundary and it is argued that it is necessary to develop a bi-epitaxial process for grain boundaries with angles less than 45° in order to improve the noise properties of these devices. In the last part of Chapter 3 it is demonstrated that a SQUID and a flux transformer can be fabricated on the same substrate to form an integrated magnetometer. These devices exhibit critical current modulation at temperatures up to 73 K, and the flux transformer enhances the sensitivity of these devices by a factor of about 50 as compared to the SQUID alone.

This report is submitted in partial fulfillment of the requirements for a Ph.D. degree at Physics Laboratory I at the Technical University of Denmark. The supervisors were Dr. N.H. Andersen at Risø National Laboratory and Dr. Jørn Bindslev Hansen and Dr. Claus Schelde Jacobsen at the Technical University of Denmark.

Dansk resumé

Denne rapport indeholder resultaterne af et eksperimentelt studie af $YBa_2Cu_3O_7$ tyndfilm. Studiet omhandler deponeringsmetoder, strukturel karakterisering og anvendelse af tyndfilmene til fremstilling af SQUIDs.
I Kapitel 1 gennemgås pricipperne i tyndfilm deponering ved hjælp af RF sputtering, efterfulgt af en gennemgang af optimeringsproceduren for deponering af YBCO tyndfilm. Sputter anlægget blev anvendt i to forskellige konfigurationer. Den første af disse, en parallel plade geometri med et uopvarmet, roterende substratbord, blev opgivet relativt hurtigt på grund af den dårlige kvalitet af film fremstillet ved højtemperatur rekrystallisering i sammenligning ved film fremstillet ved en in-situ teknik (d.v.s. deponeret på opvarmede substrater). Den anden konfiguration af sputter anlægget bestod af en inverteret cylindrisk magnetron samt et opvarmet substratbord. Ved at variere deponeringsparametrene systematisk lykkedes det at fremstille film, der var fuldt superledende ved 77 K og med et røntgen spektrum bestående praktisk taget udelukkende af (00*l*) refleksioner fra 1:2:3 fasen af YBCO. Sammensætningen af filmene blev analyseret med EDX, hvorved det blev konstateret, at filmene indeholder overskydende Ba. Den relative lave kritiske temperatur tilskrives dette forhold. I den sidste del af Kapitel 1 beskrives tyndfilm deponering ved hjælp af laser ablation. Denne teknik blev brugt ved fremstillingen af SQUIDs som beskrevet i Kapitel 3.
I Kapitel 2 præsenteres resultaterne af en undersøgelse af strukturen i laser ablerede YBCO tyndfilm ved hjælp af røntgen diffraktion. Fire film blev undersøgt, hvoraf de to var deponeret på MgO mens de to andre var deponeret på $SrTiO_3$. De to film på MgO substrater udviser en forskel på 75 % i den kritiske strømtæthed. Dette tilskrives at ca. 5 % af kornene i filmen med den lave strømtæthed vokser 45° misorienteret i forhold til den dominerende orientering i a-b planen. Denne film har også en højere tæthed af småvinkel korngrænser. De to film på $SrTiO_3$ substrater udviser en forskel på 70 % i den kritiske strømtæthed. Dette tilskrives tilstedeværelsen af 8.3 % a-akse orienteret materiale i filmen med den lave strømtæthed sammenlignet med kun 0.6 % i filmen med den høje strømtæthed. Generelt er den kritiske strømtæthed højere i filmene på $SrTiO_3$ end i dem på MgO. Dette forhold skyldes, at der er bedre tilpasning mellem krystalstrukturene i YBCO og $SrTiO_3$.
Kapitel 3 indeholder resultaterne af arbejdet med at fremstille SQUIDs og magnetometre baseret på YBCO tyndfilm. Der beskrives forskellige måder at opnå en 45° korngrænse ved en bi-epitaxiel process på MgO substrater. Herefter følger en detaljeret beskrivelse af optimeringen af deponeringsprocessen med den valgte sekvens af tyndfilmslag. Det vises, at disse SQUIDs udviser modulation af den kritiske strøm ved temperaturer op til 80 K. Den spektrale tæthed af støjen i disse SQUIDs måles både ved den såkaldte flux locked loop metode samt ved dobbelt modulation. Det vises, at 1/f støjen kan reduceres med en faktor 3 ved anvendelse af dobbelt modulation. Dette forhold indikerer, at det dominerende bidrag til 1/f støjen kommer fra fluktuationer i den kritiske strøm. Herefter beskrives en bi-epitaxiel process til dannelse af 45°

korngrænser på YSZ substrater. SQUIDs baseret på denne type junctions udviser modulation af den kritiske strøm ved temperaturer op til 77 K. Støjniveauet i disse komponenter viser sig at være sammenlignelig med støjniveauet i SQUIDs på MgO substrater. Det høje niveau af 1/f støjen hidrørende fra fluktuationer i den kritiske strøm tilskrives egenskaberne af korngrænserne på 45° og der argumenteres for, at det er nødvendigt at udvikle en bi-epitaxiel process til dannelse af korngrænser, som er mindre end 45° for at opnå afgørende forbedringer af støjniveauet i disse SQUIDs. I den sidste del af Kapitel 3 vises, at det er muligt at kombinere en SQUID med en flux transformer på samme substrat og derved fremstille et integreret magnetometer. Disse komponenter udviser modulation af den kritiske strøm ved temperaturer op til 73 K. Tilstedeværelsen af flux transformeren forøger følsomheden med en faktor 50 i sammenligning med en SQUID uden flux transformer.

Contents

1 Thin film deposition 9

1.1 Sputtering 9
1.1.1 Conventional sputter systems 9
1.1.2 Sputter systems for high T_c applications 13
1.1.3 Experimental techniques 17
1.1.4 Results of sputtering at Risø 19
1.2 Laser ablation 28
1.2.1 Theory of laser ablation 28
1.2.2 Description of the deposition system at UC Berkeley 30
1.3 Conclusions 32
References 33

2 Structural characterization 35

2.1 Fundamentals of X-ray diffraction 35
2.2 Experimental techniques 39
2.3 Relation between epitaxy and critical current density 42
2.3.1 Influence of structural defects in the film 44
2.3.2 Influence of the substrate 48
2.4 Conclusions 52
References 53

3 SQUIDs and magnetometers 54

3.1 Theory of the DC SQUID 54
3.1.1 Josephson junctions 54
3.1.2 Principle of operation of the SQUID 56
3.1.3 Noise properties 58
3.2 Experimental techniques 62
3.2.1 Patterning of thin films 62
3.2.2 Electrical characterization 64
3.2.3 Structural characterization 65
3.3 SQUIDs fabricated by the bi-epitaxial process 66
3.3.1 SQUIDs on MgO substrates 67
3.3.2 SQUIDs on YSZ substrates 80
3.4 Magnetometers 87
3.5 Conclusions 96
References 98

4 Acknowledgements 101

1 Thin film deposition

The discovery of high temperature superconductivity in 1986 by Bednorz and Müller[1] in the BaLaCuO system was followed by a couple of years of hectic and turbulent activity in many laboratories around the world. This activity lead to the discovery of several new high temperature superconductors; in particular, $YBa_2Cu_3O_7$ (or YBCO for short) with a critical temperature T_c=93 K, was discovered in the beginning of 1987 by Paul Chu et al[2,3]. Because of the potential benefits of operating superconducting electronics in liquid nitrogen instead of in liquid helium, the interest in thin films made from high temperature superconductors was very strong right from the beginning. Several methods have been used for this purpose including sputtering, laser ablation, metal organic chemical vapor deposition and ion beam sputtering. In this chapter we will describe the first two of these methods, i.e. rf sputtering and laser ablation and we will present and discuss some of the results we have obtained.

1.1 Sputtering

Sputtering was already well established as a thin film deposition technique when high T_c superconductivity was discovered. However, it is fair to say that it has undergone significant evolution as a result of the problems encountered in the sputtering of these materials. We will first describe the conventional type of sputter systems and then go on to mention some of the modifications that have been introduced in the context of high T_c superconductors.

1.1.1 Conventional sputter systems

Figure 1.1 shows schematically the construction of a sputter gun in the traditional parallel plate configuration. A sputter target made from the material to be deposited is attached to one of the plates. In the case of dc sputtering a large negative voltage is applied to this plate, which is therefore named the cathode. It is water cooled because most of the energy supplied to the sputter system is dissipated in the target. The other plate, the anode, is usually grounded, and it is used to hold one or more substrates onto which the thin film is deposited. The sputter gun is placed in a vacuum chamber which is pumped out close to its base pressure before deposition and backfilled to a pressure of typically 0.01 mbar of the sputter gas. The sputter gas can in principle be any gas which forms positive ions, but since chemical reactions between the gas and the electrodes (target or substrate) are undesirable, one of the noble gases is usually chosen. Argon, in particular, is widely used because it is relatively cheap.
When an electric voltage is applied to the system shown in Figure 1.1, an electric discharge is ignited. Electrons pick up energy from the electric field, and when they have reached an energy corresponding to the ionization energy of the sputter gas they will be able to ionize a gas atom at their next collision

with one of these (the first ionization potential of argon is 15.8 eV). Thus, the sputter gas will contain both positively and negatively charged particles and consequently, it will behave like a plasma. Without going to much into details we mention that the presence of the plasma has certain consequences for the spatial variation of the electric potential in the space between the electrodes. Because the numbers of positively and negatively charged particles are approximately equal, the potential will be almost constant in the major part of the space between the electrodes. One finds that all of the potential drop lies across the so-called dark space, which is the region extending 1-2 cm out from the cathode. When a positively charged gas atom enters the dark space it will be accelerated towards the cathode and the target. When the ion hits the target, it will interact with a small volume of it and several things can happen. First, the ion can simply be reflected from the target as a neutral atom or as an ion. Second, the ion can become trapped in the target, a process known as ion implantation which is widely used in the semiconductor industry. Third, the impact of the gas ion can cause one or more of the atoms from the target to be released. After it has been released it is free to deposit everywhere in the chamber, including the substrates. This is the desired outcome of the ion impact. Finally, one or more secondary electrons may be released from the target. They will be strongly repelled from the target and go back to the space between the target and the anode, where they will contribute to more ionizing collisions with the atoms of the sputter gas. This is how the electric discharge is sustained.

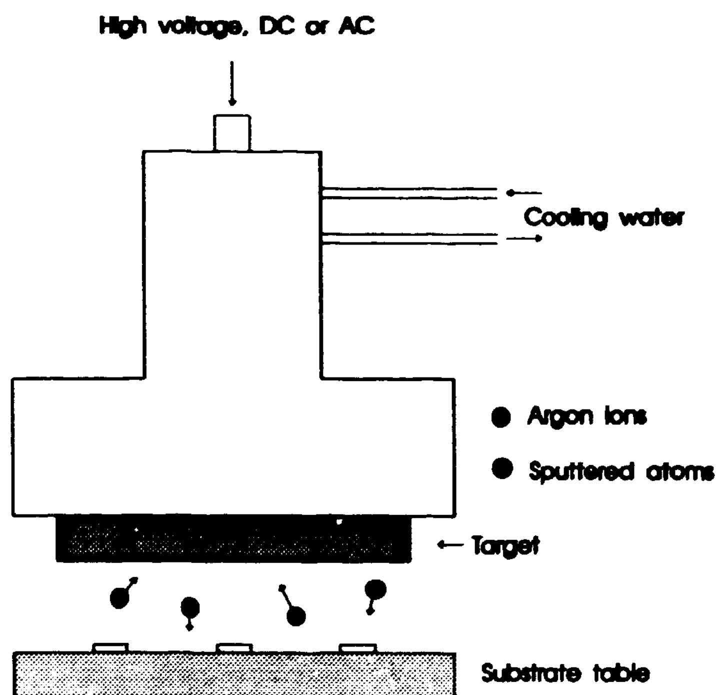

Figure 1.1 This figure shows schematically the construction of a parallel plate sputter gun. The substrate table (in this case shown with three substrates lying on it) is usually grounded.

The key number describing the sputter process is the sputter yield S, defined as the number of atoms released from the target per incident ion. The sputter yield depends on the energy of the incident ions, the binding energy of the atoms in the target, and the atomic masses of the incident ions and the target atoms. In general one finds that S increases with ion energy up to a few keV at which point S becomes more or less constant. For instance, in the case of copper sputtered by argon[4], S increases almost linearly with ion energy, rising from 0 to 3 for ion energies going from 0 to 1 keV. For higher energies the curve becomes flatter, approaching a limiting value of about 9 for energies above 10 keV. It is evident from this discussion of the sputter yield as a function of energy that we do not gain anything by operating the sputter system at voltages above 10 keV. For safety reasons we would like to operate it at as low a voltage as possible, and typical values of the operating voltage lie in the range from 100 V to 1000 V.

Another important parameter of the sputter system is the deposition rate, i.e. the rate at which the thickness of the thin film increases per unit time. The deposition rate depends on the sputtering yield (the more atoms that are released the more will be deposited), the gas pressure, and the sticking coefficient of the sputtered atoms, i.e. the probability that an atom will stick to the substrate. A high gas pressure will cause the sputtered atoms to be scattered in the sputter gas as they cross the distance between the target and the substrate and thus the deposition rate will be reduced. There is also a lower limit on the gas pressure, however, which is set by the fact that the density of gas atoms must be sufficiently large for the electrons to make ionizing collisions with them before they (the electrons) hit the walls of the vacuum chamber. As mentioned earlier, a typical sputter gas pressure is 0.01 mbar.

The deposition rate can also be increased by using a magnetron. The idea is to apply a magnetic field parallel to the surface of the target (in the case of a planar magnetron; other forms of magnetrons exist). The secondary electrons emitted from the target will then be forced to follow a circular path because of the influence of the magnetic field. This means that the electrons will be confined to the region immediately in front of the target. This will in turn cause more ionizing collisions with the sputter gas atoms, because fewer electrons are lost to the anode and the walls of the chamber. The deposition rate is thus increased by increasing the number of ions incident on the target. As an extra benefit of the magnetron arrangement, the bombardment of the substrate by electrons is virtually eliminated. The drawback of using a magnetron is that the discharge becomes spatially inhomogeneous. This means that the target will be eroded at different rates in different places. More seriously, in cases where a multi-component target is used (such as YBCO), the composition of the deposited material will vary across the substrate, reflecting the inhomogeneity of the discharge. The film can be made homogeneous under these circumstances by moving the substrates relative to the target during deposition.

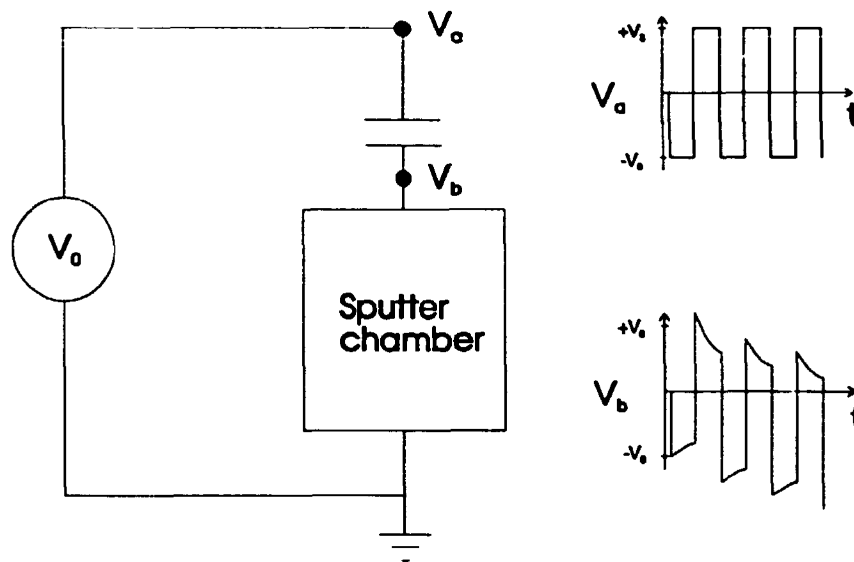

Figure 1.2 The two curves of voltage versus time illustrate how a negative bias voltage develops on the capacitor because of the higher mobility of the electrons compared to the ions.

Until now we have only considered a dc voltage as the power source for the electrical discharge. If we instead use an rf voltage it becomes possible to sputter also insulating materials, because there is no net current flowing in an rf discharge. However, it might at first seem to be impossible to achieve any deposition, because the constant reversal of the polarity would seem to constantly interchange the roles of the electrodes as target and substrate. However, this is not the case. Consider the simple model of the discharge shown in Figure 1.2 with a blocking capacitor inserted between the power supply and the vacuum chamber. This capacitor is normally part of a more complicated matching network consisting of adjustable capacitors and coils and which is used to match the impedance of the discharge to the power supply. Imagine we apply a voltage V_0 in the form of a square wave with frequency f to the sputter system. Because the voltage across the capacitor can not change instantaneously, at time t=0 the voltage at the target V_b drops to $-V_0$. The discharge is initiated and the target is bombarded by positive ions. This will cause the capacitor to charge up and the target voltage will rise slowly towards zero. At the end of the first half-cycle, at t=1/2f, the voltage from the power supply jumps by $2V_0$ to $+V_0$ and this causes the voltage at the target to jump by $2V_0$ also. The target is now positive with respect to ground and the direction of the discharge is reversed. The target will now be bombarded by electrons, and because they have a much higher mobility than the ions, the net current drawn by the target will be much larger during this half-cycle. Consequently, the voltage across the capacitor will change by a much larger amount. The net effect of this is that after a few cycles a negative bias voltage has developed across the capacitor, which will ensure that the net current in the discharge is zero. When the steady state has been reached the magnitude of the bias voltage is only slightly smaller than V_0 with the result that the target is at

a negative potential nearly all the time; it becomes positive only in a small fraction of the period right after the power supply changes from $-V_0$ to $+V_0$. Thus, the target will be bombarded by ions almost continuously and the rf discharge will produce the same effect as the dc discharge.
We conclude our discussion of conventional systems by mentioning that it is possible to apply a small negative bias voltage (rf or dc) to the substrate table. This gives one more adjustable parameter in the deposition process and thus makes it possible to better control the properties of the thin film. A good example is given in Ref. 4 where it is shown how the resistivity of a sputtered gold film varies as a function of the bias voltage. For bias voltages around -40 V the resistivity reaches its minimum value, which corresponds to the bulk value. The effect of bias sputtering is often explained as a resputtering of loosely bonded material by the sputter gas ions, but this does not explain all the observed effects. As a counter example we can mention the oxidation of chromium films in the naturally occurring oxygen in the sputter chamber. This oxidation is reduced under the influence of a substrate bias voltage, even though the chromium-oxygen bond is very strong. Regardless of what the exact mechanism of the bias voltage is, the fact that nearly all film properties can be changed simply by adjusting the bias voltage has been one of the decisive factors for the widespread application of sputtering as a deposition technique.

1.1.2 Sputter systems for high T_c applications

In this section we will describe some of the different approaches to sputtering of high temperature superconductors that have been reported in the literature. Even though they were not invented for this purpose, they have been used much more extensively than before the high T_c materials were discovered.
The earliest reports[5] of sputtered thin films of YBCO appeared only a couple of months after the material was discovered. It is characteristic of these first attempts to sputter deposit YBCO thin films that they were made with sputter system configurations similar to that described in the previous section, i.e. with planar targets in parallel plate configurations and with no intentional substrate heating. At room temperature YBCO grows in an amorphous layer and it is therefore necessary to anneal the films in an oxygen atmosphere after deposition. Most studies suggest that a temperature in the range 800-900 °C is optimum for this purpose[6]. The optimum temperature is determined as a trade off between a temperature high enough that the amorphous to crystalline transformation can take place and be completed in a reasonable time, and a temperature low enough that the film does not react chemically with the substrate material resulting in decomposition of the superconducting phase. The latter problem has been the subject of several studies[7,8]. It is generally found that only MgO and $SrTiO_3$ have sufficiently low reactivity with YBCO to withstand the temperatures required in the post-annealing process without any significant degradation of the YBCO film. For other substrate materials such as Yttrium Stabilized Zirconia (YSZ), sapphire and silicon it is found that a buffer layer is necessary to protect the film and substrate from each other. There is another problem with the films produced by the post-annealing

method. As the temperature approaches the annealing temperature, the transformation to the crystalline phase will be initiated in many places on the substrate, independently of each other. There will not necessarily be any correlation between the film texture and the crystallographic orientation of the substrate at the different nucleation sites, and the film will therefore be polycrystalline in nature with a significant amount of high-angle grain boundaries. As it will be discussed in Chapter 2, such a film will have a strongly reduced critical current density compared to a film without high-angle grain boundaries.
The key to avoid high-angle grain boundaries in the film is to grow it in such a way that the desired crystal structure is present already as the film is deposited. This can be achieved by depositing the film at elevated temperatures in the range 650 °C - 750 °C. However, because oxygen is a constituent of the film material, it must be present at a certain minimum partial pressure to prevent decomposition of the superconductor into simple oxides. Bormann and Nölting[9] have investigated how the required oxygen partial pressure P_{O2} depends on temperature T by using an electrochemical method. They find that P_{O2} decreases linearly with 1/T. In particular, for the practically relevant temperature T=750 °C, P_{O2} should be at least 0.2 mbar to prevent decomposition. When the film is deposited under these conditions, it will grow in the oxygen deficient tetragonal structure, i.e. the oxygen content is close to 6 atoms per unit cell. By cooling off the film slowly (in about 30 min or so) in an oxygen pressure close to 1 atm, the film will take up oxygen to form the superconducting orthorhombic phase with close to 7 oxygen atoms per unit cell. This method of film formation is usually referred to as an in-situ technique. It offers two main advantages over the post-annealing method. First, the highest temperature required at any point in the process is reduced by typically 150 °C, thereby reducing the probability of film/substrate reactions. Second, the film grows virtually as a single crystal with very few high-angle grain boundaries and with a higher critical current density as a result.

Another problem with the high T_c superconductors in the context of sputtering is that the target contains oxygen. This means that also oxygen atoms and, in particular, negatively charged oxygen ions will be released from the target. These ions will be accelerated by passing through the cathode dark space, i.e. they will be accelerated towards the anode, where they will cause parts of the already deposited film material to be resputtered. In order to understand this problem completely it is necessary to consider sputtering from a multi-component target in more detail.
A sintered YBCO target consists of a multitude of randomly oriented single crystals. The target material will in general not be released in molecular form as $YBa_2Cu_3O_7$, but rather as single atoms or simple molecules such as CuO and BaO_2. Since each of the four kinds of atoms in YBCO has different sputter yields at a given Ar ion energy, the atom with the highest sputter yield will be removed from the surface at the highest rate. However, this will lead to a depletion of the surface layer in this particular type of atom and its sputter rate will thus be reduced. Since the different atoms eventually have to leave the

surface in the same ratio as they are supplied to the surface from the interior of the target, it is easy to convince oneself that when the steady state has been reached, the composition of the surface layer has been changed in such a way as to achieve this effect. Consider now the resputtering from the substrate. The same arguments about the different sputter yields of the different kinds of atoms apply as before. However, since there is no interior of the thin film (at least not in the early stages of its formation) there is no compensating mechanism as in the case of sputtering from a target. The resputtering from the substrate will thus simply result in a depletion of the element with the highest sputter yield.

The simplest way to overcome the problem of resputtering is to perform the sputtering in a significantly higher pressure than usual. The idea is that if the mean free path of the oxygen ions is less than the distance between the target and the substrate, then the oxygen ions will undergo a sufficient number of collisions to prevent them from being effective in resputtering of the deposited material. Note, that if a magnetron is used, the electrons are confined to the region immediately in front of the target and most ionizing collisions will take place here. This is why the oxygen ions have to travel several mean free paths to reach the substrate, whereas the Ar ions in general have to travel less than a mean free path to reach the target. The Ar ions will thus still be effective in sputtering the target. This technique has been demonstrated for instance by Li et al[10]. They used a total gas pressure of 0.6 Torr (0.8 mbar) with 33 % O_2 and achieved a reasonable deposition rate of 5 Å/s. Under the best of circumstances the films were fully superconducting at 83 K, with the onset of superconductivity occuring at 90 K. However, this technique does not result in stoichiometrically correct YBCO films as evidenced by the reduced transition temperature and the relative broad transition. Similar results have been obtained by a French group[11] using a total gas pressure in excess of 1 mbar. In that case the deposition rate was significantly lower (only about 300 Å/h).

A more drastic approach to the problem of resputtering is illustrated in Figure 1.3. The substrate table is rotated by 90° and placed along the side of the sputter gun. The idea is to remove the substrates from the path travelled by the oxygen atoms. At low gas pressures (0.01 mbar) the oxygen ions travel essentially in a straight line perpendicular to the target and an arrangement as shown in Figure 1.3 will thus prevent that the majority of the ions hit the substrate. This technique is referred to as off-axis sputtering. It solves the problem of resputtering at the expense of a reduced deposition rate. In one of the first demonstrations of this technique, Eom et al[12] deposited films with transition widths of only 1 K and which were fully superconducting at temperatures up to 87 K. The composition of the films corresponded to that of the target within 5 % as determined by electron microprobe measurements. The deposition rate was typically 0.5 Å/s. The technique has also been demonstrated by a group at IBM[13]. They used an angle of 60° instead of 90° between the target and the substrate. They produced films that were fully superconducting at temperatures up to 89 K and with critical current densities up to 8×10^5 A/cm^2 at 77 K.

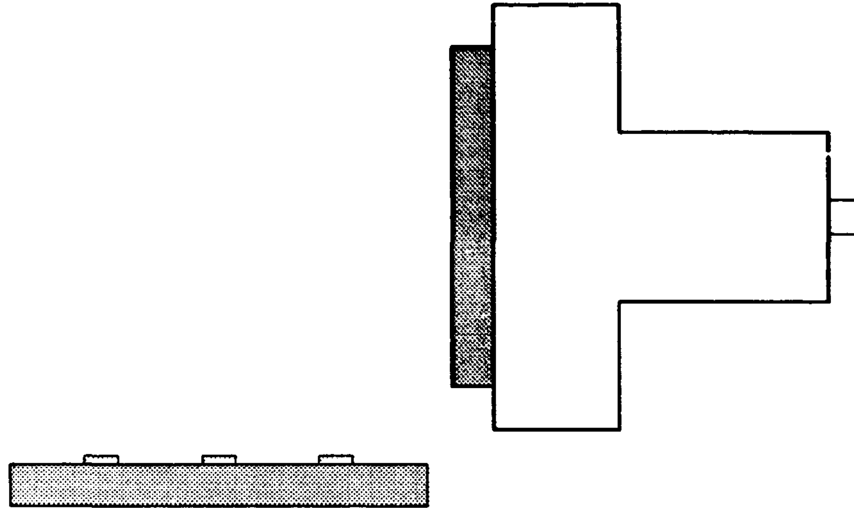

Figure 1.3 In the so-called off-axis technique the substrate table is rotated 90° and placed along the side of the sputter gun.

A variation of the off-axis technique was demonstrated by Gao et al[14]. They placed a reflection plate at an angle of 45° to both the target and the substrate. The purpose of this plate is to direct the beam of sputtered particles towards the substrate. They were able to produce films with transition widths of 3.5 K which were fully superconducting at 89.5 K. They reported a critical current density of 8×10^6 A/cm^2 at 77 K.
The use of two planar targets facing each other (imagine a second sputter gun added at the left end of the substrate table in Figure 1.3) has been reported by a Japanese group. With this system they have deposited films of three different ceramic oxide superconductors: LaSrCuO[15], YBCO[16] and BiSrCaCuO[17]. However, in all three cases the transition width of the film was very broad (27 K in the case of the YBCO films), indicating that the process was not completely under control.
The logical extension of the arrangement with two planar targets facing each other is to use a cylindrical target. The configuration is shown in Figure 1.4. A ring shaped magnet is placed on the outside of the cylinder to achieve the magnetron effect. One end of the cylinder is closed off by a metal plate held at ground potential, while the substrate table is placed at the other end of the cylinder. The electric power is supplied to the target as in the case of a planar target, and the discharge takes place between the end plate and the target. This technique was pioneered in the context of high T_c materials by a German group at Kernforschungszentrum Karlsruhe[18]. They have used this setup in combination with a high sputter gas pressure (0.8 mbar with 33 % O_2) to achieve films that were fully superconducting at 90 K and with critical currents up to 5.5×10^6 A/cm^2 at 77 K on $SrTiO_3$ substrates. These films are among some of the best produced by sputtering anywhere in the world. The use of a cylindrical target has also been reported by an Indian group[19]. However, they did not heat the substrates during deposition and consequently, they had to go through the post-annealing procedure. This is probably the reason that they report a

maximum transition temperature of only 80 K (for the films being fully superconducting).

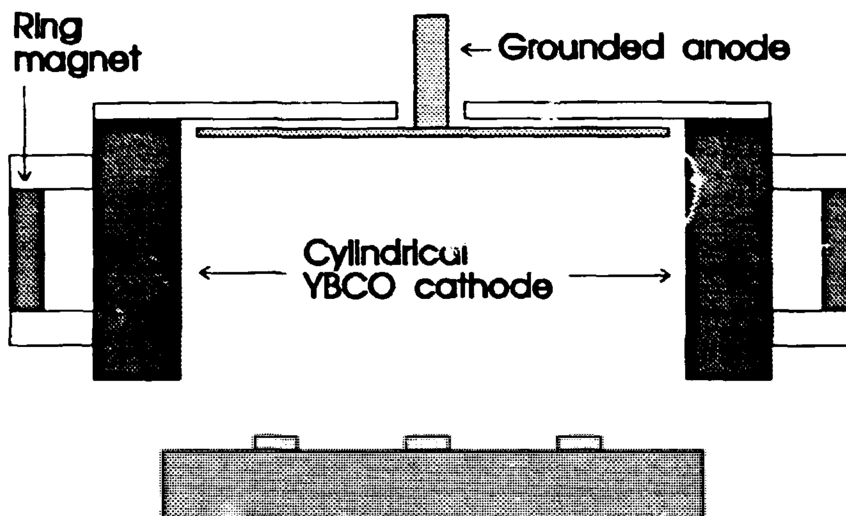

Figure 1.4 This figure shows the physical layout of the inverted cylindrical magnetron using a cylindrical sputter target.

1.1.3 Experimental techniques

For the sputter deposition experiments at Risø we have used a commercial sputter system from Alcatel (model SCM 451). This system comes with four sputter guns in the parallel plate configuration. The substrate table can be moved from one target to another during deposition and it is thus in principle possible to deposit four different materials on top of each other without breaking the vacuum. The power to the discharge is supplied by a Dressler 2 kW RF generator. The system is equipped with a diffusion pump (Alcatel Crystal 160) and a mechanical backing pump (Alcatel type 2033) and has a base pressure of 5×10^{-7} mbar. During deposition both argon and oxygen can be supplied to the system, and the composition of the sputter gas is monitored by a Dataquad mass spectrometer from Spectramass using a quadropole sensor head. We have made a few changes to the system, prompted by the problems encountered in sputtering of high T_c materials. Initially, we were using a planar target with magnetron, and it was therefore necessary to move the substrates relative to the target during deposition. For that purpose we have used a 2 stage rotating substrate table as shown in Figure 1.5. The first stage of the table has a diameter comparable to the diameter of the target (100 mm) and can be rotated in either direction. On top of the first stage there are three smaller secondary stages connected to the first stage by gears such that they always rotate in the opposite direction of the first stage. The center of the first stage is offset by 2 cm relative to the center of the target, since otherwise the substrate table would have no effect (the inhomogeneities introduced by the magnetron are rotationally symmetric around an axis going through the center of the target). Due to the difficulties encountered with the planar target (to be

described in the next section) we have subsequently designed an inverted cylindrical magnetron sputter gun as described in the previous section (Figure 1.4). Our sputter gun differs from the Karlsruhe design in that it is significantly larger, with an inner diameter of about 70 mm compared to 30 mm. Also, because the in-situ method is superior compared to the post-annealing method as far as the quality of the YBCO films is concerned, we have developed a heating stage for the substrate table which allows us to keep the substrates at temperatures up to 800 °C during deposition. The temperature of the substrate table was measured by a thermocouple inserted into the table at a position directly beneath the substrate. The temperature was regulated to within 2 °C by a temperature regulator. The heated substrate table can not be rotated.

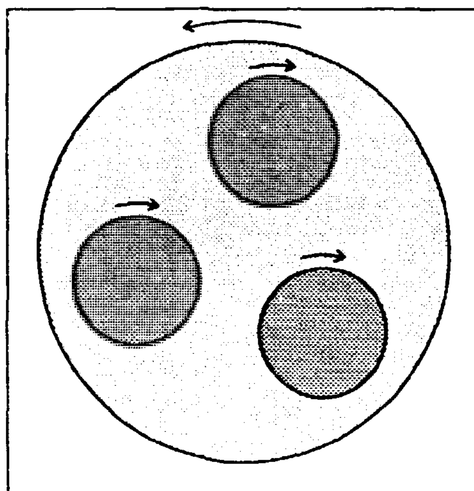

Figure 1.5 Top view of the rotating substrate table. In this case the first stage is rotating counter-clockwise.

After deposition the films were removed from the deposition chamber and transferred to a scanning electron microscope (SEM) at the Materials Department. This microscope is equipped with a stage for energy dispersive X-ray analysis (EDX). The chemical composition of the films was analyzed using this stage. The principle behind this type of measurement is that the incoming electron beam will have sufficient energy to knock out electrons from the atoms in the sample with the emission of characteristic X-ray lines as a consequence. We have used a SEM from JEOL (model JSM-840) operated at 20 kV with an EDX stage from EDAX (model 9100).
After the EDX analysis the samples were transferred to an X-ray powder spectrometer (Phillips model PW 1130/90) for determination of the crystal structure. This machine is also situated at the Materials Department. It is interfaced to a Hewlett-Packard HP-85 microcomputer, which is also used to store the data.
Finally, the films were characterized by a resistance versus temperature measurement. This last step was carried out at the Physics Department. The resistance was measured by the four point technique by attaching four wires

to the sample with silver paint. The sample was then mounted in a cryostat cooled by a closed cycle refrigerator (Displex). A measurement current of 1 mA was typically used. The voltage across the sample was measured with a digital voltmeter and the resistance was calculated. This was all done under computer control.
Some of the films were deposited at room temperature on MgO and YSZ substrates. In these cases the films were post-annealed in an oxygen atmosphere using a programmable oven, which allows specification of a certain temperature profile for the annealing procedure. This annealing step was done between the EDX and X-ray analyses.

1.1.4 Results of sputtering at Risø

As already indicated in the last section, we have used two different configurations of the sputter system in our experiments. We will first describe the least successful of these, which is the planar magnetron gun in combination with the rotating, unheated substrate table.
As mentioned in section 1.1.1, the use of a magnetron together with a multi-component target leads to variations in the chemical composition of the films across the substrate. This problem can be solved by using a rotating substrate table, which will even out the spatial variations. However, the problem of resputtering due to negative oxygen ions still remains. Consequently, the composition of the films will be different from that of the target.
The obvious solution to this problem is to change the composition of the target such that the composition of the film will be correct under the influence of the resputtering. We have used this approach (starting with a stoichiometrically correct target) rather than using a high sputter gas pressure to eliminate the resputtering. Note that when the films are deposited at room temperature there is no required minimum oxygen partial pressure, since the film grows in an amorphous layer. An elevated sputter gas pressure is therefore not mandatory. It turns out that this approach leads to an iterative process, i.e. it is necessary to make several targets with their chemical composition adjusted based on the EDX analysis of the films deposited from the previous target.
All the planar targets were used with a pure argon sputter gas at a pressure of 10^{-2} mbar. The RF power was kept at 300 W and the target to substrate distance was 43 mm in all cases. Glass slides, MgO and YSZ were used as substrates. The films deposited on glass slides were only used to measure the composition of the deposit; no attempt was made to make them superconducting by post-annealing.
In Table 1.1 we show how the composition of the compensated targets change from one generation to the next. The first two columns show the Ba and Cu content in the target. The next two columns show the Ba and Cu content in the resulting films, while the last two columns show the calculated composition of the new compensated target based on the composition of the films. In all three cases the Y content is normalized to 1 and therefore not shown. For each target a series of films were made (often more than one film per deposition) and the composition was determined. After a few runs (typically 4-5) of 12-14 hours

duration the target surface reached a steady state, and at this point the composition of the films became reasonable constant from run to run. The average composition of the last couple of depositions was then used to calculate the composition of the next target generation based on the relations $Ba_{NEW} = 2 (Ba_{OLD} / Ba_{FILM})$ and $Cu_{NEW} = 3 (Cu_{OLD} / Cu_{FILM})$.

Target		Film		New target	
Ba_{OLD}	Cu_{OLD}	Ba_{FILM}	Cu_{FILM}	Ba_{NEW}	Cu_{NEW}
2.00	3.00	0.94	2.61	4.27	3.45
4.27	3.45	3.46	3.20	2.47	3.23
2.47	3.23	1.93	2.69	---	---

Table 1.1 The composition of target, films and compensated targets in three iterations.

None of the films deposited onto MgO and YSZ from the first two targets became superconducting after annealing. The third target resulted in three films which showed a semiconducting behavior from room temperature down to 90 K. At this temperature the resistance started to drop and the films became fully superconducting around 30 K. The temperature profile for the annealing step was as follows: Heat at 200 °C/h to T=880 °C, keep T=880 °C for 30 min, cool at 200 °C/h to 550 °C, keep T=550 °C for 2 hours (oxygen up-take), then cool at 200 °C/h to room temperature. A characteristic R versus T curve is shown in Figure 1.6. The composition of this film is 1:1.96:2.75 as determined by EDX.

The X-ray spectrum for this particular sample shows that the strongest reflection is the (103), indicating that most of the film is randomly oriented with respect to the substrate. Also, there are several peaks that can not be identified as belonging to the 1:2:3 phase of YBCO. We can thus conclude that the film consists of several phases and that even the 1:2:3 part of the film is of poor crystallographic quality. As can be seen from Table 1.1, the films from this target generation are slightly Cu deficient, and it is possible that we could get better results by continuing the iterative process. However, at this point it became clear from literature studies that even if we were able to deposit films with 1:2:3 composition and a T_c close to 90 K, they would still be of poor crystallographic quality due to the post-annealing. It was therefore decided to abandon this approach at this point.

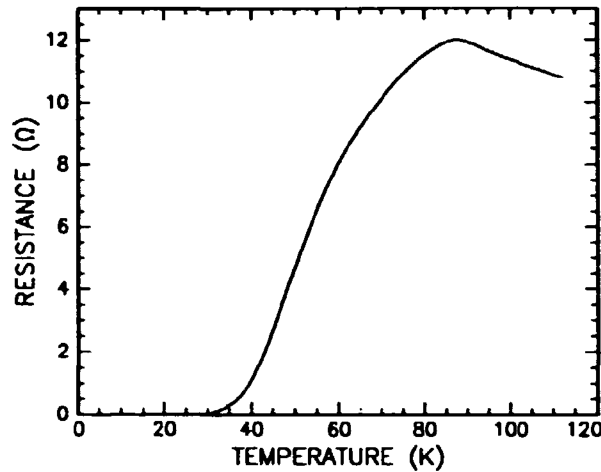

Figure 1.6 Resistance versus temperature for a film deposited from the third generation of compensated targets.

Next we discuss the results from the second sputter system configuration that we have employed. This configuration consisted of a cylindrical target with an inner diameter of 70 mm and a length of 25 mm. It was mounted at one of the water cooled sputter guns instead of a planar target. A ring magnet was placed on the outside of the target to achieve the magnetron effect. The rotating substrate table was replaced by a non-rotating, heated substrate table, which allowed us to keep the substrate at temperatures up to 800 °C during deposition. Note that when a cylindrical target is used, the substrates are not directly facing the target. The mechanism whereby the material is transferred from the target to the substrate thus becomes more of a diffusion rather than a direct ejection from the target onto the substrate and consequently, we expect the spatial variations caused by the magnetron to be much smaller. This is the justification for not using a rotating substrate even though we do use a magnetron.

Initially, we chose to operate the sputter system under conditions similar to those reported by the Karlsruhe group (Ref. 18), i.e. we used a sputter gas with a total pressure of 0.5 mbar and consisting of equal amounts of argon and oxygen. We used a target to substrate distance of 20 mm (measured from the bottom end of the cylinder to the substrate) and we applied 300 W RF power to the sputter gun. The substrates were placed on the axis of the cylindrical target.

In order to obtain superconducting films it is necessary to do a systematic study of the influence of the various sputter process parameters on the film quality. The most important parameters are the substrate temperature, the gas pressure and composition, and the position of the substrate relative to the target. We started by examining the influence of the substrate temperature. MgO substrates were used in all depositions at elevated substrate temperatures. In Table 1.2 we show the results from five films deposited at five different temperatures. The first column indicates the substrate temperature during

deposition, the second and third columns give the Ba and Cu content (with Y normalized to 1) and the last column indicates the transition temperature.

T_s (°C)	Ba	Cu	T_c (K)
525	2.93	3.02	---
600	2.81	2.71	---
700	2.73	3.00	30
750	2.79	2.74	67
800	3.05	2.67	---

Table 1.2 Deposition temperature T_s, Ba and Cu content, and T_c for five films deposited on MgO substrates in a 50/50 argon/oxygen atmosphere with a total pressure of 0.5 mbar. The two first and the last film were not superconducting at any temperature.

From Table 1.2 we can see that a substrate temperature around 750 °C during deposition gives the best result. The Cu content in the films fluctuates around the correct value, but the Ba content is clearly too high; in some cases there is more Ba than Cu in the films. In Figure 1.7 we show the R versus T curve for the film deposited at 750 °C and in Figure 1.8 we show the X-ray spectrum for the same sample. The spectrum consists of 7 (00*l*) reflections from YBCO (marked by +) and three reflections that do not belong to the 1:2:3 phase of YBCO (marked by -). We conclude that the excess Ba content leads to the formation of one or more foreign phases in the film.

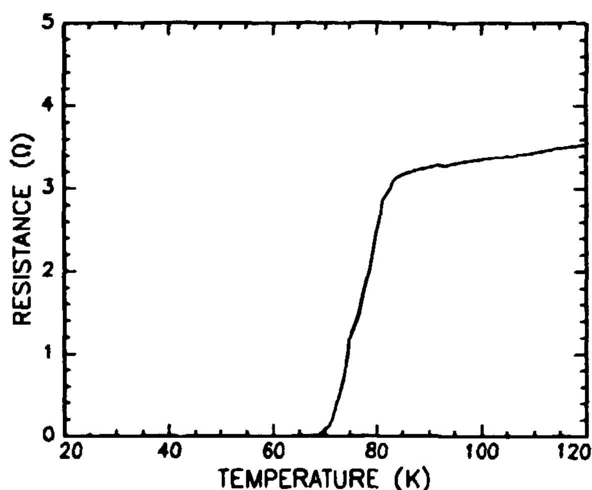

Figure 1.7 Resistance versus temperature for a film deposited at T_s = 750 °C in 0.5 mbar total pressure and 50 % oxygen content in the sputter gas.

In the next series of depositions we tried to eliminate the excess Ba by varying the oxygen content in the gas while keeping the total pressure constant. Alternatively, we could have tried to change the total pressure while keeping the composition constant. Unfortunately, we did not have much room to vary the total pressure. The deposition rate was very low already with a total pressure of 0.5 mbar (it was necessary to deposit overnight to get a film thick enough not to be transparent) and an increased pressure would presumably only make things worse. On the other hand, by lowering the total pressure the oxygen would constitute the majority of the sputter gas, considering that we want to keep a minimum partial pressure of about 0.2 mbar, i.e. the abundance of argon atoms would become relatively small and this would presumably also reduce the deposition rate.

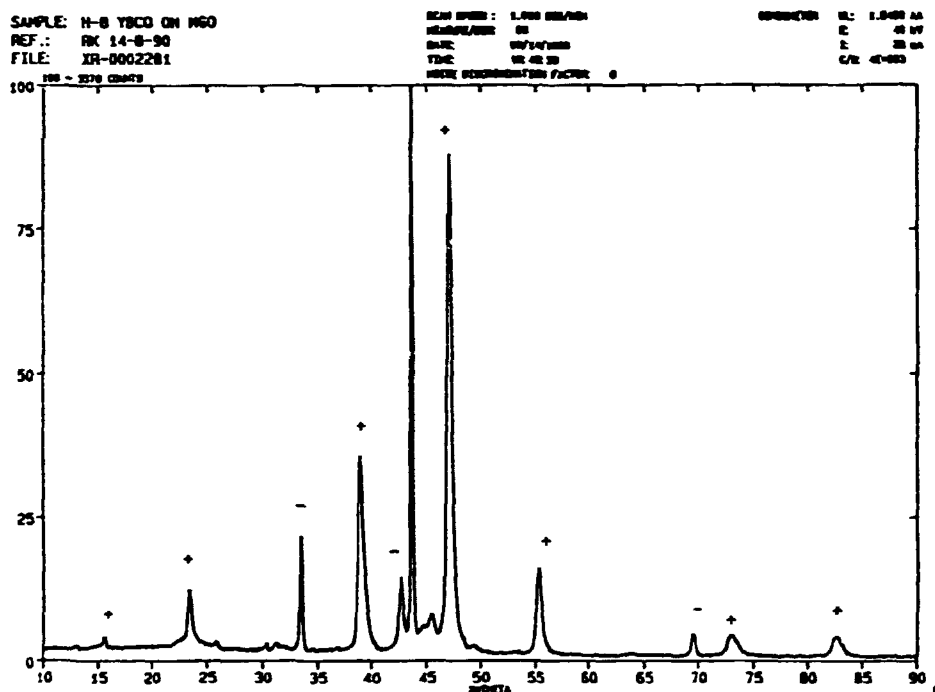

Figure 1.8 X-ray spectrum for the same film as in Figure 1.7. The three peaks marked by - do not originate from the YBCO 1:2:3 phase.

In Table 1.3 we show the results from four films deposited at 750 °C in 0.5 mbar total pressure and with 300 W RF power. The target to substrate distance was 20 mm as before and the samples were placed on the axis of the cylindrical target.

We see that the film deposited in pure argon is very far off the correct composition. On the other hand, this film is not really interesting, since we would not be able to grow the 1:2:3 phase under these conditions anyway. Both the Ba and the Cu content decreases with increasing oxygen content, and in the case where 90 % of the gas is oxygen, the Ba content is almost reduced to the correct value. Unfortunately, the Cu content is also decreased far below its correct value at this oxygen content, and the film does not become

superconducting. The best result in terms of T_c is obtained for the film deposited with 25 % oxygen in the gas. In Figure 1.9 we show the R versus T curve for this sample. The film becomes fully superconducting at 77 K with a transition width of about 8 K. Much more interesting is the X-ray spectrum for this sample, which is shown in Figure 1.10. Comparing to the spectrum in Figure 1.8 we see that the 7 (00*l*) reflections from the YBCO 1:2:3 phase are still present, while the three peaks belonging to a foreign phase have disappeared. Instead, three small peaks have appeared between 30° and 35 °, one of them is the YBCO (103) at 2θ = 32.85 °. Also, when the absolute intensities are compared, we see that the peaks are about 100 times stronger in Figure 1.10 than in Figure 1.8 (about 2.5 × 10^5 cts/sec compared to 2500 cts/sec). We can thus conclude that the quality of the part of the film that grows in the 1:2:3 phase is strongly improved by reducing the oxygen content from 50 % to 25 % during deposition. However, the problem of the excess Ba still remains.

Ar/O_2	Ba	Cu	T_c (K)
100/0	4.08	6.97	---
75/25	3.32	3.36	77
50/50	2.79	2.74	67
10/90	2.33	2.36	---

Table 1.3 Gas composition, Ba and Cu content and T_c for four films deposited on MgO substrates at 750 °C and with a total pressure of 0.5 mbar.

The next attempt to eliminate the excess Ba involved an investigation of how the composition of the films depends on the position of the substrate relative to the target. To this end we made two depositions on glass slides without heating them. The glass slides were long enough that the composition could be measured at various points along a profile from the center to the edge of the target using only one sample (in contrast to the MgO substrates which were only 10 × 10 mm). In the first deposition the slide was oriented horizontally (corresponding to the usual orientation) and placed 20 mm below the target. In the second deposition the slide was oriented vertically along the edge of the target (as an extension of it). Both depositions were carried out in 0.5 mbar total pressure with 25 % oxygen content. After the depositions the glass slides were transferred to the SEM and the composition of the deposit was determined in a number of points along the profile. This experiment should tell us the best substrate position in both the horizontal and vertical direction.

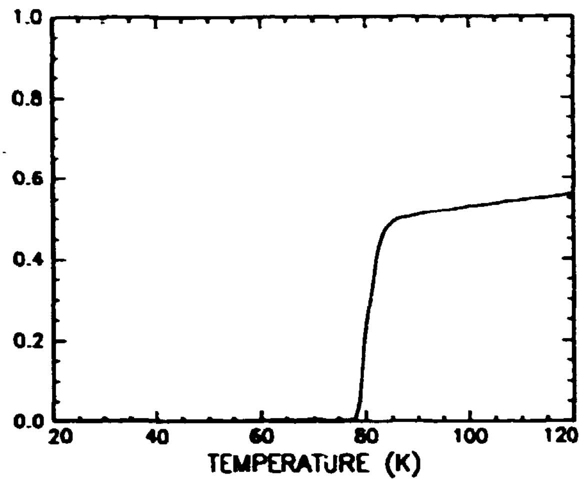

Figure 1.9 Resistance versus temperature for a film deposited at T_s = 750 °C in 0.5 mbar total pressure and 25 % oxygen content in the sputter gas.

The result is shown in Figure 1.11. On the left and right is shown the composition versus horizontal and vertical position, respectively. We see that at about 25 mm from the center (10 mm from the edge of the target) the Ba content is correct, while the Cu content is a bit too small. Likewise, we see that the Ba content is correct in the range 20-25 mm below the target, while the Cu content is optimum a little further away at about 27 mm from the target.

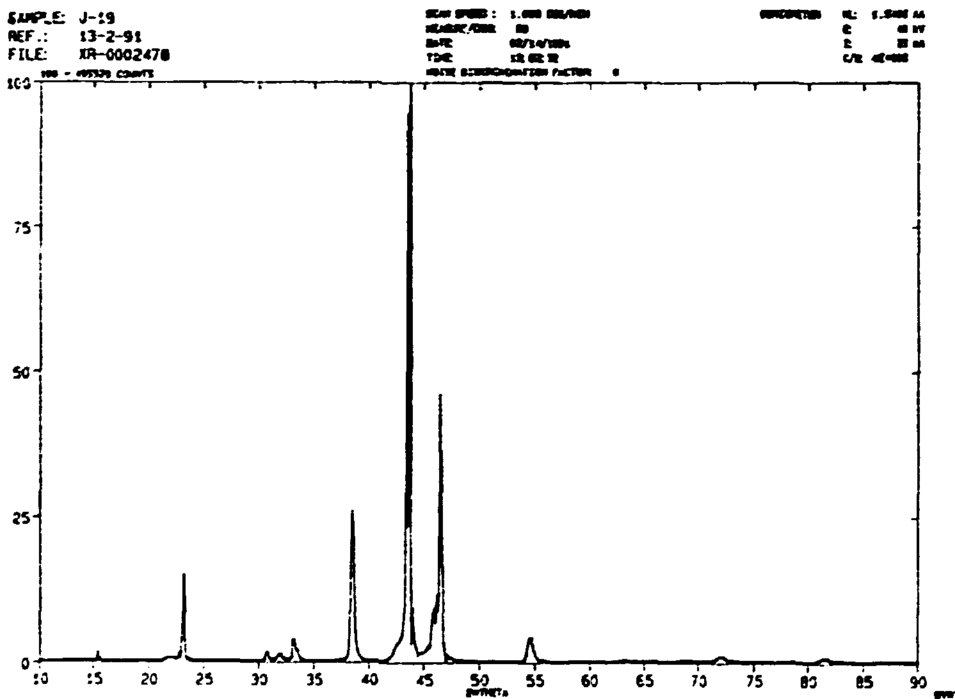

Figure 1.10 X-ray spectrum for the same film as in Figure 1.9. Apart from the three peaks between 30° and 35°, only (00l) reflection from the YBCO 1:2:3 phase appear.

At a pressure of 0.5 mbar the mean free path in the sputter gas is less than 1 mm. Thus, since the target to substrate distance is several cm, the transport process of the sputtered particles from the target to the substrate is diffusive in nature (rather than ballistic). If we assume that the three cations Y, Ba and Cu are ejected with the same energy from the target then Ba, by virtue of its larger mass, will have the smallest velocity and consequently the lowest diffusion constant. However, it is not clear how this fact can explain the above results. Other phenomena may also play a role. For instance, the three cations will probably oxidize at different rates. This will change the energy of the sputtered particles in a differential way and consequently also their velocity and diffusion constant. However, we have no experimental evidence to support these speculations.

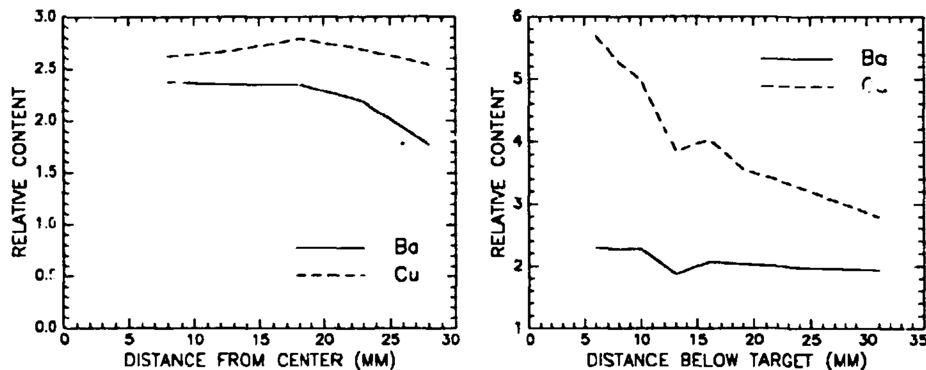

Figure 1.11 The Ba and Cu content versus horizontal and vertical position of the substrate relative to the target (left and right, respectively). In both cases the Y content was normalized to 1.

Armed with the new information about the substrate position dependence of the film composition, we immediately deposited a film at a position about 25 mm below the target and close to the edge, since this should give a chemical composition as close to 1:2:3 as possible. The film was deposited at 750 °C in 0.5 mbar total pressure with 25 % oxygen. Much to our disappointment, we found only a slight improvement in the Ba content; the film had a composition of 1:2.53:3.36. Based on the experiment with film composition versus substrate position we would have expected the Ba content to be less than 2 rather than above 2 at this substrate position. The reason for this discrepancy is most likely that the sticking coefficients of the sputtered atoms are temperature dependent such that experiments at room temperature can not be compared with experiments at 750 °C. The R versus T curve for the film is essentially identical to the one shown in Figure 1.9. The film becomes fully superconducting at 75.5 K with a transition width of about 7 K. The X-ray spectrum is shown in Figure 1.12. It consists only of YBCO (00l) peaks except for a very small (103) peak. The diffracted intensity is comparable to the spectrum in Figure 1.10 and we conclude that the 1:2:3 part of the film is of good quality. At this point it was necessary to stop the experiments with sputtering due to time constraints. Based on the measurements of film composition versus

substrate position the next logical step would have been to use a target with a smaller inner diameter (about 25-30 mm instead of 70 mm), since this will bring the substrates closer to the edge of the target. It will also enhance the off-axis nature of the sputter gun, i.e. it will place the substrates further away from the plasma region of the sputter gas. Also, it would be instructive to repeat the experiment with film composition versus substrate position, this time using heated substrates to see if the temperature plays a role, as we expect it to.

We conclude the discussion of thin film fabrication by rf sputtering by showing (in Figure 1.13) a pole figure for a sample deposited under conditions similar to the sample shown in Figures 1.7 and 1.8. The experimental details and the interpretation of pole figures is discussed in Chapter 2. By comparing to the pole figures shown in Chapter 2 for laser ablated films (Figures 2.9 and 2.10) we note that the sputtered film appears to be free of 45° misorientations in the a-b plane. However, the mosaic spread appears to be significantly larger both in χ and φ. The relatively wide angular distribution of the a-b axes coupled with the fact that the film contains foreign phases suggest that the critical current density is rather modest for this film.

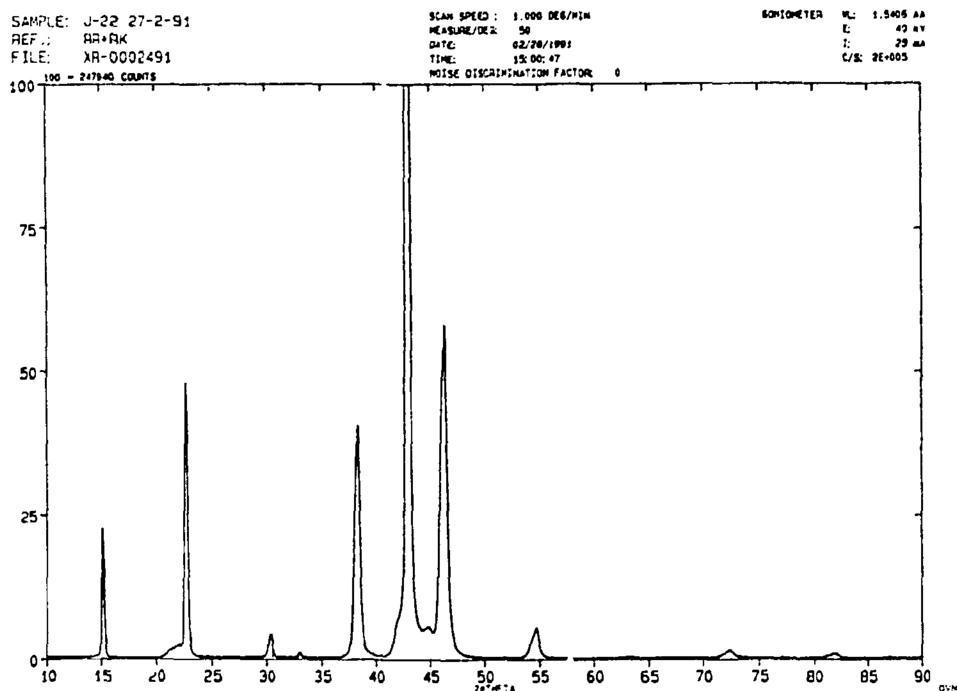

Figure 1.12 X-ray spectrum for the film deposited close to the edge of the target. Besides the small (103) peak the spectrum consists only of (00l) reflections from YBCO.

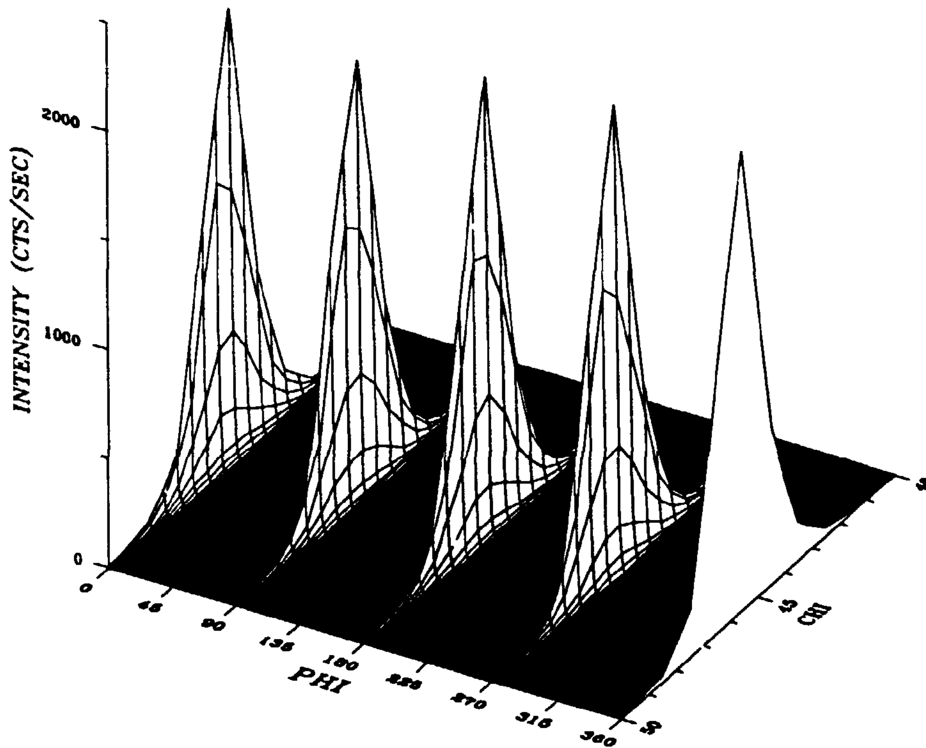

Figure 1.13 Pole figure for the YBCO (103) reflection measured on a sample deposited at 750°C in 0.5 mbar total pressure with 50 % oxygen.

1.2 Laser ablation

Thin film deposition by the laser ablation technique has found widespread application in the context of high T_c superconductors, because it virtually eliminates the very annoying problem of resputtering which is so characteristic of sputtering. The technique is almost as old as the laser itself (the earliest reports[20] of thin film deposition go back to the mid-60s), although in those days the preferential sputtering from multi-component targets was a problem for this technique also. The breakthrough came in the early 80s, when the deposition of stoichiometric semiconductor films was first demonstrated. For instance, Cheung et al[21] deposited $Hg_{1-x}Cd_xTe$ films and found that the composition of the film could be adjusted to match the target composition by applying a certain background pressure of Hg. The first successful demonstration of laser ablated YBCO thin films is due to Dijkkamp et al[22]. In the next section we will discuss the mechanisms involved in laser ablation and we will subsequently describe the deposition system at UC Berkeley. The results we have obtained with this deposition system are described in Chapter 3.

1.2.1 Theory of laser ablation

The title of this section is a bit pretentious, since there is no well established theory of laser ablation at present. However, several spectroscopic techniques

have been applied to the process and some suggestions about the mechanism responsible for the ablation have been put forward.

In practice the output from a pulsed laser (solid state or excimer) is focussed onto a target. Typical numbers for the laser power and pulse length are 10^7 W and a few tens of nanoseconds, resulting in an energy per pulse in the range 0.1 J to 1 J. This energy is focussed onto a spot with a diameter of a few mm, giving an energy density of typically 1-5 J/cm^2. This quantity (the energy density) is termed the laser fluence. Besides the fluence, the wavelength of the laser light is also found to have a significant effect on the ablation process. Typical wave lengths are in the 250-350 nm range. Each laser pulse gives rise to a plume. This term refers to the light emitting collection of species released from the target by the laser pulse.

The simplest scenario one can think of is that the target material simply evaporates and is transferred to the substrate in clusters of correct stoichiometry. However, several studies suggest that this is not the case. Venkatesan et al[23] have used laser ionization mass spectroscopy to identify the ionic species emitted from the target. They find signatures from Y, Ba, Cu and their oxides and also from more complex oxides such as BaCuO and YBa_2O_3, but they see no sign of $YBa_2Cu_3O_7$. Similar results are obtained by Dyer et al[24] by studying the emission from the plume. In addition to the species found by Venkatesan et al they also find singly ionized Y, Ba, Cu and O_2. By measuring the charge of the species emitted in each pulse and comparing with the mass removed from the target per pulse they find that between 1.4 % and 4 % of the species in the plume are ionized, i.e. by far the most material is transferred as neutrals. The experimental setup in this study allowed a determination of the expansion velocity of the plume. At a fluence of 1 J/cm^2 they find velocities around 10^4 m/s for Y, Y^+, Cu and Ba^+. In the case of copper this speed corresponds to a temperature around 4000 K. In Ref. 23 the authors estimate a temperature of 15000 K for the emitted species. These numbers suggest that something more powerful than a simple evaporation is at play.

Theoretical calculations based on a one-dimensional heat flow equation indicate that temperatures far higher than the melting point of YBCO (about 1100°C) can indeed be reached inside the target. Singh et al[25] find that the temperature difference between the hottest point in the target and its surface can be as high as 2000°C depending on the absorption coefficient α. The subsurface heating is most pronounced at small values of α. Also, the laser beam will penetrate further into the target for small values of α and the distance between surface and the hottest point in the target will thus increase with decreasing α. Similar results are found by Otsubo et al[26], although they find a maximum temperature differential of only 1000°C. In both studies it is argued that evaporation from the surface of the target plays a key role in keeping the surface at a lower temperature than the interior of the target.

In another study by Venkatesan et al[27] the angular distribution of the thickness and composition of the laser ablated material was investigated by Rutherford backscattering. They find that two distinct components can be identified. The first is a non-stoichiometric part varying as $\cos(\theta)$, where θ is the angle that the emitted particles make with the normal to the target. The second compo-

nent is a highly forward directed component with an angular dependence sharper than $\cos^{11}(\theta)$. They find that the fluence threshold for the latter component is about 0.4 J/cm^2. The amount of material following this angular distribution increases with increasing fluence, whereas the $\cos(\theta)$ component is essentially independent of fluence. The authors speculate that the $\cos(\theta)$ component is due to evaporation from the surface, while the forward directed component is due to a secondary process, possibly induced by the evaporation of the surface material. One can imagine that if the target surface recedes fast enough, a shock wave could be formed which would lead to explosive removal of the subsurface material. The problem with this explanation is that the required power density for the formation of a shock wave is a couple of orders of magnitude higher than the typical values used in deposition experiments.
Other mechanisms have been proposed to explain the high temperatures of the laser ablated material. For instance, Ready[28] has proposed a scenario whereby the recoil pressure of the evaporated material is sufficient to raise the boiling point of the target material to the critical point. At this point there is no longer any distinction between a superheated solid and a highly condensed gas, and the target material is free to expand without any latent heat of vaporization. This explanation appears to be highly speculative, since the author extrapolates low-temperature vapor-pressure data to temperatures of several thousand degrees in order to estimate whether the recoil pressure can keep the material in its solid state up to the critical point.
A couple of other mechanisms are mentioned in Ref. 26 and 27 together with suggestions as to why they are probably not the correct ones. We conclude this section by noting that whatever the exact mechanism of laser ablation is, the technique has proved to be very fast and reliable compared to sputtering and consequently, it has emerged as the deposition method of choice for device work where throughput is important. The only drawback of laser ablation is that relative large particles (on the order of 1 μm in diameter) are sometimes found on the surface of the deposited films. These particles are referred to as boulders and can result in shorts between two superconducting layers separated by an insulator. The density of the boulders seems to correlate with the wave length of the laser light[29], with short wave lengths (248 nm or below) resulting in the lowest density. The number of boulders can be reduced by rotating the target during deposition such that it is hit only once in each spot. Each time the target is hit, a small crater is formed on the surface and a subsequent pulse in the same spot would lead to ejection of material from the rim of the crater with the creation of boulders as a consequence. Furthermore, we have found that by polishing the YBCO target with emery paper before deposition of the first layer in a multi-layer sample, the density of the boulders can be reduced to a point where they no longer present a problem.

1.2.2 Description of the deposition system at UC Berkeley

For the experiments at UC Berkeley we have used a deposition system[30] built around an excimer laser from Questek (model 2820). When this laser is operated with a KrF gas fill it is capable of emitting up to 850 mJ per pulse

at a wave length of 248 nm and with a pulse length of 18 ns. The laser beam is focussed onto the target by a lens which can be moved back and forth such that the spot size can be varied. In this way the fluence can be changed. We have used a fluence of 2.5 J/cm^2 for most of the depositions; only during MgO depositions did we increase the fluence to about 4 J/cm^2 because of the low deposition rate.

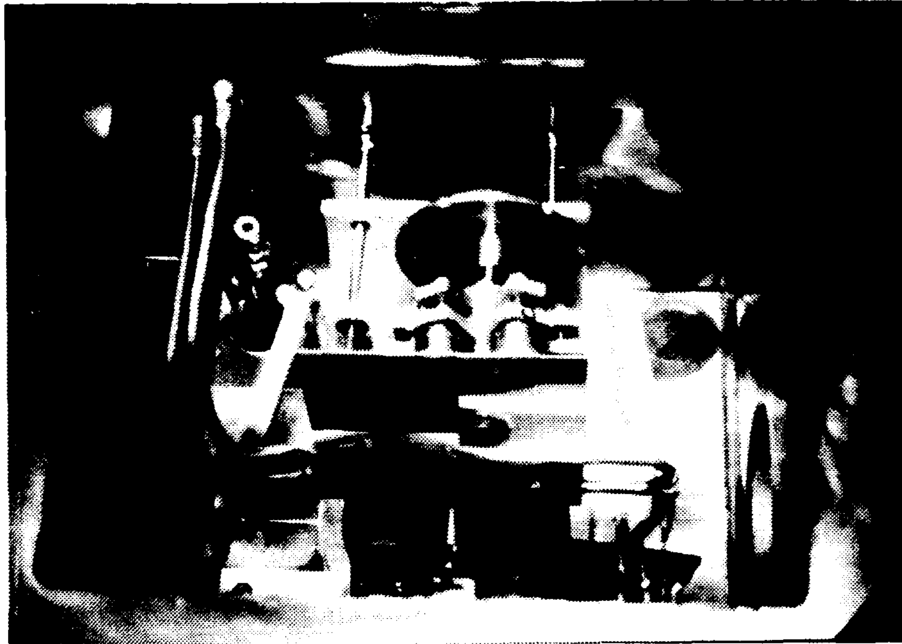

Figure 1.14 Photograph of the interior of the vacuum chamber.

The target holder is mounted in a vacuum chamber equipped with a Varian 6" diffusion pump backed by a Varian mechanical pump. The base pressure of the chamber is about 8×10^{-7} Torr ($\approx 10^{-6}$ mbar). The interior of the vacuum chamber is shown in Figure 1.14. Up to six targets can be mounted in the target holder simultaneously, and it is possible to change from one target to another without breaking the vacuum. The laser beam hits the target approximately halfway between the center and the edge, and the target in use in rotated around an axis going through its center to ensure that it is sputtered as evenly as possible. The sample holder is placed at a distance of 6 cm from the target. The temperature of the heater block is measured by a thermocouple mounted directly beneath the substrate. In addition to the thermocouple, the temperature can also be measured by a pyrometer looking through a window in the vacuum chamber. When everything is in proper condition, the thermocouple and the pyrometer agree to within 5°C.
The results we have obtained with this deposition system are described in a separate chapter (Chapter 3), since the emphasis in this part of the work was the fabrication of devices based on YBCO thin films rather than the deposition of the films themselves.

1.3 Conclusions

In this chapter we have described the two different deposition methods used and the results of our experiments with thin film deposition by rf sputtering. We have used two different configurations of the sputter system in these experiments. The first of these was a parallel plate configuration with magnetron and a rotating substrate table. The idea in these experiments was to use a series of targets with off-stoichiometric composition to compensate for the resputtering effect. After three iterations we obtained superconducting films, but with a very low T_c ($\approx$ 30 K). Even though it might have been possible to raise the T_c by continuing the iterative process, we decided to abandon this approach because it was impossible to combine it with a heated substrate table and consequently, we could not fabricate films in-situ.
The second configuration of the sputter system consisted of an inverted cylindrical magnetron sputter gun in combination with a heated substrate table. Initially, we made a series of depositions to determine the best substrate temperature and we found that 750°C gave the highest T_c. Next, we varied the oxygen content in the gas and found that 25 % oxygen gave a higher T_c and a significant increase in the diffracted X-ray intensity. Under these conditions (T_s=750°C, P_{O2}=25 %) we obtained films with a T_c of 77 K and with an X-ray spectrum consisting essentially of only (00*l*) reflections from the YBCO 1:2:3 phase. However, the films contained too much Ba, leading to the formation of foreign phases in the film and this is most likely the cause of the reduced T_c. We have made a series of experiments to find out if the Ba content can be reduced by changing the position of the substrate relative to the target. We find that if the substrate is placed close to the edge of the cylindrical target and about 25 mm below it, the composition of the film is very close to 1:2:3. However, this experiment was carried out at room temperature and we find that as soon as the temperature is raised to 750°C, the composition changes, even though the substrate is kept at the same orientation relative to the target. The films still contain too much Ba and no improvement in T_c is obtained. The fact that the composition changes with temperature is probably a consequence of the sticking coefficients being temperature dependent. We speculate that the fact that the best film composition is obtained close to the edge of the target is related to the diffusive nature of the transport process of the sputtered material, although it is not possible to determine the exact cause based on the experiments carried out so far.
In future work a target with a smaller diameter should be used, since this will increase the off-axis nature of the sputter gun. The experiment where the film composition is measured as a function of substrate position should then be repeated with heated substrates, and hopefully the composition will then be closer to 1:2:3 and more independent of substrate position.
In the last part of this chapter we have discussed the principles of laser ablation and we have described the deposition system at UC Berkeley. However, the results of this work is deferred to Chapter 3, since it is primarily related to the fabrication of devices rather than deposition of the thin films themselves.

References

[1] J.G. Bednorz and K.A. Müller. Z. Phys. B, **64** (1986), 189.

[2] M.K. Wu, J.R. Ashburn, C.J. Torng, P.H. Hor, R.L. Meng, L. Gao, Z.J. Huang, Y.Q. Wang and C.W. Chu. Phys. Rev. Lett., **58** (1987), 908.

[3] P.H. Hor, L. Gao, R.L. Meng, Z.J. Huang, Y.Q. Wang, K. Forster, J. Vassilious, C.W. Chu, M.K. Wu, J.R. Ashburn and C.J. Torng. Phys. Rev. Lett., **58** (1987), 911.

[4] B. Chapman: "Glow discharge processes", (Wiley, New York, 1980).

[5] H. Adachi, K. Setsune, T. Mitsuyu, K. Hirochi, Y. Ichikawa, T. Kamada and K. Wasa. Jap. J. Appl. Phys., **26** (1987), L709.

[6] S.I. Shah. Appl. Phys. Lett., **53** (1988), 612.

[7] C.T. Cheung and E. Ruckenstein. Mat. Lett., **7** (1988), 172.

[8] H. Koinuma, K. Fukuda, T. Hashimoto and K. Fueki. Jap. J. Appl. Phys., **27** (1988), L1216.

[9] R. Bormann and J. Nölting. Appl. Phys. Lett., **54** (1989), 2148.

[10] H.C. Li, G. Linker, F. Ratzel, R. Smithey and J. Geerk. Appl. Phys Lett., **52** (1988), 1098.

[11] M. Guilloux-Viry, M.G. Karkut, A. Perrin, O. Peña, J. Padiou and M. Sargent. Physica C, **166** (1990), 105.

[12] C.B. Eom, J.Z. Sun, K. Yamamoto, A.F. Marshall, K.E. Luther, T.H. Geballe and S.S. Laderman. Appl. Phys. Lett., **55** (1989), 595.

[13] R.L. Sandstrom, W.J. Gallagher, T.R. Dinger, R.H. Koch, R.B. Laibowitz, A.W. Kleinsasser, R.J. Gambino, B. Bumble and M.F. Chisholm. Appl. Phys Lett., **53** (1988), 444.

[14] J. Gao, B. Haüser and H. Rogalla. J. Appl. Phys., **67** (1990), 2512.

[15] H. Koinuma, M. Kawasaki, M. Funbashi, T. Hasegawa, K. Kishio, K. Kitazawa, K. Fueki and S. Nagata. J. Appl. Phys., **62** (1987), 1524.

[16] M. Kawasaki, S. Nagata, Y. Sato, M. Funbashi, T. Hasegawa, K. Kishio, K. Kitazawa, K. Fueki and H. Koinuma. Jap. J. Appl. Phys., **26** (1987), L738.

[17] H. Koinuma, M. Kawasaki, S. Nagata, K. Takeuchi and K Fueki. Jap. J. Appl. Phys., **27** (1988), L376.

[18] X.X. Xi, G. Linker, O. Meyer, E. Nold, B. Obst, F. Ratzel, R. Smithey, B. Strehlau, F. Weschenfelder and J. Geerk. Z. Phys. B., **74** (1989), 13.

[19] R. Pinto, L.C. Gupta, R. Vijayaraghavan, A.G. Chourey and V.S. Shirodkar. Physica C, **171** (1990), 131.

[20] H.M. Smith and A.F. Turner. Appl. Opt., **4** (1965), 147.

[21] J.T. Cheung and D.T. Cheung. J. Vac. Sci. Technol., **21** (1982), 182.

[22] D. Dijkkamp, T. Venkatesan, X.D. Wu, S.A. Shaheen, N. Jisrawi, Y.H. Min-Lee, W.L. McLean and M. Croft. Appl. Phys. Lett., **51** (1987), 619.

[23] T. Venkatesan, X.D. Wu, A. Inam, Y. Jeon, M. Croft, E.W. Chase, C.C. Chang, J.B. Wachtman, R.W. Odom, F. Radicati di Brozolo and C.A. Magee. Appl. Phys. Lett., **53** (1988), 1431.

[24] P.E. Dyer, R.D. Greenough, A. Issa and P.H. Key. Appl. Phys. Lett., **53** (1988), 534.

[25] R.K. Singh, D. Bhattacharya and J. Narayan. Appl. Phys. Lett., **57** (1990), 2022.

[26] S. Otsubo, T. Minamikawa, Y. Yonezawa, A. Morimoto and T. Shimizu. Jap. J. Appl. Phys., **29** (1990), L73.

[27] T. Venkatesan, X.D. Wu, A. Inam and J.B. Wachtman. Appl. Phys. Lett., **52** (1988), 1193.

[28] J.F. Ready. J. Appl. Phys., **36** (1965), 462.

[29] G. Koren, A. Gupta, R.J. Baseman, M.I. Lutwyche and R.B. Laibowitz. Appl. Phys. Lett., **55** (1989), 2450.

[30] J.J. Kingston, F.C. Wellstood, P. Lerch, A.H. Miklich and J. Clarke. Appl. Phys. Lett., **56** (1990), 189.

2 Structural characterization

The structural properties of YBCO has been studied extensively throughout the time span from its discovery until the present time both in bulk samples and in thin films. The neutron diffraction studies on bulk samples have provided valuable information about the correlation between the superconducting and the structural properties of this material, which may eventually lead to the formulation of a theory for the mechanism responsible for high temperature superconductivity. Structural characterization by X-ray diffraction has been applied to thin films of YBCO deposited by a variety of techniques on a number of single crystal substrates. These studies have revealed that, because of the anisotropy of YBCO, only certain orientations of the thin film with respect to the substrate result in films of high quality in terms of their superconducting properties. In this chapter we will describe our work on the structural characterization by X-ray diffraction of laser ablated films on $SrTiO_3$ and MgO substrates. However, before we proceed with this, we will briefly describe the theory of diffraction of X-rays by crystalline solids.

2.1 Fundamentals of X-ray diffraction

The crystal structure of solids is described in terms of Bravais lattices. A Bravais lattice is an infinite array of discrete points with an arrangement and orientation that appears exactly the same from whichever of the points the array is viewed. The lattice is described in terms of three lattice vectors $\mathbf{a}$, $\mathbf{b}$ and $\mathbf{c}$. Any vector $\mathbf{R}$ of the Bravais lattice can thus be expressed as a linear combination of $\mathbf{a}$, $\mathbf{b}$ and $\mathbf{c}$ with integer coefficients.
The diffraction of X-rays by a crystal is caused by the interaction between the electrons in the crystal and the electric field associated with the X-ray beam. As the beam passes by the electron, the electric field will cause it to oscillate back and forth about its equilibrium position with the same frequency as the X-ray beam. This will result in the emission of a spherical electromagnetic wave from the electron. There are several electrons per atom but as a first approach we will consider the solid as a Bravais lattice of single electrons. The diffracted beam results from the superposition of the scattered waves from all the electrons in the crystal. As we shall see, X-ray radiation is useful for structural characterization because it has a wave length which is comparable to the interatomic spacings in solids.
Consider first a one dimensional chain of atoms with spacing a as shown in Figure 2.1. We will now find the condition under which a beam incident at an angle α with the linear chain is diffracted into a beam making an angle β with the chain. The two dotted lines in the figure denote the wave front of the incident and the diffracted beam, respectively, and it is easy to see that the spherical waves emitted by neighboring atoms will interfere constructively if the difference in the length of the path traveled by them differ by an integral number of wave lengths. We have thus AC-BD=$n\lambda$, where λ is the wavelength of the X-rays. By simple geometry this condition can be related to the interatomic spacing a, giving:

$$a\,(\cos(\beta) - \cos(\alpha)) = n\lambda$$

We see that for each incident angle α we get a number of diffracted beams for n=1,2..., subject to the constraint $\cos(\beta) = \cos(\alpha) + n\lambda/a < 1$. The number n is referred to as the order of the diffraction.

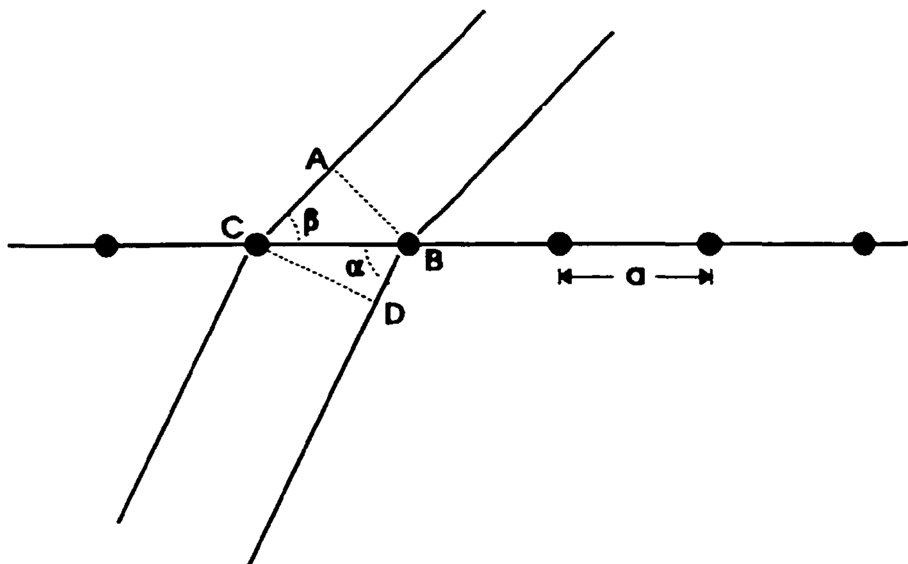

Figure 2.1 An X-ray beam incident under an angle α is diffracted into a beam making an angle β with a linear chain of atoms with spacing a.

The above derivation can easily be generalized to three dimensions. If we consider three linear chains at right angles to each other and with interatomic spacings a, b and c (corresponding to an orthorhombic lattice as in YBCO), an incident beam will make angles α_1,α_2 and α_3 with the three chains, respectively. Similarly, the diffracted beam will make angles β_1,β_2 and β_3, respectively. We then find that the following set of three equations have to be satisfied simultaneously:

$$\begin{aligned} a\,(\cos(\beta_1) - \cos(\alpha_1)) &= p\lambda \\ b\,(\cos(\beta_2) - \cos(\alpha_2)) &= q\lambda \\ c\,(\cos(\beta_3) - \cos(\alpha_3)) &= r\lambda \end{aligned} \qquad (1)$$

where p,q and r are integers. In general, the reflection can be of different order along the three chains and p,q and r will thus be different. In contrast to the one dimensional case, this set of equations will only be satisfied simultaneously for particular values of α_i and β_i.

Equation (1) relates the angles of the incident and diffracted beams to the direction of the rows of atoms in the crystal. From an experimental point of view, it is much more convenient to express the condition for diffraction in terms of the angle 2θ between the undeviated incident beam and the diffracted beam, since this is the quantity which is most readily measured. In Figure 2.2 the two beams are shown together with a broken line bisecting the angle 2θ between them. Note that the broken line does not necessarily coincide with any of the three perpendicular chains of atoms mentioned earlier. The incident and diffracted beams have direction cosines $(\cos(\alpha_1),\cos(\alpha_2),\cos(\alpha_3))$ and $(\cos(\beta_1),\cos(\beta_2),\cos(\beta_3))$ as before. From a standard formula from solid

analytical geometry relating the angle between two lines to their direction cosines we get:

$$\cos(2\theta) = \cos(\alpha_1)\cos(\beta_1) + \cos(\alpha_2)\cos(\beta_2) + \cos(\alpha_3)\cos(\beta_3) \qquad (2)$$

If we square the three equations in (1), add them together and use a simple trigonometric identity we get:

$$\lambda^2\left(\left(\frac{p}{a}\right)^2 + \left(\frac{q}{b}\right)^2 + \left(\frac{r}{c}\right)^2\right) = 2 - 2\left(\cos(\alpha_1)\cos(\beta_1) + \cos(\alpha_2)\cos(\beta_2) + \cos(\alpha_3)\cos(\beta_3)\right)$$

The term in parenthesis on the right is identical to cos(2θ) (from(2)). Using the identity $1 - \cos(2\theta) = 2\sin^2(\theta)$ we can further simplify the equation:

$$\lambda^2\left(\left(\frac{p}{a}\right)^2 + \left(\frac{q}{b}\right)^2 + \left(\frac{r}{c}\right)^2\right) = 4\sin^2(\theta)$$

By taking the greatest common divisor n of p,q and r outside the parenthesis on the left we arrive at:

$$n\lambda = \frac{2}{\sqrt{\left(\frac{p'}{a}\right)^2 + \left(\frac{q'}{b}\right)^2 + \left(\frac{r'}{c}\right)^2}}\sin(\theta) \qquad (3)$$

We have now formulated the condition for diffraction in terms of the angle θ and the integers p',q' and r'. It can be shown that these integers are the Miller indices for the plane bisecting the angle 2θ between the undeviated incident beam and the diffracted beam. One can then think of the diffraction process as a reflection of the X-ray beam in a set of lattice planes. This is the idea behind the alternative derivation of the condition for diffraction, due to Bragg. Indeed, by realizing that in an orthorhombic lattice with lattice constants a, b and c, the spacing d between lattice planes with Miller indices (h,k,l) is just $d = ((h/a)^2 + (k/b)^2 + (l/c)^2)^{-1/2}$, equation (3) reduces to the Bragg formula:

$$n\lambda = 2d\sin(\theta)$$

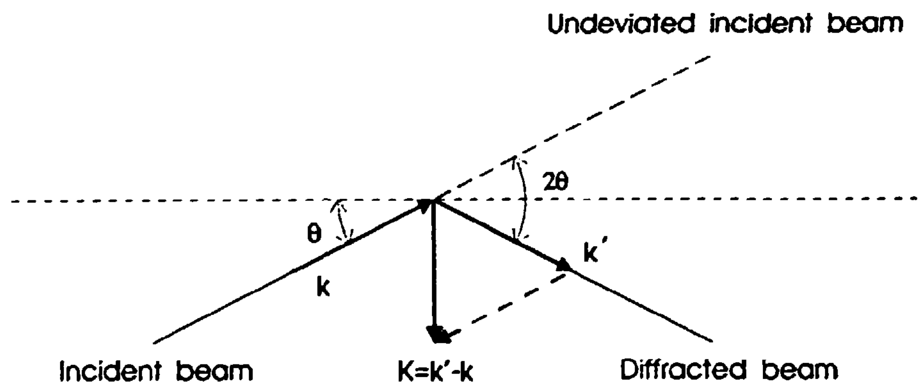

Figure 2.2 This figure shows the relation between the incident beam with wave vector k, the diffracted beam k' and the vector difference K=k'-k.

The preceding discussion describes the 'iffraction phenomenon in real space, since this approach is useful for illustrating the underlying physics. It is possible instead to formulate the condition for diffraction in terms of the

reciprocal lattice. The reciprocal lattice corresponding to a given Bravais lattice can be defined in terms of a plane wave exp(i(k· r). The vectors of the reciprocal lattice are all those vectors τ which give the plane wave the same periodicity as the Bravais lattice[1], i.e. it is all those vectors for which exp(i(τ·R)) = 1. The reciprocal lattice is described by three reciprocal lattice vectors **a***, **b*** and **c***, which are related to **a**, **b** and **c** by:

$$a^* = 2\pi\frac{b\times c}{a\cdot(b\times c)} \qquad b^* = 2\pi\frac{c\times a}{a\cdot(b\times c)} \qquad c^* = 2\pi\frac{a\times b}{a\cdot(b\times c)}$$

Formulating the condition for diffraction in terms of the reciprocal lattice is often very useful in practice, since the condition can be interpreted in terms of a reciprocal lattice vector. According to the above definition of the reciprocal lattice, for any set of lattice planes in the direct lattice separated by a distance d, there is a reciprocal lattice vector perpendicular to the planes with length 2π / d. Consider the incident beam and the diffracted beam both making an angle θ with the diffracting lattice plane as shown in Figure 2.2. We characterize the beams in terms of their wave vector **k** and **k'**, respectively. Because we are only concerned with elastic scattering of X-rays we have |**k**| = |**k'**|. From the figure we see that the difference **K** = **k'** - **k** in the wave vector describing the incident and the diffracted beam is perpendicular to the diffracting plane, i.e. **K** is parallel to a reciprocal lattice vector. Furthermore, we see that the length of **K** is K=2 k sin (θ). With k = 2π / λ, we get K = 2π × 2 sin (θ) / λ. By comparing this expression with the Bragg condition for diffraction, we see that we get a diffracted beam only when K/(2π) = n/d, i.e. when K = n × 2π/d. This last equation states that we get diffraction with scattering vector **K** from a set of lattice planes separated by a distance d only if **K** is an integral number of the reciprocal lattice vector corresponding to this set of planes. This formulation of the condition for diffraction is due to von Laue. Formally, it can be expressed as exp(i**K**· **R**) = 1, where **R** is a vector of the direct lattice. Diffraction occurs when this relation holds for all vectors **R** of the direct lattice, and the intensity I(**K**) of the diffracted beam can then be calculated as a summation over all **R**:

$$I(K) = |\sum_{j=1}^{N'} f' e^{iK\cdot R_j}|^2 \qquad (4)$$

where f' is a measure of the cross section for scattering of an X-ray beam by an electron and N' is the total number of lattice points in the crystal.

The preceding discussion was based on a model of the crystal consisting of single electrons sitting at the points of a simple Bravais lattice. However, real crystals consist of one or more kinds of atoms arranged in a periodic structure, which is usually more complicated than a simple Bravais lattice. To deal with these additional complexities, one introduces the atomic form factor f and the concept of a lattice with a basis. The atomic form factor accounts for the fact that different atoms scatter the X-rays with different probability, that in general more than one electron per atom participate in the scattering process and that the atoms have a finite spacial extension. The form factor f_k for the atom on site k is a function of **K**, i.e. $f_k=f_k(K)$. The basis of a given material consists of two or more atoms or ions and has the property that when it is repeatedly translated through vectors belonging to a Bravais lattice it will reproduce the crystal structure of the material. The vectors **R** in (4) can then be decomposed

into two vectors $\mathbf{R} = \mathbf{R}' + \mathbf{r}'$, where $\mathbf{R}'$ describes the position of the basis in the Bravais lattice and $\mathbf{r}'$ describes the position of the atom within the basis. The summation in (4) can thus be rewritten as:

$$I(\mathbf{K}) = |\sum_{j=1}^{N} e^{i\mathbf{K}\cdot\mathbf{R}_j} \sum_{k=1}^{M} f_k e^{i\mathbf{K}\cdot\mathbf{r}_k}|^2 \qquad (5)$$

The last sum in (5) is over all atoms or ions in the unit cell and is referred to as the structure factor. By evaluating this quantity for a given crystal structure one finds that not all possible Bragg reflections occur. For instance, for the body centered cubic structure only reflections from lattice planes having an even sum of the Miller indices ($h+k+l = 2n$) are observed. The first sum is zero in general, except when **K** is a reciprocal lattice vector, in which case the square of the sum is a delta function (for $N \to \infty$).

2.2 Experimental techniques

The experiments were carried out in the X-ray basement at Risø using the Rigaku 12 kW rotating anode X-ray source. Figure 2.3 shows the layout of the diffractometer and the path of the beam from source to detector. The intensity versus wavelength spectrum for the beam emitted from the anode A consists of a number of strong lines at wavelengths, that are characteristic for the anode material, superimposed on a continuous spectrum. The monochromator M is used to select one of the strong lines from the spectrum. In our case we have used Cu as anode material and we have used a pyrolitic graphite crystal as monochromator. The K_α line from Cu has a wavelength of λ=1.542 Å and it is selected by adjusting the monochromator for the graphite (002) reflection (d-spacing 3.354 Å). The beam continues to the sample, where it is diffracted one more time before it reaches the detector. This layout is referred to as a double axis spectrometer, since both the sample and the detector arm can be rotated around their vertical axes.

The resolution of the spectrometer, i.e. the minimum distance in 2θ between two reflections that the spectrometer can distinguish between, is determined by a number of factors. These factors include the wavelength spread in the X-ray source (the Cu K_α line is actually a doublet consisting of the Cu $K_{\alpha 1}$ line at λ=1.5405 Å and the Cu $K_{\alpha 2}$ line at λ=1.5443 Å), the mosaic spread of the monochromator (0.3° in our case) and the widths of the slits. It is possible to calculate a theoretical value of the resolution by folding together the contribution from each of these factors. However, we have simply determined the resolution experimentally by mounting a single crystal MgO substrate at the sample position, assuming that the mosaic spread of the MgO crystal is much less than the resolution of the spectrometer. With a distance of 100 cm between the sample and the detector and with a 4 mm wide slit in front of the detector, we find a resolution of 0.25°, defined as the width of the MgO (200) reflection at half its maximum intensity (Full Width at Half Maximum or FWHM), for scans in the longitudinal direction, and a resolution of 0.17° in the transverse direction. In longitudinal scans the angle of the detector and the sample are changed on the ratio 2:1 such that the direction of the scattering vector remains fixed with respect to the sample; varying the angle in this way will change only the length of the scattering vector. The direction of a transverse scan is perpendicular to the direction of a longitudinal scan.

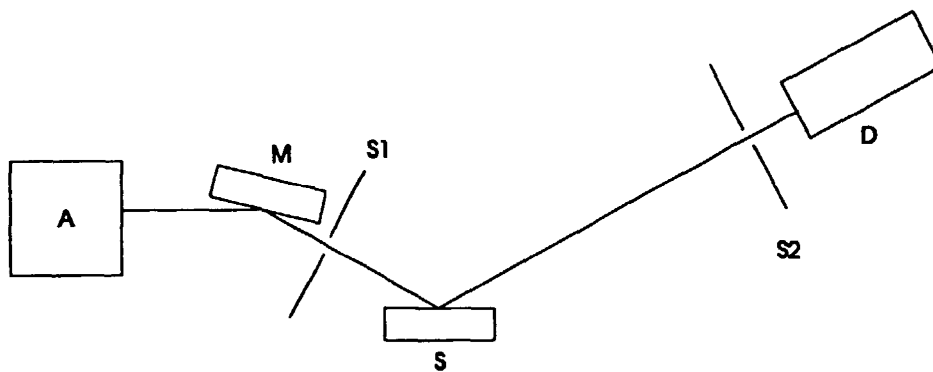

Figure 2.3 The physical layout of the spectrometer is shown here. The beam is diffracted two times before it reaches the detector.

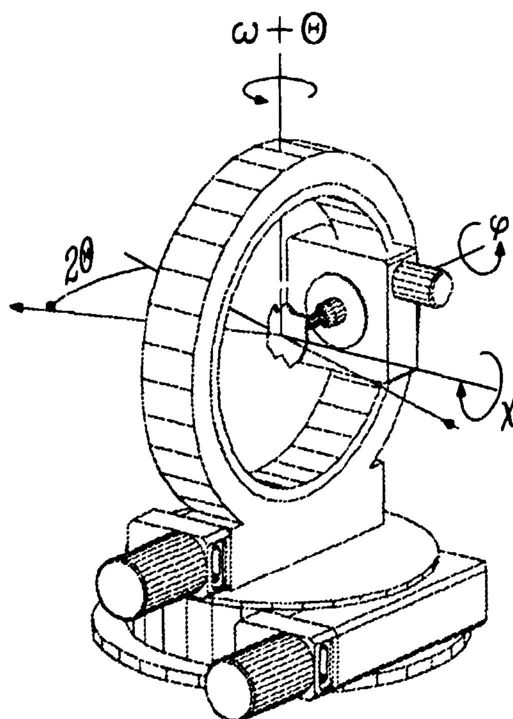

Figure 2.4 This figure shows how the four angles ω, 2θ, χ and φ are defined in relation to the four circle.

In our experiments the sample was mounted on a four-circle as shown in Figure 2.4. This allows rotation of the sample not only around the θ-axis, but also around two additional axes, denoted by χ and φ, as shown in the figure. The fourth angle involved is ω. The angle between the incident beam and the diffracting planes is $\omega+\theta$, i.e. in a traditional θ-2θ scan ω is equal to zero. By using a four-circle the sample can be rotated freely and all reciprocal lattice vectors can be brought into the scattering plane, subject only to the mechanical constraints on the moving parts. This makes it possible to determine the texture (preferred crystallographic orientation) of crystalline materials[2]. The principle behind this type of measurement is that the θ- and 2θ-angles of the four-circle are kept fixed at the value corresponding to a given reflection from the

material in question. The χ- and φ-angles are then varied systematically. The resulting plot of the diffracted intensity as a function of χ and φ gives information about the orientation distribution of this particular reflection. In a highly textured sample we expect to see a significant intensity of the diffracted beam only in certain directions, whereas the diffracted intensity from a sample with little or no texture will be evenly distributed over all directions.

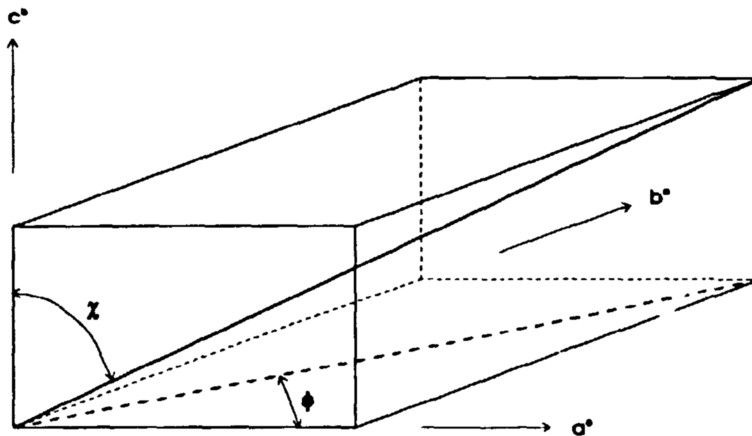

Figure 2.5 This figure shows how the (111) reflection can be brought into the scattering plane by two rotations around the φ- and χ-axis.

As an example of how we have used the four-circle in our experiments consider Figure 2.5, which shows a unit cell of the reciprocal lattice of YBCO growing c-axis oriented with respect to the MgO substrate, i.e. with its c-axis perpendicular to the surface of the substrate. A general reciprocal lattice vector $\tau = ha^* + kb^* + lc^*$ can be brought into the scattering plane by a rotation around the χ-axis followed by a further rotation around the φ-axis. The two angles are χ and φ are given by:

$$\chi = \arctan \frac{\sqrt{(ha^*)^2 + (kb^*)^2}}{lc^*}$$

$$\varphi = \arctan \frac{kb^*}{ha^*}$$

The relative orientation of the film with respect to the substrate can be determined by locating a reflection from the substrate in a similar fashion. In particular, we can determine the relative in-plane orientations, which is not possible using only standard θ-2θ scans.
We conclude the discussion of the four-circle by giving the χ- and φ-angles for the (103), (113) and (102) reflections from YBCO. This material has the direct lattice parameters a = 3.82 Å, b = 3.88 Å and c = 11.67 Å. However, because the films are always twinned (to be discussed later), we use a = b = 3.85 Å, i.e. $a^* = b^* = 1.63$ Å^{-1} and $c^* = 0.538$ Å^{-1}. We find $\chi_{103} = 45.3°$, $\chi_{113} = 55.0°$

and χ_{102} = 56.6°. Because the multiplicity of each of these reflections is eight, we observe them at four different φ angles for $\varphi = n \times 90° + \varphi_0$, where φ_0 is an offset angle. By proper alignment we can choose φ_0 =0. The other four equivalent reflections occur for negative *l*-indices, which are inaccessible by the spectrometer.

2.3 Relation between epitaxy and critical current density

Application of superconducting thin films for electronic devices requires that they can support critical current densities on the order of 10^6 A/cm^2. For instance, if we require a 5 μm wide strip patterned into a 3000 Å thick film to carry a current of 5 mA at 77 K, which is not unreasonable, the critical current of the film must be at least 3.3×10^5 A/cm^2 at this temperature. At the present time the deposition techniques have evolved to the point where these current densities can be obtained routinely. This success has been achieved in part as a result of investigations of the type described in this chapter, demonstrating that the critical current density in the thin films is strongly dependent on their crystallographic and especially their microstructural properties.

Several groups have measured the texture in YBCO films[3,4,5,6,7,8] deposited on $SrTiO_3$, $LaAlO_3$, MgO and YSZ substrates by laser ablation and rf sputtering. They find that c-axis oriented films grown on the first two substrates have their a-b axes perfectly aligned with the corresponding axes of the substrate. This is easily explained by the nearly perfect lattice match between YBCO and these two materials. For the MgO substrate, which has about 9.5 % mismatch to YBCO, it is found that sometimes a few percent of the film grows with its [110] direction parallel to the [100] direction of the substrate. For YSZ this effect was even more pronounced. This is understandable, since YBCO and YSZ have a mismatch of about 33 %. A $\sqrt{2} \times \sqrt{2}$ supercell of YBCO, on the other hand, has a mismatch of only 5.9 % to YSZ. Besides the in-plane misorientations it is sometimes found that the film grows with its c-axis parallel to the substrate surface (referred to as a-axis oriented growth). This type of film growth is usually found on the substrates that have a good lattice match to YBCO in the a-b plane, i.e. on $SrTiO_3$ and $LaAlO_3$ substrates. These substrates can accommodate a-axis oriented films because their lattice parameters are close to ⅓ of the c-axis of YBCO.

Both of these types of defects lead to the creation of grain boundaries in the YBCO film. Although at present the nature of the grain boundaries in this material in not fully understood, it is well known that they exhibit reduced values of the critical current density compared to the intragrain critical current density. In the pioneering work by a group at IBM[9,10] it was found that all grain boundaries in YBCO act like Josephson junctions with a critical current density up to two orders of magnitude lower than the intragrain value, depending on the misorientation angle. In particular, it was found that 45° grain boundaries in the a-b plane have J_c reduced to about 2 % of the intragrain value. The Josephson junction behavior was inferred from the observation of current steps in the I-V characteristic under microwave irradiation. This conclusion has been disputed by Babcock et al[11] for the case of boundaries between a- and c- axis oriented grains. They find that although the critical current density is reduced, it is only weakly dependent on the

applied magnetic field, being reduced only by a factor of 2 at a field of 5 T. This is in contrast to Josephson junction behavior, where the Frauenhofer pattern $I_c = \sin(\phi/\phi_0) / (\phi/\phi_0)$ will lead to a reduction by several orders of magnitude in such high fields.

The cri'ical current density in YBCO is affected not only by the density of grain boundaries in the sample, but also by the density and strength of the flux pinning sites. YBCO is a type II superconductor, which means that it will allow penetration by flux vortices for applied magnetic fields above the lower critical field H_{c1}, while remaining superconducting outside the vortices. This mixed state persists until the applied magnetic field reaches the upper critical field H_{c2}, at which point the density of the vortices can not be increased further without overlap between individual vortices. At this point the superconductivity is destroyed. Once t'ie flux has penetrated the sample, it is important that it is pinned with sufficient strength to prohibit motion under the influence of the Lorentz force. If the flux st rts to move, an electric field will be induced parallel to the direction of t, current flow, with the dissipation of heat as a consequence.

The issue of flux pinning and flux motion in high T_c superconductors is not fully understood at present. It is generally agreed that structural defects in the samples can act as pinning sites, because the superconducting order parameter is already partially or fully depressed at these sites. Consequently, there has been some interest in experiments designed to increase the density of such defects by irradiating the sample with neutrons, protons, oxygen ions etc. Some success has been achieved in this respect. For instance, van Dover[12] et al report an increase in J_c by two orders of magnitude (from 6.5×10^3 A/cm^2 to 6.2×10^5 A/cm^2) at 77 K in neutron irradiated single crystals of YBCO. For epitaxial thin films the improvements are much more modest; Siegal[13] et al have reported an increase by a factor of two in YBCO thin films irradiated by $^{135}Xe^+$ ions. This difference between single crystals and thin films can be related to at least two observations. First, the irradiation process have a tendency to reduce the critical current density of the grain boundaries in the fi'ms and thus partially offset the gain in the intragrain J_c. By definition, there are no grain boundaries in single crystals. Second, when the unirradiated samples are compared, it is generally found that the J_c of thin films are several orders of magnitude higher than that of single crystals. This difference is not understood, but must somehow be related to an unidentified pinning mechanism[14] which is present only in the thin films. This pinning mechanism could for instance be induced by the substrate or by differences in the twin boundary density.

The degree of single crystallini y is found to affect not only the critical current density, but also several other properties of YBCO thin films. For instance, Hiskes[15] et al find that the microwave surface resistance R_s of metal organic chemical vapor deposited films correlates with the amount of a-axis oriented material. In another study[16] it was found that high-angle grain boundaries in the a-b plane corresponding to only 4 % of the volume fraction of the film being misaligned can lead to increases in R_s by a factor of 25. Besides R_s, also the resistivity in the normal state ρ_n, and the width of the superconducting transition ΔT_c are adversely affected by deviations from perfect crystalline order[17].

2.3.1 Influence of structural defects in the film

In this section and the following (2.3.2) we will describe the results of our measurements[18] on four YBCO thin films deposited by laser ablation at NKT Research Center. Two of these films were deposited on MgO substrates (supplied by Harrick Scientific) while the other two were deposited on $SrTiO_3$ substrates (supplied by Kristalhandel Kelpin). During deposition the laser was adjusted to give an intensity of 300 MW/cm^2 at a wavelength of 355 nm and with a pulse length of 5 ns. The substrates were held at 750°C in 1 mbar oxygen ambient. After deposition the oxygen pressure was raised to 1 atm, and the films were cooled to 600°C at a rate of 100°C/min and further to room temperature at a rate of 10°C/min. The onset of superconductivity was measured at 90.5 K with a transition width of 1.5 K. In Table 2.1 we have summarized the critical current densities and some of the results from our diffraction measurements for the four films. The third column of the table specifies the FWHM for a transverse scan through the YBCO (005) reflection. This type of scan gives information about the width of the angular distribution of the c-axes. Similarly, the angular distribution of the a- and b-axes can be determined by doing scans in φ on the (102) or (103) reflection and the result of this measurement is given in the fourth column. Finally, in the fifth column, we specify the value of the orthorhombic splitting ε, defined as $\varepsilon=2(b-a) / (b+a)$. We will later return to this issue; at this point we simply note that with a=3.82 Å and b=3.88 Å we get ε=1.56 %. Since our measured values of ε is in good agreement with this number, we can conclude that either the films are not strained (most likely) or they are strained in such a way as to preserve the orthorhombic splitting.

Substrate material	J_c at 77 K (A/cm^2)	YBCO (005) Transverse scan FWHM (°)	In-plane mosaicity (°)	Orthorhombic splitting ε (%)
MgO	3.7×10^5	0.82	0.85	1.58
MgO	1.5×10^6	0.49	0.86	1.41
$SrTiO_3$	2.9×10^6	0.29	0.46	1.58
$SrTiO_3$	1.0×10^7	0.28	0.31	1.57

Table 2.1 This table summarizes the measured critical current densities and crystallographic properties of the four films.

In Figure 2.6 we show θ-2θ scans for the two films deposited on $SrTiO_3$ substrates. The scan on the left is from the film having $J_c=1.0 \times 10^7$ A/cm^2 at 77 K. Besides a small YBCO (200) reflection at 2θ = 47.6° (and the inevitable substrate reflections) we see only the (00*l*) reflections from the film, indicating that it grows predominantly c-axis oriented. A small fraction of the film is a-axis oriented as revealed by the (200) reflection, but there is no randomly oriented material present, since this would have resulted in a (103) reflection at 2θ = 32.7°. The scan shown on the right is from the film having

J_c=2.9 × 10^6 A/cm² at 77 K. This scan is qualitatively identical to the scan on the left. Quantitatively, we note that the relative height of the YBCO (200) reflection is higher in the scan on the right, indicating that a larger fraction of the film is a-axis oriented. In principle, it is possible to determine the relative fractions of a-axis oriented material in the two films from the θ-2θ scans. This would involve a calculation of the ratio of the integrated intensities of the (200) and, say, the (005) reflections, taking the structure factors into account. However, the ratio between a- and c-axis oriented material can be found much more conveniently by doing a χ-scan on the (102) reflection. Referring to Figure 2.5 it is easy to see that, if this reflection occurs at $\chi_{102,c}$ = 56.6° for c-axis oriented material, then it will occur at $\chi_{102,a} = 90 - \chi_{102,c}$ = 33.4° for a-axis oriented material. The YBCO (103) reflection, even though it is stronger, is not suited for this type of scan since the difference in χ-angle would only be about 1° in the two cases.

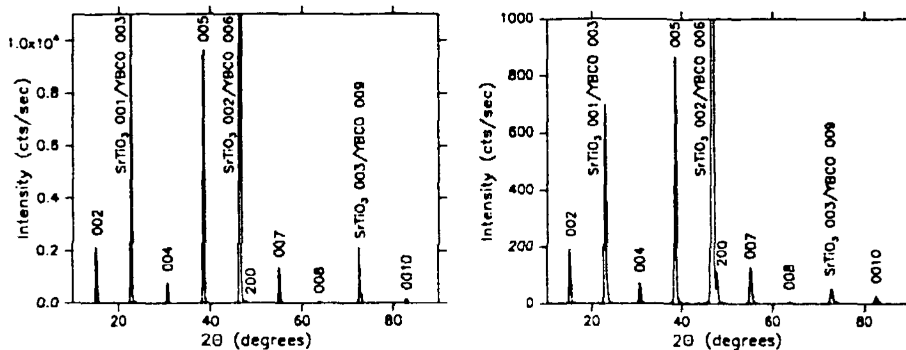

Figure 2.6 θ-2θ scans for the two films deposited on $SrTiO_3$ substrates. Left: J_c=1.0 × 10^7 A/cm² at 77 K. Right: J_c=2.9 × 10^6 A/cm² at 77 K.

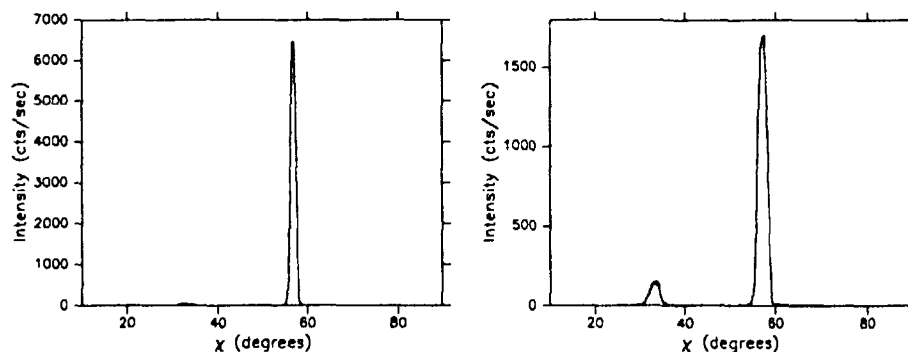

Figure 2.7 χ-scans for the same two films as in Figure 2.6. Clearly, there is more a-axis oriented material in the low J_c film shown on the right.

In Figure 2.7 we show χ-scans corresponding to the θ-2θ scans in Figure 2.6, i.e. the film with the high J_c is on the left. In both scans there is clearly a peak both at χ = 56.6° and at χ = 33.4°. However the ratio between the integrated intensities of these two peaks is 0.6 % and 8.3 %, respectively. Since no other defects were found in these two films (no randomly oriented material, no

impurity phases, no in-plane misalignments) and since the angular distribution of the a- b- and c-axes are essentially identical as indicated in Table 2.1, we attribute the reduction of J_c by 70 % in the film in the right most scans in Figures 2.6 and 2.7 to the increased amount of the a-axis oriented material.
Next we turn to the films deposited on MgO substrates. In Figure 2.8 we show the θ-2θ scan for the two films. The scan on the left is from the film having $J_c=1.5 \times 10^6$ A/cm^2 at 77 K, while the scan on the right is from the film having $J_c=3.7 \times 10^5$ A/cm^2 at 77 K. The two scans are virtually identical, except that the absolute intensity is a bit lower for the low J_c film. Both scans reveal only (00*l*) reflections from YBCO, i.e. there is no a-axis oriented material and also no randomly oriented material in either of the films. Nevertheless, the critical current densities differ by 75 %.

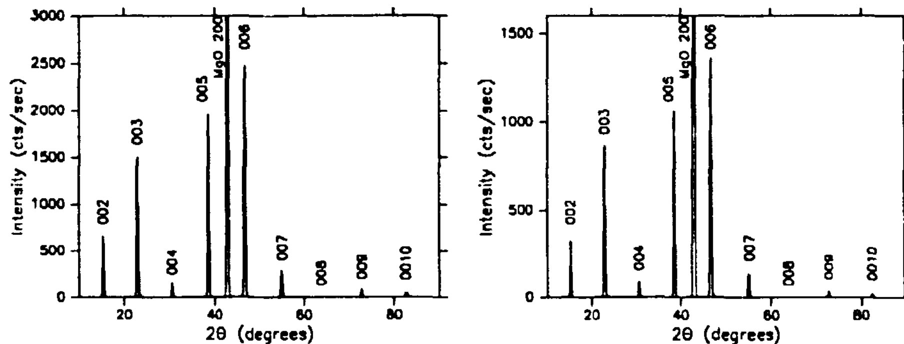

Figure 2.8 θ-2θ scans for the two films deposited on MgO substrates. Left: $J_c = 1.5\times10^6$ *A/cm²*. *Right:* $J_c = 3.7\times10^5$ *A/cm²*.

The cause of the reduced critical current density becomes apparent if one does a pole figure measurement on the two films. In Figures 2.9 and 2.10 we show partial pole figures for the high J_c and low J_c film, respectively. These pole figures were recorded with ω and 2θ adjusted to the YBCO (103) reflection. The azimuthal angle φ was defined by means of the substrate such that φ=0 when the spectrometer was adjusted to one of the four degenerate MgO (202) reflections. This allows us to determine the orientation of the film with respect to the substrate. The pole figure in Figure 2.9 for the high J_c film is seen to consist of four peaks at χ=45.5° and at φ=0°,90°,180° and 270°. The pole figure in Figure 2.10 for the low J_c film displays the same four main peaks, but in addition it has four smaller peaks at χ=45.5° and φ=45°,135°,225° and 315°. The intensity of the smaller peaks is about 5 % of the main peaks. The straight forward interpretation of these pole figures is that in the high J_c film essentially all the material is oriented with its a-b axes parallel to the a-b axes of the substrate (because the YBCO (103) reflection is aligned with the MgO (202) reflection), whereas in the low J_c film about 5 % of the material is oriented with its a-b axes along the [110] direction of the substrate.

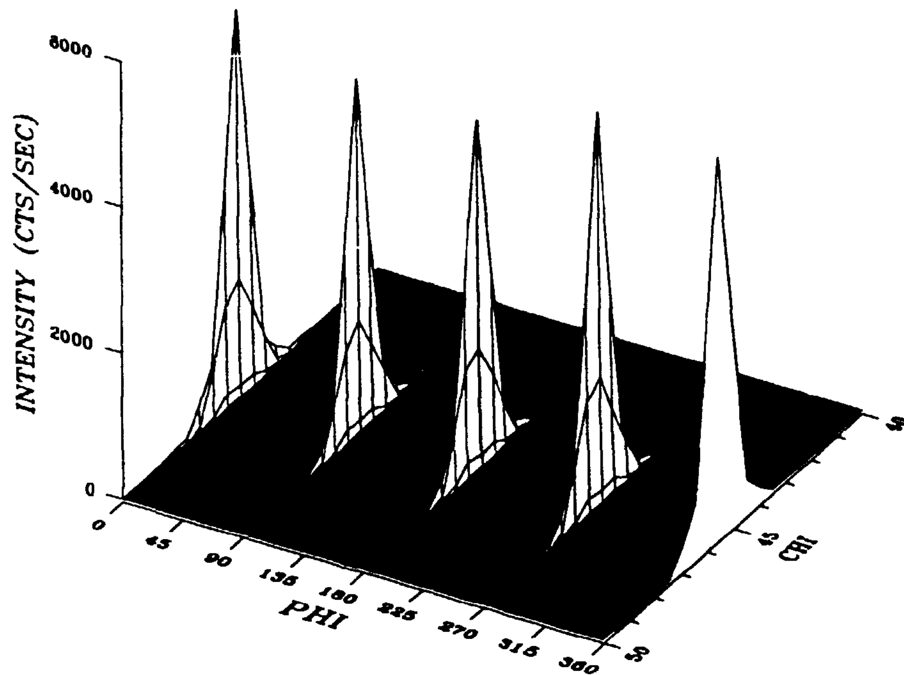

Figure 2.9 Partial pole figure for the YBCO film on MgO having $J_c = 1.5 \times 10^6$ A/cm^2 at 77 K. The positions of the peaks indicate that all the material in the film is aligned with the substrate.

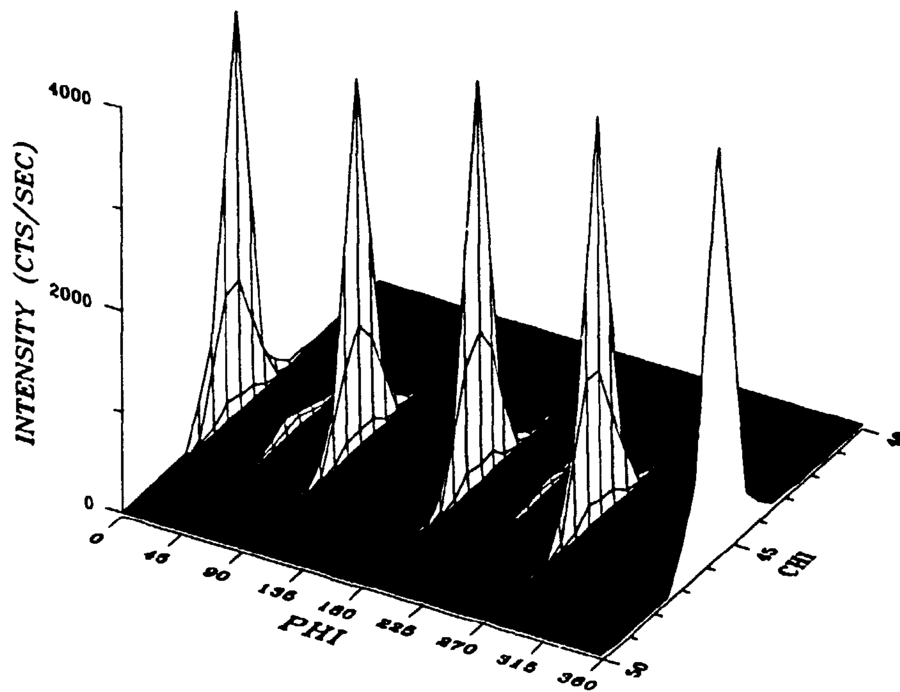

Figure 2.10 Partial pole figure for the YBCO film on MgO having $J_c = 3.7 \times 10^5$ A/cm^2 at 77 K. The positions of the peaks indicate that most of the material in the film is aligned with the substrate, but about 5 % is rotated 45° with respect to the dominant orientation.

The two films deposited on MgO substrates have been subjected to a further study by transmission electron microscopy (TEM) at the Materials Department at Risø. In Figure 2.11 we show electron micrographs of the films, again with the high J_c film on the left and the low J_c film on the right. The low J_c film exhibits a fine-grained structure with a grain size of around 200 nm. Most grains have [001] approximately perpendicular to the foil. The grains contain microtwins with a width of approximately 30 nm. The orientations of the microtwins indicate that most of the grain boundaries are small-angle boundaries. This is corroborated by selected area diffraction patterns from areas containing several grains. These patterns indicate a typical misorientation of up to 2° rotation around [001]. Microdiffraction patterns from neighbouring single grains show rotation of the same magnitude about an axis in the film plane. Grains with a larger rotation about an axis perpendicular to the film are, however, also found, and among these a substantial fraction has a misorientation close to 45°.
The high J_c film exhibits a structure with most of the material being without grain boundaries over large areas. The microtwins in this specimen have a transverse width of approximately 60 nm and were found to have the same orientations parallel to either [110] or [$1\bar{1}0$] over large areas.
The results from the X-ray diffraction and TEM investigations are thus seen to complement each other and we conclude that the reduced current density results as a combination of the presence of high-angle boundaries and the much higher density of small-angle grain boundaries in the low J_c film.

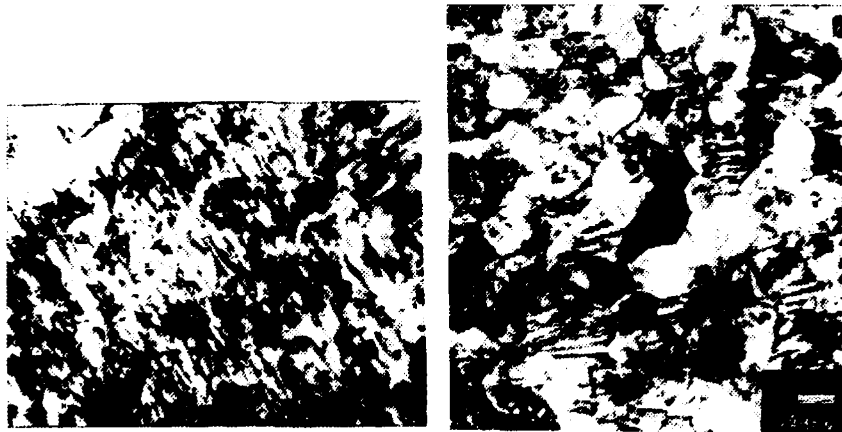

Figure 2.11 Left: Electron micrograph of the high J_c film on MgO showing a structure with no grain boundaries over large areas. Right: Electron micrograph of the low J_c film on MgO, showing a fine-grained structure with a grain size of about 200 nm and a high density of small-angle grain boundaries.

2.3.2 Influence of the substrate

Twinning is commonly observed in materials that have two nearly identical crystallographic axes as in YBCO, where the relative difference in length between the a- and b-axis is 1.5 %. Physically, the phenomenon manifests itself by an interchange of the two nearly identical axes at more or less regular

intervals. In the context of epitaxial thin film growth on cubic single crystal substrates (as in the case of YBCO films on MgO or $SrTiO_3$ substrates) the formation of twin domains relieves the strain that would otherwise result if the lattice parameters of the substrate were imposed on the thin film.
The formation of twin domains has certain consequences that can be observed experimentally by X-ray diffraction. This is illustrated in Figure 2.12. The square drawn with a solid line shows the a-b plane of a tetragonal unit cell with parameters $a=b=a_0$. The distortion to an orthorhombic unit cell can be described by the parameter ε by letting $a = (1-\varepsilon/2)\ a_0$ and $b = (1+\varepsilon/2)\ a_0$. The two rectangles drawn with broken lines (Figure 2.12, left) shows the two possible configurations of the orthorhombic unit cell given that the direction of the diagonal has to remain fixed with respect to the tetragonal unit cell (for $\varepsilon<<1$ the length of the diagonal remains essentially unchanged). This is referred to as twinning along the [110] direction. Similarly, the twinning can occur along the [1$\bar{1}$0] direction as shown on the right in Figure 2.12. Note that in the figure we have exaggerated the effect for illustration purposes by choosing ε=20 %. The net effect of the twinning is that a reflection with Miller indices $(h,0,l)$ is split up into four reflections with indices $(h\ (1\pm\varepsilon/2), \pm\varepsilon/2, l)$. Similarly, a reflection with indices $(0,k,l)$ is split up into four reflections at $(\pm\varepsilon/2, k(1\pm\varepsilon/2), l)$.

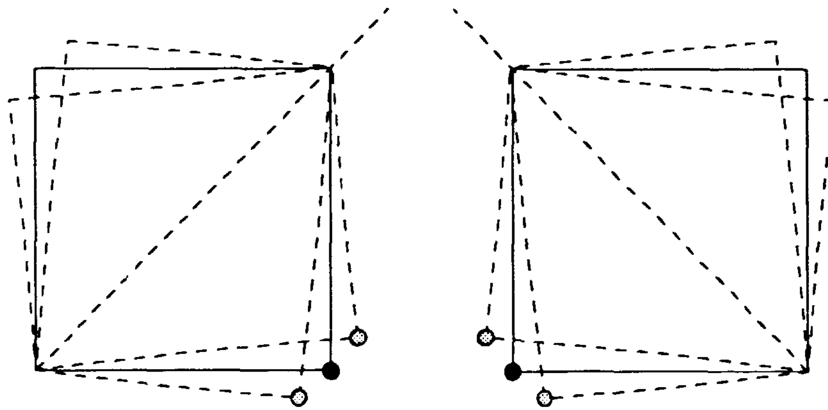

Figure 2.12 Left: This figure illustrates how the twinning along the [110] direction splits up the (h,0,l) reflection (indicated by the black dot) into two reflections at $(h(1-\varepsilon/2), -\varepsilon/2, l)$ and $(h(1+\varepsilon/2), \varepsilon/2, l)$. Right: Similarly, the twinning along the [1$\bar{1}$0] direction splits the (h,0,l) reflection into two reflections at $(h(1+\varepsilon/2), -\varepsilon/2, l)$ and $(h(1-\varepsilon/2), \varepsilon/2, l)$.

If we go to high enough Miller indices, the splitting described above can be resolved with the spectrometer. In Figures 2.13 and 2.14 we show scans in reciprocal space around the (304) reflection from YBCO for the two high J_c films on $SrTiO_3$ and MgO substrates, respectively. In Figure 2.13 we see four peaks as expected, but in Figure 2.14 the peaks have merged together in the azimuthal direction, leaving only two broad peaks behind. The orthorhombic

splitting can be determined by such scans either along the [100] direction or the [010] direction in reciprocal space. Since the splitting is easily resolved in the [100] direction in all cases, we have determined ε in this way for all the films with the result given in Table 2.1, as mentioned earlier.

Scans along the [010] direction, on the other hand, can be used to determine the angular distribution of the a-b axes. This is because of the fact that for any scan in reciprocal space from $(h,-y,l)$ to (h,y,l) through a lattice point $(h,0,l)$ where $y \ll 1$, the direction of the scan will be perpendicular to the scattering vector and thus the scan will be equivalent (almost) to a φ-scan. Because of the twinning, we should expect to see two peaks displaced φ_0 in φ and each with an intrinsic width $\Delta\varphi$. From the discussion of Figure 2.12, it should be clear that φ_0 is given by φ_0 = Arctan ε = 0.89°. In Figure 2.13 we see clearly two peaks along the k-direction and we can thus determine $\Delta\varphi$ directly from the FWHM of each peak. From the scan we get FWHM = 0.377° and corrected for the instrument resolution in φ (0.21°) we arrive at $\Delta\varphi$ = 0.31° as quoted in Table 2.1. A similar calculation for the low J_c film on $SrTiO_3$ gives $\Delta\varphi$ = 0.46°. For the two fiims deposited on MgO substrates it was not possible to resolve the two peaks in the k-direction. We interpret this as a result of the intrinsic width $\Delta\varphi$ of the peaks being comparable to the separation φ_0 between them. In that case we should see just one peak with FWHM = $((\varphi_0+\Delta\varphi)^2 + (\varphi_{res})^2)^{1/2}$, where φ_{res} is the instrument resolution. From the scan in Figure 2.14 we get FWHM = 1.76° and thus $\varphi_0+\Delta\varphi$ = 1.75°, i.e. $\Delta\varphi$ = 0.86°. A similar calculation for the low J_c film gives $\Delta\varphi$ = 0.85°.

Comparing the two scans in Figures 2.13 and 2.14, it is clear that the angular distribution of the a- and b-axes is significantly wider in the film on MgO than in the film on $SrTiO_3$. We attribute the smaller width on $SrTiO_3$ to the closer lattice match between YBCO and $SrTiO_3$. The wider distribution on MgO reflects that the average small-angle grain boundary on this type of substrate in general is higher than the average small-angle grain boundary on $SrTiO_3$. It is therefore possible that the small-angle grain boundaries tend to reduce the critical current density more on MgO than on $SrTiO_3$ and this is most likely the reason for the generally lower critical current densities observed on MgO compared to $SrTiO_3$.

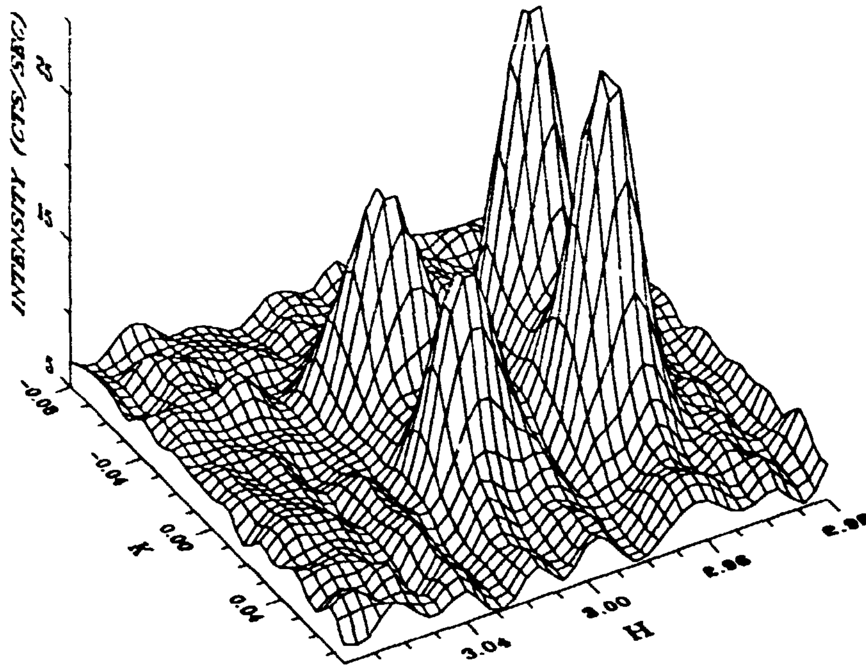

Figure 2.13 Detailed scan of the region around the (304) reflection of YBCO for the high J_c film on $SrTiO_3$. The four-fold splitting is easily resolved.

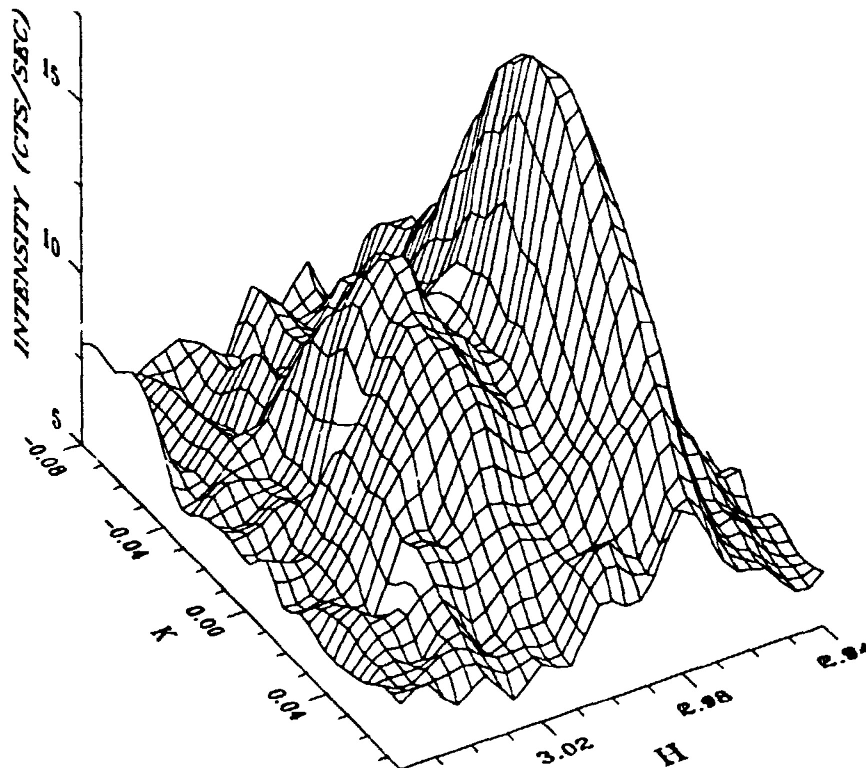

Figure 2.14 Detailed scan of the region around the (304) reflection of YBCO for the high J_c film on MgO. The splitting in the azimuthal direction is masked because of the wider angular distribution of the a-b axes on this substrate.

2.4 Conclusions

In this chapter we have described the results of our measurements of the crystalline order in YBCO thin films deposited on MgO and $SrTiO_3$ substrates. We have shown that the films all grow predominantly c-axis oriented and as such appear almost identical in a θ-2θ scan. However, by using a four-circle it is possible to perform other types of scans which clearly bring out the differences between the films. In this way we have identified two types of structural defects which both correlate with reduced critical current densities of the films. For films grown on MgO substrates we find that a film with 5 % of its grains rotated 45° around an axis perpendicular to the substrate and a high density of small-angle grain boundaries has J_c reduced by 75 % compared to a film with no 45° grain boundaries and a low density of small-angle grain boundaries. For films grown on $SrTiO_3$ substrates we find that an increase in a-axis oriented material from 0.6 % to 8.3 % results in a reduction of J_c by 70 %. In general, we find higher critical current densities on $SrTiO_3$ than on MgO substrates. This fact is attributed to the closer lattice match of YBCO to $SrTiO_3$. As a result of this, the average small-angle grain boundary is smaller on $SrTiO_3$ than on MgO (the mosaic spread in the a- and b-axes is only 0.38° for the best film on $SrTiO_3$ versus 0.86° for the best film on MgO), and consequently, it has less detrimental effect on J_c.
The four-circle has proven to be very useful, not only for basic structural characterization, as described here. It turns out that, because of their weak-link character, the 45° misorientations described in this chapter can be used as a primitive form of Josephson junctions. For that purpose it is necessary to find a reasonably reliable fabrication process to create the misorientations at will. We have used the four circle extensively (particularly its ability to perform φ-scans) during the development of such a process, as we shall see in the next chapter.

References

[1] N.W. Ashcroft and N.D. Mermin: "Solid state physics", (Holt-Saunders, New York, 1976).

[2] H.R. Wenk: "Preferred orientation in deformed metals and rocks: An introduction to modern texture analysis", (Academic Press, Orlando, 1985).

[3] J.P. Zheng, S.Y. Dong and H.S Kwok. Appl. Phys. Lett., 58 (1991), 540.

[4] Y.-L. He, C.-G. Wang, A.J. Drehman and H.-S. Jin. J. Appl. Phys., 67 (1990), 7460.

[5] A. Perrin, M.G. Karkut, M. Guilloux-Viry and M. Sergent. Appl. Phys. Lett., 58 (1991), 412.

[6] J. Sizemore, R. Barton, A. Marshall, J.C. Bravman, M. Naito and K. Char. IEEE Trans. Mag., 25 (1989), 2245.

[7] S.E. Russek. D.K. Lathrop, B.H. Moeckly, R.A. Buhrmann, D.H. Shin and J.Silcox. Appl. Phys. Lett., 57 (1991), 1155.

[8] D.H. Shin, J. Silcox, S.E. Russek, D.K. Lathrop, B. Moeckly and R.A. Buhrmann. Appl. Phys. Lett., 57 (1990), 508.

[9] D. Dimos, P. Chaudari, J. Mannhart and F.K. LeGoues. Phys. Rev. Lett., 61 (1988), 219.

[10] D. Dimos, P. Chaudari and J. Mannhart. Phys. Rev. B, 41 (1990), 4038.

[11] S.E. Babcock, X.Y. Cai, D.L. Kaiser and D.C. Larbalestier. Nature, 347 (1990), 167.

[12] R.B. van Dover, E.M. Gyorgy, L.F. Schneemeyer, J.W. Mitchell, K.V. Rao, R. Puzniak and J.V. Waszczak. Nature, 342 (1989), 55.

[13] M.P. Siegal, R.B. van Dover, J.M. Phillips, E.M. Gyorgy, A.E. White and J.H. Marshall. Appl. Phys. Lett., 60 (1992), 2932.

[14] J.E. Tkaczyk, C.L. Briant, J.A. DeLuca, E.L. Hall, P.L. Karas, K.W. Lay, E. Narumi and D.T. Shaw. J. Mater. Res., 7 (1992), 1317.

[15] R. Hiskes, S.A. DiCarolis, J.L. Young, S.S. Laderman, R.D. Jacowitz and R.C. Taber. Appl. Phys. Lett., 59 (1991), 606.

[16] S.S. Laderman, R.C. Taber, R.D. Jacowitz, J.L. Moll, C.B. Eom, T.L. Hylton, A.F. Marshall, T.H. Geballe and M.R. Beasley. Phys. Rev. B, 43 (1991), 2922.

[17] M.R. Beasley. Proc. IEEE, 77 (1989), 1155.

[18] R. Kromann, J.B. Bilde-Sørensen, R. de Reus, N.H. Andersen, P. Vase and T. Freltoft. J. Appl. Phys., 71 (1992), 3419.

3 SQUIDs and magnetometers

Two fundamentally different kinds of Superconducting QUantum Interference Devices exist, commonly referred to as the rf SQUID and the DC SQUID, respectively. The rf SQUID consists of a superconducting ring interrupted by one Josephson junction and it is operated with an rf bias current, typically in the 20-30 MHz range. The DC SQUID, in contrast, has two Josephson junctions and it is operated with a DC bias current. The former type is more widely used for practical applications, largely because of successful commercialization at an early point. However, in recent years it has been surpassed in performance by the DC SQUID, which has undergone extensive development with intrinsic energy sensitivities approaching the quantum limit. In this work we have focused exclusively on the DC SQUID and the rf SQUID will not be mentioned further.

3.1 Theory of the DC SQUID

3.1.1 Josephson junctions

The active element of the SQUID is the Josephson junction. This type of junction consists of two superconductors separated by an insulating barrier. When the thickness of the barrier is on the order of a few tens of Å, electrons can tunnel through the barrier, not only as single electrons but also as Cooper pairs. The tunneling of Cooper pairs was predicted in 1962 by Brian Josephson[1] and was soon confirmed experimentally by Anderson and Rowell[2] in a tunnel junction of the sandwich type. This type of junction has since undergone an impressive evolution and with the advent of the Nb tri-layer process[3,4], it has reached a level of reliability which makes it possible to fabricate devices containing several thousand junctions[5]. Besides sandwich junctions several other kinds of junctions have been demonstrated. An excellent review of the physics of the Josephson junction, including fabrication methods and applications, has been given by Barone and Paterno[6].
The current-voltage characteristics for the Josephson junction can be derived by using the so-called resistively shunted junction (RSJ) model[7,8]. In this model, shown in Figure 3.1, the junction is approximated by an ideal Josephson element in parallel with a shunt resistor R and a self-capacitance C. The following relations hold for the ideal Josephson element:

$$I = I_0 \sin(\delta)$$
$$V = \frac{\hbar}{2e}\frac{\partial \delta}{\partial t}$$

where δ is the difference in the phases of the wave functions describing the two superconductors on either side of the barrier. The equations state that the element in the zero-voltage state can carry a current I less than or equal to the critical current I_0 by adjusting the phase difference accordingly. When I

exceeds I_0, the junction switches to the voltage state, where the phase evolves with time at a rate depending on the voltage (484 MHz/μV).
When the junction is biased with a current I we obtain the following equation from the RSJ model:

$$I = I_0 \sin(\delta) + \frac{V}{R} + C\frac{\partial V}{\partial t}$$

By introducing a new time variable $\theta=\omega_c t$ the equation can be rewritten as[9]:

$$\frac{I}{I_0} = \beta_c \frac{\partial^2 \delta}{\partial \theta^2} + \frac{\partial \delta}{\partial \theta} + \sin(\delta) \qquad (6)$$

where $\beta_c=\omega_c RC$ and $\omega_c=(2e/\hbar)RI_0$.

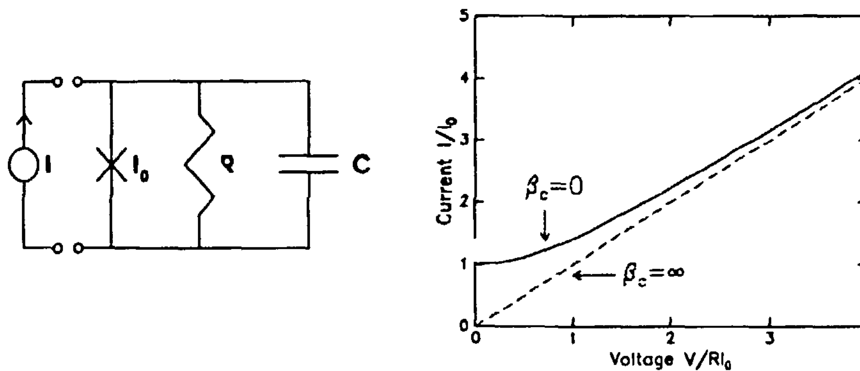

Figure 3.1 Left: The equivalent diagram for a Josephson junction according to the RSJ model. Right: I-V characteristics for the junction in the two limiting cases $\beta_c=0$ and $\beta_c=\infty$.

This equation describes the behavior of $\delta(t)$ in the general case. For $I<I_0$ it has the trivial solution $\delta(t)=\delta_0=\sin^{-1}(I/I_0)$ and thus V=0. When I exceeds I_0 a voltage develops across the junction and we have to solve (1) for $\delta(t)$ in order to be able to calculate V as the time average of $\partial\delta/\partial t$. For $\beta_c=0$ this can be done analytically giving:

$$V = RI_0\sqrt{\left(\frac{I}{I_0}\right)^2 - 1}$$

This curve, which corresponds to the situation where the self-capacitance of the junction is negligible, is shown in Figure 3.1 (solid line) together with its asymptotic value (dotted line) corresponding to the shunt resistance R.
In the general case where $\beta_c>0$, equation (6) must be integrated numerically. The effect of this non-negligible self-capacitance is to introduce hysteresis in the I-V characteristic for $\beta_c\geq1$. When I is increased from 0 the junction remains in the zero-voltage state until I reaches I_0, at which point the voltage jumps abruptly to a finite value. When the current is decreased, the junction remains in the voltage state until the current is reduced to a certain value $I_{min}<I_0$, which

depends on β_c. In the extreme case $\beta_c \rightarrow \infty$, I_{min} is zero and the I-V characteristic is then given by the dotted line in Figure 3.1.
This hysteretic behavior is undesirable for the operation of the SQUID. In low T_c SQUIDs based on tunnel junctions of the sandwich type the hysteresis is eliminated in the fabrication process by the addition of a shunt resistor of sufficiently low value. In high T_c SQUIDs based on grain boundary junctions, where the state of the art is much less advanced, one has essentially no control over the junction parameters, but luckily the nature of the grain boundary junctions is such that they are inherently non-hysteretic.
In the discussion above of the DC I-V characteristics it was tacitly assumed that the external magnetic field is zero. The application of external magnetic flux to the junction does not qualitatively alter the I-V characteristic, but leads to a reduction of the critical current. As discussed in Ref. 9, one finds that the I_c versus ϕ dependence for a high quality junction can be expressed in the form $I_c \propto \sin(\phi/\phi_0) / (\phi/\phi_0)$, i.e. it is equivalent to the Frauenhofer pattern produced by the diffraction of light passing through a narrow slit. The period in the pattern is the flux quantum $\phi_0 = h/2e = 2.07\times10^{-15}$ Wb. This quantity plays a crucial role in the operation of the SQUID, as we shall see in the next section.

3.1.2 Principle of operation of the SQUID

One of the most striking features of superconductivity is the fact that this inherently quantum mechanical phenomenon under certain circumstances reveals itself on the macroscopic level. One such circumstance is the case of a closed superconducting ring, where one finds that the magnetic flux passing through the hole in the ring is quantized[10] in units of the magnetic flux quantum. When this effect is combined with Josephson tunneling by the insertion of two junctions into the ring, the net result is a DC SQUID[11] as shown in Figure 3.2. The SQUID is essentially a flux-to-voltage transducer with a transfer function propor-tional to R/L, where R is the shunt resistance of the junction and L is the inductance of the SQUID loop. This can be realized in the following way:
Assume that the two junctions have identical critical currents I_0 and that the applied flux ϕ is zero. The I-V characteristic for the SQUID is then as shown in Figure 3.3 (left, the curve marked $\phi=n\phi_0$) with a critical current of $2I_0$. If we now apply an external flux ϕ, the SQUID will respond with a circulating current $J=\phi/L$, which will oppose the external flux so as to keep the flux ϕ_s through the SQUID loop quantized. As ϕ is increased to $\phi_0/2$ a point is reached, where it becomes energetically favorable for the SQUID to allow ϕ_s to increase from 0 to 1 flux quantum by reversing the direction of the circulating current. At this point the circulating current is $\phi_0/2L$. With an externally applied bias current I_B distributed evenly between the two arms of the SQUID loop, the current in the two junctions is then $I_B/2-\phi_0/2L$ and $I_B/2+\phi_0/2L$, respectively. When the larger of these currents reaches I_0, the SQUID goes into the voltage state, i.e. the maximum bias current in the zero-voltage state is $I_B=2(I_0-\phi_0/2L)$. This I-V characteristic is shown in Figure 3.3 (left, the curve marked $\phi=(n+1/2)\phi_0$) for the case $\phi_0=2LI_0$. As ϕ is increased

beyond $\phi_0/2$, the circulating current J will decrease in magnitude until it reaches zero at $\phi=\phi_0$ at which point the critical current of the SQUID is restored to $2I_0$. Further increases in ϕ will merely cause the SQUID to repeat this behavior.

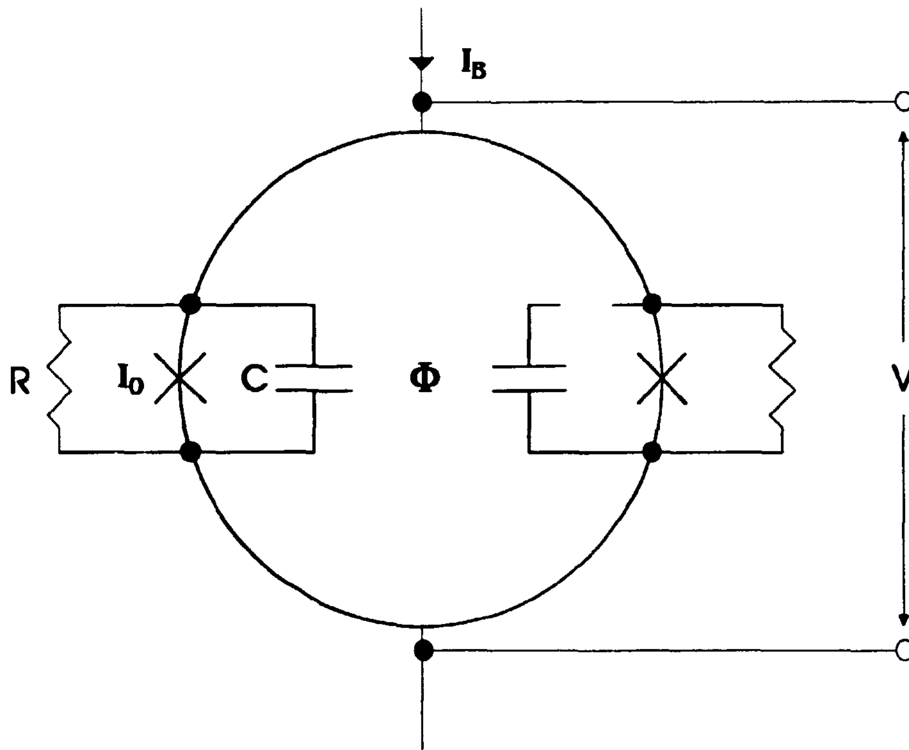

Figure 3.2 The equivalent diagram of a DC SQUID according to the RSJ model.

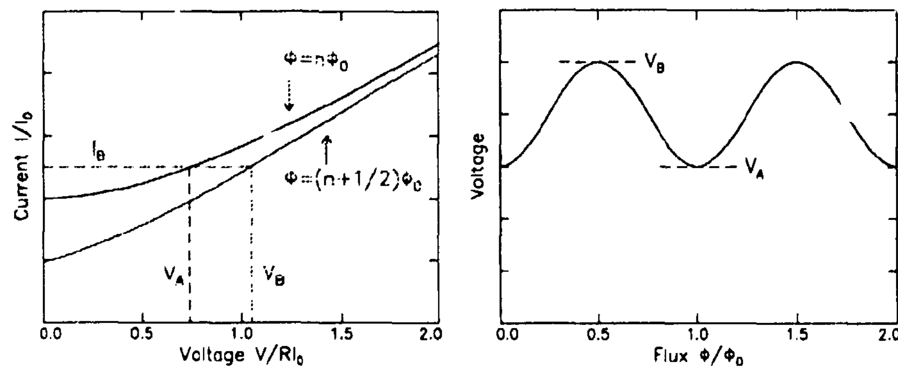

Figure 3.3 Left: I-V characteristic for the SQUID in the two cases $\phi=n\phi_0$ and $n=(n+1/2)\phi_0$. Right: V-ϕ curve showing how the voltage oscillates periodically in ϕ for a fixed bias current.

It is now clear that if the bias current is held constant at a value $I_B > 2I_0$, the SQUID will be in the voltage state at all times, and the voltage will oscillate between the two extrema V_A and V_B as a function of the applied flux ϕ. This behavior is shown in the V-ϕ characteristic in Figure 3.3 (right). The peak-to-peak value of the voltage depends on the modulation depth $\Delta I_c/2I_0$, which is a function of the screening parameter $\beta = 2LI_0/\phi_0$, and on the dynamical resistance R_d at the bias point. To a first approximation the transfer function $\partial V/\partial\phi$ can be found by realizing that a circulating current J leads to a reduction of the critical current by 2J and this current has to flow through the resistance $R_S = R/2$. Since an external flux $\phi_0/2$ leads to a circulating current $J = \phi_0/2L$ we find:

$$\frac{\partial V}{\partial \Phi} - \frac{\Delta V}{\Delta \Phi} = \frac{R_S \Delta I_C}{\Delta \Phi} = \frac{\frac{R}{2}\frac{\Phi_0}{L}}{\frac{\Phi_0}{2}} = \frac{R}{L}$$

A more accurate estimate of the transfer function is obtained if the shunt resistance R is replaced by R_d. This expression suggests that a large R and a small L is desirable for optimum performance of the SQUID. However, there are several other factors to consider in the design of a SQUID, and the discussion of how to optimize the overall performance will be deferred until after the discussion of noise.

3.1.3 Noise properties

The issue of noise is of fundamental importance in the design of the SQUID, since this is the limiting factor for the sensitivity to magnetic flux changes. The noise is measured in terms of the power spectrum $S_\phi(f)$ of the equivalent flux noise. In practice this is done by measuring the power spectrum of the voltage noise $S_v(f)$ for a given bias current. $S_v(f)$ and $S_\phi(f)$ are related by:

$$S_\Phi(f) = S_v(f) \left(\frac{\partial V}{\partial \Phi}\right)^{-2} \qquad (7)$$

This relation demonstrates the importance of maximizing $\partial V/\partial\phi$. As we saw in the previous section this can be done by minimizing L. However, since L is proportional to the linear dimensions of the SQUID loop, this minimization leads to a very small effective area and thus difficulty in coupling flux into the SQUID. It is therefore customary to use the so-called noise energy, defined as $\varepsilon(f) = S_\phi(f)/2L$, as a figure of merit, since this quantity explicitly takes the value of L into account.

The are several sources of noise in SQUIDs, displaying two different kinds of power spectra. The first of these power spectra is generated by the thermal noise, or Nyquist noise, and it is well understood. It originates in the shunt resistors and gives rise to a noise voltage with spectral density $S_v(f) = 4k_BT(R/2)$. With $\partial V/\partial\phi = R/L$ (from the simple approximation from the previous section), the noise energy due to the thermal noise is found to be k_BTL/R. However, because of the non-linearity of the Josephson junction, if a measurement is performed at frequency f_m, one will get a contribution not only from f_m itself,

but also from frequencies $nf_j \pm f_m$ (n integer) mixed down to f_m from the Josepson frequency f_j. For $f_m << f_j$ (as is the case for SQUIDs) all these mixed down contributions except those for n=1 are negligible. The net result is that one measures a value of the thermal noise somewhat higher than predicted by the Nyquist formula.

Another effect of the thermal noise is a rounding of the I-V characteristic at low voltages[12]. This can be understood if the noise is modeled as a noise current source $I_N(t)$ in parallel with the shunt resistance R. This causes fluctuations in the total current $I+I_N(t)$ passing through the junction and thus the value of the critical current I_0 will appear to fluctuate, since the junction switches when I exceeds $I_0 - I_N(t)$. The noise rounding is measured in terms of the noise parameter $\Gamma = 2\pi k_B T/\phi_0 I_0$, where $\phi_0 I_0/2\pi$ is the coupling energy of the junction. Computer simulations[13] indicate that Γ should be less than 0.2 in order for quantum interference effects to be observable.

Tesche and Clarke[14] have investigated the thermal noise by doing computer simulations based on a model of the SQUID essentially as Figure 3.2 with the addition of two voltage noise sources in series with the shunt resistors. They computed the transfer function, the spectral density of the voltage noise and the spectral density of the flux noise as a function of the bias current I_B and with the applied flux, the SQUID loop inductance, the temperature and the critical current as parameters. Their main results can be summed up as follows. The transfer function peaks sharply for $I_B \approx 1.5 \times (2I_0)$ as a function of all the parameters, which is understandable, since this is the region where the dynamical resistance is largest. When the bias current is held constant and the temperature is varied, they find that the increased noise rounding at high temperatures leads to a decreased transfer function. For the spectral density of the voltage noise they find, that this quantity also peaks sharply for $I_B \approx 1.5 \times (2I_0)$. However, what really matters is the spectral density of the flux noise and this quantity is found to go through a minimum for $I_B \approx 1.5 \times (2I_0)$. This can be understood on the basis of equation (7). Even though the voltage noise peaks, its effect is offset by the peak in the transfer function, and the net result is a dip in the flux noise. As a final important result from their simulation, they find that the flux noise as a function of the parameter $\beta = 2LI_0/\phi_0$ goes through a minimum at $\beta \approx 1$. Under this constraint they calculate a noise energy of $9k_B TL/R$ from the thermal noise, almost a factor of 10 higher than the estimate based on the Nyquist formula.

A very simple procedure for the optimization of the SQUID with respect to thermal noise at a given temperature has been established, based on the results of these computer simulations. First, one chooses a geometry for the SQUID. This will determine the value of L. The critical current of the junctions can be calculated from the requirement $\beta = 1$. With a given capacitance for the chosen type of junction, the shunt resistance is calculated based on the requirement that the junctions remain non-hysteretic, i.e. $\beta_c = 2\pi I_0 R^2 C/\phi_0 \leq 1$. Finally, the SQUID is operated with a bias current slightly larger than the critical current. It is interesting to note that since the noise energy ε_w due to thermal noise is proportional to $k_B TL/R$ and since the flux noise goes through a minimum for $\beta = 1$, i.e. when $2LI_0 = \phi_0$, the expression for ε_w can be written as $\varepsilon_w \propto k_B T\phi_0/RI_0$.

This relation demonstrates the importance of striving for a large RI_0 product as a means of lowering the noise energy, still under the constraint $\beta_c \leq 1$.

We now turn to the noise displaying the second kind of power spectra, the flicker noise or 1/f noise. This type of noise has been observed in numerous physical systems, but so far the origin of the noise remains elusive in the majority of the cases. The SQUID is one case where the 1/f noise can be partially explained.
There are at least two sources of 1/f noise in SQUIDs. The first arises from motion of flux lines trapped in the SQUID body itself[15]. There is little to be said about it, other than that the level of the noise seems to depend strongly on the microstructure of the thin films. This correlation was first observed in the low T_c materials, but has been found to be even more pronounced in the high T_c materials. It is not known why the power spectrum of the flux line motion scales as 1/f with frequency, and there is nothing one can do to reduce the noise level, other than to improve the quality of the film.
The other source of 1/f noise can be identified as 1/f fluctuations in the critical current and the mechanism for this is well understood[16]. If an electron is trapped on a defect in the barrier, the local value of the barrier height and thus the critical current will change. When the electron is subsequently released, the critical current will be restored to its original value. Assuming that the mean time between trapping events is τ, the spectral density of the process will take the form of a Lorentzian $S(f) \propto \tau / (1+(2\pi f\tau)^2)$. If it is further assumed that the process is thermally activated, i.e. that τ has a temperature dependence given by $\tau = \tau_0 \exp(E/k_BT)$, where τ_0 is a constant and E is the barrier height, and that the junctions contain several defects, each with its own characteristic time τ_0 and barrier height E, then the overall power spectrum, obtained by assuming that all the traps are statistically independent, can be shown to have the form[17] $S(f) \propto k_BT/f$.
The effect of the critical current fluctuations on the voltage noise can be analyzed as follows. Assume that the critical currents of the two junctions are $I_0+I_{N1}(t)$ and $I_0+I_{N2}(t)$, respectively, where $I_{N1}(t)$ and $I_{N2}(t)$ are uncorrelated. By defining two noise currents $I_{N+}(t) = (I_{N1}(t)+I_{N2}(t))/2$ and $I_{N-}(t) = (I_{N1}(t)-I_{N2}(t))/2$ the junction critical currents can be written as $I_0+I_{N+}(t)+I_{N-}(t)$ and $I_0+I_{N+}(t)-I_{N-}(t)$, i.e. the noise currents can be decomposed into an in-phase component $I_{N+}(t)$, which leads directly to a reduction of the critical current, and an out-of-phase component $I_{N-}(t)$ leading to a circulating current, which behaves like a flux noise $\phi_N(t) = LI_{N-}(t)$. The resulting voltage noise across the SQUID is then:

$$V_N(t) = \frac{\partial V}{\partial I_0}\Delta I_0 + \frac{\partial V}{\partial \Phi}\Delta\Phi = \frac{\partial V}{\partial I_0} I_{N+}(t) + \frac{\partial V}{\partial \Phi} LI_{N-}(t)$$

The spectral density of the voltage noise thus becomes proportional to:

$$S_V(f) \approx \left(\left(\frac{\partial V}{\partial I_0}\right)^2 + \left(\frac{\partial V}{\partial \Phi}\right)^2 L^2\right) S_{I_0}(f)$$

where $S_{I0}(f)$ is the spectral density of the current noise.

The issue of how to reduce the noise associated with the critical current fluctuations is closely related to the modulation scheme employed in the operation of the SQUID. In Figure 3.4 is shown a block diagram illustrating the principle of the traditional operation mode, based on a flux-locked feedback loop. In this scheme, a modulating flux with peak-to-peak value $\phi_0/2$ and frequency f_0 (typically 100 kHz) is applied via a modulation coil placed in the close vicinity of the SQUID. In the absence of any externally applied flux, the voltage across the SQUID will be at a minimum (cf. Figure 3.3, right). The modulating flux, which oscillates between $-\phi_0/4$ and $\phi_0/4$, will then give rise to an ac voltage with frequency $2f_0$. If this voltage is lock-in detected with the oscillator driving the modulation coil, the output will be zero. However, if the externally applied flux is changed to any value other than n × $\phi_0/2$ (n integer), the ac voltage caused by the modulating flux will have a component with frequency f_0 and thus the output from the lock-in detector will be finite. This output is fed back to the modulation coil through a resistor R so as to cancel out the external flux and restore the flux in the SQUID loop to zero. The dc voltage across R is then a measure of the externally applied flux.

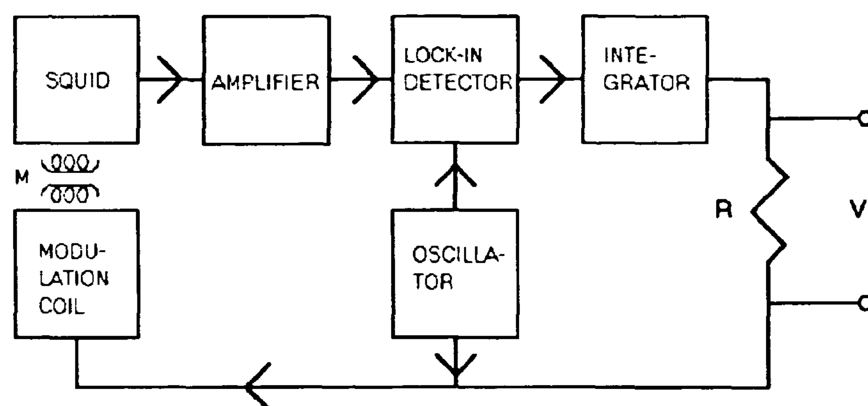

Figure 3.4 Block diagram showing the principle behind the flux-locked loop. A modulating flux is coupled to the SQUID via the mutual inductance M.

It should now be clear that the voltage noise associated with the in-phase component of the critical current fluctuations is eliminated by this flux-locked loop scheme for frequencies below the modulation frequency, since all the in-phase component does is to shift the V-ϕ curve along the V-axis. However, this modulation scheme does not affect the out-of-phase component of the critical current fluctuations.

It is possible to extend the modulation scheme described above in such a way that also the noise voltage associated with the out-of-phase component of the critical current fluctuations is eliminated. In this so-called double modulation scheme[15], the bias is reversed with frequency f_1 and each bias current reversal is accompanied by a change in the applied flux of $\phi_0/2$. In this way it is

possible to render the SQUID output insensitive to both components of the critical current fluctuations, while at the same time keeping it sensitive to changes in the externally applied flux. The noise associated with the critical current fluctuations can thus be completely eliminated for frequencies below f_1.

We conclude our discussion of noise by noting that the fact that high T_c junctions do not have a well defined shunt resistance (in contrast to low T_c junctions) opens up the possibility of 1/f noise due to resistance fluctuations[18]. However, recent experimental results indicate, that in bi-epitaxial junctions (to be described later) this type of fluctuations are negligible compared to critical current fluctuations[19].

3.2 Experimental techniques

In this section we will briefly describe the experimental techniques we have employed in the fabrication processes of SQUIDs and magnetometers. First we will describe how to create the desired patterns in the thin films by shadow masking or by photolithographic techniques in combination with chemical etching or ion milling. Next we will describe how we have characterized the samples electrically (by resistance-versus-temperature measurements, I-V and V-ϕ characteristics) and structurally (by X-ray diffraction measurements). The deposition of the thin films by laser ablation has already been described in Chapter 1.

3.2.1 Patterning of thin films

Even the simplest devices require some form of patterning of the superconducting layer(s) and thus anyone wishing to engage in any sort of device work has to deal with this issue. Fortunately, much experience in this field has already been accumulated in the semiconductor industry. This knowledge is readily available in places like the Microfabrication Laboratory at UC Berkeley, where a substantial part of the device fabrication was carried out.

The simplest way to achieve a patterned film is to use a shadow mask in front of the substrate during the deposition. A shadow mask is a sheet of stainless steel or some other material, which does not react with the film or substrate material, even under the relatively high temperatures of the deposition process. The desired pattern is cut out of the mask and thus it will prevent deposition of material in places outside the pattern. The main advantage of this technique is that the deposition and patterning is carried out simultaneously and it is therefore very fast compared to photolithography. However, there are several drawbacks. It is difficult to obtain line widths below a few hundred microns and it is even more difficult to align two layers, even on this relatively crude scale of a few hundred microns. Also, because the mechanical contact between the mask and the substrate is not perfect, the deposited material diffuses in under the mask and leaves poorly defined edges.

All of these problems can be alleviated by using photolithography to pattern the layers. The idea behind this method is to form a mask or stencil of photoresist, which will then protect those parts of the film, that make up the desired pattern, during the actual etching of the film. Initially, the film is deposited all over the substrate. After removal from the deposition chamber, it is covered with photoresist everywhere, followed by either a soft bake at 70 °C - 90 °C or a hard bake at 120 °C. The sample is exposed to UV light through an emulsion mask, which will leave the desired pattern unexposed in the resist (in the case of a positive resist). After exposure the resist is developed, i.e. the exposed parts of the resist is removed. The sample is then ready for the actual pattering of the film, either by chemical etching or by ion milling.

In all our experiments we have used Microposit 1400-31 photoresist applied by means of a Headway Research resist spinner at 6000 rpm for 30 seconds. The sample and mask was aligned in a Canon FPA 141 fine pattern projection aligner. The photoresist was developed in a mixture of Microposit developer concentrate and water in a 1:1 ratio.

With the photoresist stencil in place, the sample is ready for the actual patterning of the film. One way to do this is by ion milling. With this technique, the material is sputtered away under bombardment with positive ions of a suitable gas, typically argon. The ions are generated in an ion gun. We have used a gun of the Kaufmann type with two filaments. A heated cathode emits electrons, which ionize the argon gas. The ions are extracted from the gun by an acceleration voltage. Usually the ion beam is focused to some extent by the addition of one or more grids with suitable control voltages. Electrons can be added to the ion beam by the second heated filament, the neutralizer. As the name implies, the purpose of this filament is to neutralize the ion beam, thereby extending the ion milling technique to non-conducting materials, which would otherwise become positively charged and repel the ions.

One of the problems with the Kaufmann type of ion guns is that the filaments produce substantial amounts of heat. This radiation heat, in combination with the mechanical heat generated by the argon ion bombardment, can lead to severe degradation of the sample. This is especially true for YBCO, since this material easily loses oxygen when it is heated in low oxygen partial pressures. Recently, a new type of filamentless ion gun has been introduced, but we have not had access to such an ion gun. Instead we have used an Ion Tech 2.5 cm Kaufmann source in combination with a water cooled sample holder.

Another way to pattern the film is to use a chemical wet etch. Most of the materials we have used can be etched by a suitable choice of acid. YBCO and MgO have reasonable etch rates in a 0.05% HNO_3 solution, while $SrTiO_3$ is removed by a 7% HF solution. Only CeO_2 is not easily removable by an acid. The problem of sample heating does not exist in chemical etching, but instead the problem of undercutting arises. The etching process does not stop when the material outside the resist stencil has been removed, but continues to etch away the material under the stencil. As a result, the pattern in the film becomes narrower than intended, typically by a couple of microns on each side.

Linewidths less than about 5 μm can therefore not be patterned reliably with an acid etch. For most of the work we have done, however, the method works very well.
The last step in the patterning process, regardless of which of the methods described has been used, is the removal of the photoresist stencil. When the sample has been acid etched this can be done in ethanol using an ultrasonic bath. When the sample has been ion milled, however, it becomes significantly more difficult to remove the resist, and it is necessary to use acetone instead of ethanol. Most likely, the milling process itself and/or the resulting heating of the sample, induces changes in the resist, which makes it harder to remove. As a matter of fact, we have used the degree of difficulty encountered in the resist removal as an indicator of possible damage inflicted on the sample in the milling process.

3.2.2 Electrical characterization

The samples have been characterized electrically in the form of resistance-versus-temperature measurements, and by I-V and V-ϕ characteristics. During the optimization of the deposition parameters, we have made extensive use of structural characterization in the form of X-ray diffraction.
The resistance was measured as a function of temperature by a four point measurement in a liquid helium dewar. The wires were attached to the sample by pressed indium contacts. A fixed current was passed through the sample, which was initially lowered and then slowly raised to allow the temperature to increase. The voltage across the sample was measured with a HP 3478A multimeter and the temperature was measured with a platinum resistor connected to a Lakeshore Cryotronics DRC 82C temperature controller. Both of these instruments were interfaced to an IBM PC to facilitate data recording and manipulation.
The I-V characteristics were recorded with the system shown in Figure 3.5. The central component in the system is the I-V box. A function generator in series with a variable resistor (100 Ω-5kΩ) is used to generate an input current I_{in} to the box, which in turn generates an output current I_{out} to the sample and also a control voltage (marked V_{mon}). This voltage is sent to the Y-input on the plotter. The ratio between V_{mon} and I_{out} is either 100 Ω or 10 kΩ (selectable by a switch). The voltage across the sample is amplified in the I-V box by a factor of 10^2, 10^4 or 10^5 (also selectable by a switch), before it is sent to the X-input on the plotter. An oscilloscope is connected to the system in parallel with the plotter to allow photographic recording of the I-V characteristic. The temperature is varied by raising or lowering the temperature in a shielded liquid helium dewar (μ-metal shield).
This system can easily be reconfigured to record the V-ϕ characteristic. In that case the output current from the I-V box is fed to the field coil. This coil is permanently installed in the probe and provides a variable magnetic field. The bias current to the SQUID is provided by a battery in series with a variable resistor. In this way the bias current can easily be adjusted to its optimum value for a given temperature.

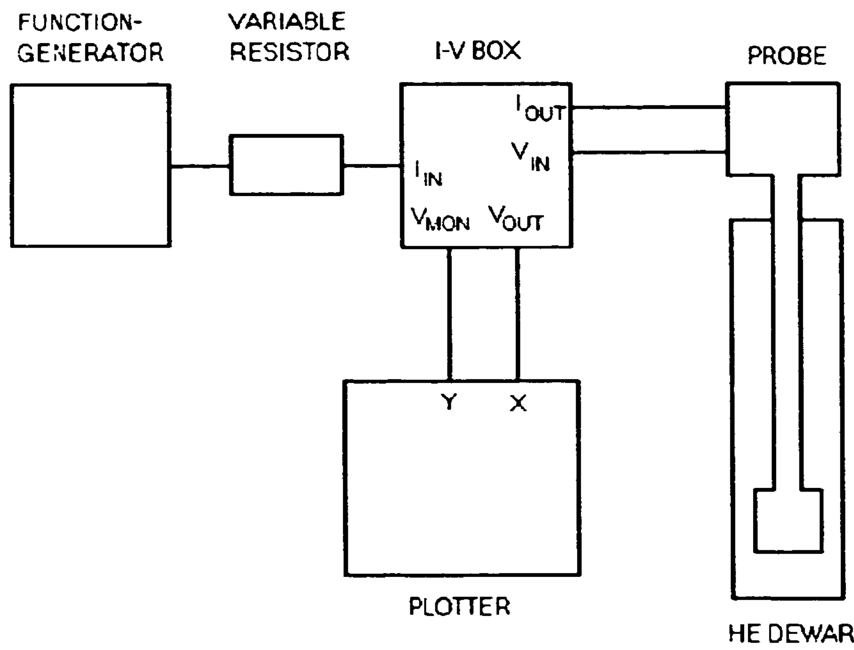

Figure 3.5 The I-V and V-ϕ characteristics were recorded with the system shown here. In this figure the system is configured for I-V measurements.

3.2.3 Structural characterization

Samples with YBCO in combination with various dielectric layers were characterized by X-ray diffraction in the form of θ-2θ scans and φ-scans as described in Chapter 2. The experimental setup consisted of an Enraf-Nonius Scintag model DMC-105 four-circle spectrometer and was physically located in the Department of Geology at UC Berkeley. The X-rays (Cu K_α radiation) were produced by an X-ray tube (operated at 40 kV and 10 mA) in combination with a graphite monochromator. The resolution of the spectrometer reflected its primary use as an instrument intended to find the general trends in the orientation distribution rather than the precise location of reflections in a highly textured sample. The resolution, as determined by doing scans on an MgO substrate, was 0.80° FWHM in the θ-2θ scan (at θ=42.94°) and 1.28° in the φ-scan. The spectrometer was interfaced to a computer controlling the angles ω, 2θ, χ and φ via step-motors, and which was also used to store the data. Table 3.1 below shows the 2θ values and relative intensities for the most important reflections for each of the materials we have used in the fabrication process. The 2θ angles are given for Cu K_α radiation (λ=1.542 Å). All four materials are cubic with lattice parameter a=4.213 Å, a=5.139 Å, a=3.905 Å and a=5.411 Å, respectively, for MgO, YSZ, $SrTiO_3$ and CeO_2 (data taken from the Powder Diffraction Files of the Joint Committee on Powder Diffraction Standards). YSZ is an acronym for Yttrium Stabilized Zirconia. The material consists of ZrO_2 with about 9.5 % Y_2O_3 added to it. The Y atoms are substituted for the Zr atoms in the crystal structure, and stabilizes the cubic high temperature

phase against transformation to the monoclinic phase[20] found in pure ZrO_2 at room temperature, and which has poor mechanical properties.

MgO			YSZ			$SrTiO_3$			CeO_2		
hkl	2θ	I/I_0	hkl	2θ	I/I_0	hkl	2θ	I/I_0	hkl	2θ	I/I_0
111	36.96	10	111	30.12	100	100	22.77	12	111	28.57	100
200	42.94	100	200	34.92	25	110	32.43	100	200	33.11	30
220	62.34	52	220	50.22	55	111	39.99	30	220	47.52	52
222	78.68	12	222	62.63	6	200	46.52	50	222	59.14	8
400	94.11	5	400	73.76	5	220	67.90	25	400	69.48	8

Table 3.1 2θ angle and relative intensity for the dielectric materials used as substrate materials and seed and buffer layers. The 2θ angles are based on Cu K_α radiation.

3.3 SQUIDs fabricated by the bi-epitaxial process

The first reports[21] of SQUIDs made from YBCO appeared already in the spring of 1987, only a few months after the material had been discovered. These early devices were made from post annealed films, a technique which is now known to result in polycrystaline films. Because of the weak-link nature of high-angle grain boundaries, SQUIDs can be made simply by patterning a loop intersected in two places by such a grain boundary.

Ideally, one would like to be able to fabricate Josephson junctions by a process whereby one has control over the junction parameters R, C and I_0, since certain relationships between these parameters are desired for proper device operation. The obvious way to achieve this control is to deposit and pattern each electrode and the barrier individually. However, since the high quality films grow with the c-axis perpendicular to the substrate, and since the coherence length along the c-axis[22,23] is less than 10 Å, the fabrication of such a sandwich junction would require the ability to deposit a homogeneous, defect-free barrier with a thickness of only a few Å. This is not possible with the currently available technology.

One of the alternative ways to fabricate junctions is based on the fact that YBCO displays strong anisotropy in many of its materials parameters. In particular, it is found that the coherence length is significantly longer in the a-b plane than along the c-axis. Typical values of a few tens of Å have been reported[22,23] in the literature. This fact is exploited in the edge junctions. This type of junction is fabricated by depositing the barrier and counter electrode over a patterned edge in the base electrode. In this way tunneling of Cooper pairs parallel to the a-b planes is achieved. Several groups have reported on junctions made in this way, using a variety of materials such as BaF_2[24],

$SrTiO_3$[25], PBCO[26,27] and even a non-superconducting phase of YBCO[28] as barriers. The best of these junctions display Shapiro steps under microwave irradiation (Shapiro steps are steps in the I-V characteristic that occur at voltages $V = n \times (hf_s / 2e)$, where f_s is the frequency of the microwave signal and n is an integer. At f_s = 3 GHz the spacing between the steps is 6.2 µV). Also, they exhibit an I_c versus B dependence closely approximating the expected Fraunhofer pattern.

The IBM group has studied the properties of grain boundaries in YBCO extensively[29,30] by depositing YBCO films on bi-crystals. The bi-crystals are made by cutting two single crystals of $SrTiO_3$ under a certain angle and fusing them together again. The YBCO deposited on top will then be forced to form grain boundaries with the same angle. They find that all grain boundaries in YBCO (except boundaries smaller than a few degrees) act like weak links. In continuation of this work they have fabricated junctions and SQUIDs[31,32] and achieved the lowest white noise level at 77 K reported to date (3×10^{-31} J/Hz). Recently, there have been reports[33,34] of SQUIDs fabricated on YSZ bi-crystals. While it is evident that the bi-crystal technique is feasible and has produced some of the best SQUIDs so far, it is also true that the fact that the junctions have to be placed along the boundary between the two single crystals is a severe limitation if one wants to fabricate more complicated circuits.

The bi-epitaxial process offers the opportunity to create a high-angle grain boundary at will anywhere in an otherwise epitaxial YBCO thin film using a simple single crystal substrate as the starting point. The idea of this process was triggered by the observation that YBCO displays two preferred in-plane orientations on a YSZ substrate, depending on the temperature of the substrate during deposition[35]. If the two in-plane orientations can be produced by growing the film on a substrate, which is partially covered with a suitable seed layer, then it becomes possible to create high-angle grain boundaries in YBCO films using standard photo-lithographic techniques. This was first demonstrated on a sapphire substrate using MgO as the seed layer[36]. Later, junctions with improved properties were fabricated using $SrTiO_3$, MgO and CeO_2 as base layer, seed layer and buffer layer[37]. Because $SrTiO_3$ grows epitaxially on most of the commonly used substrates, this set of materials greatly expands the possibilities for junction fabrication on other more suitable substrates than sapphire, which differs from YBCO in the magnitude of the thermal expansion coefficient. In the remainder of this section we will describe our work on the fabrication of bi-epitaxial junctions and SQUIDs on MgO and YSZ substrates.

During the development of a process it is necessary to deal with such questions as: What are the optimum deposition parameters for each layer? How does the patterning of the layers affect the quality of the subsequent layers? and how does the edge created by the patterning of the seed layer affect the junction quality?

3.3.1 SQUIDs on MgO substrates

From the experiments described in Chapter 2 we know that if the deposition parameters are optimized, then both $SrTiO_3$ and YBCO align with the MgO

substrate in the a-b plane. Given the established epitaxial relations between $SrTiO_3$, MgO and CeO_2 (CeO_2 [110] parallel to $SrTiO_3$ [100] and CeO_2 [100] parallel to MgO [100], from Ref. 37) and between YBCO and CeO_2 (YBCO [110] parallel to CeO_2 [100][38]) it is possible to obtain a 45° grain boundary in the YBCO layer in a number of ways.

The simplest way involves only an MgO substrate with a CeO_2 seed layer followed by the YBCO layer. However, high quality MgO substrates are required for this scheme to work and furthermore, it is essential that the patterning of the CeO_2 layer by ion milling does not inflict damage on the MgO substrate surface. We tested this by breaking an MgO substrate in two halves. One half was ion milled under typical conditions (beam voltage 500 V, beam current density 0.8 mA/cm^2) before the YBCO was deposited, whereas the YBCO was deposited directly on the other half without the ion milling step. The result of a partial X-ray φ-scan on these two samples is shown in Figure 3.6. Since the scan spans a range less than 90° we expect to see only one peak if the film grows fully oriented in the a-b plane.

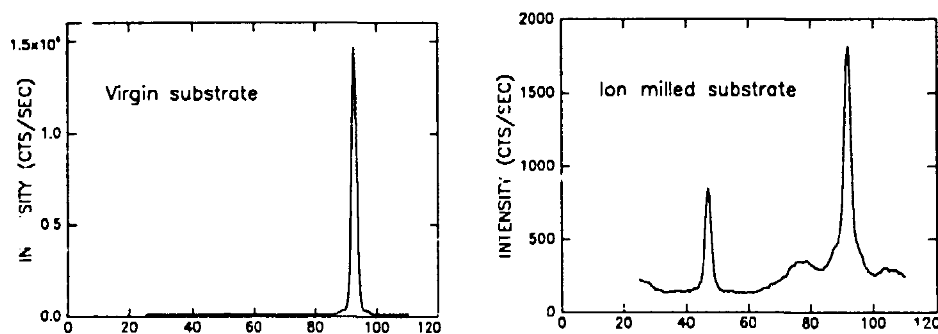

Figure 3.6 φ-scans on YBCO (103) reflection for films deposited on a virgin MgO substrate (left) and an ion milled MgO substrate (right). Obviously the ion milling step damages the substrate surface.

The scan on the left is from the sample which was not ion milled and is essentially clean, meaning that there is no intensity other than the peak around φ=90° (any deviations of the peaks in the φ-scans from 90° or multiples thereof is due to the fact that the alignment of the crystallographic directions with the φ-scale during the sample mounting is only approximate). The scan on the right is from the ion milled sample and has a distribution of intensities, with a significant part of the film rotated 45°. Clearly, a substrate like this can not be relied upon to impose a well defined in-plane orientation in a YBCO film.

Another combination of materials which would result in high-angle grain boundaries consists of an MgO substrate completely covered with a CeO_2 buffer layer, followed by a $SrTiO_3$ seed layer and the YBCO layer. This combination is only slightly more complicated than the previous and it avoids the exposure of the MgO substrate to the patterning process. Unfortunately, $SrTiO_3$ on CeO_2 grows with the (110) direction per-pendicular to the substrate and thus the YBCO film on top will not be c-axis oriented.

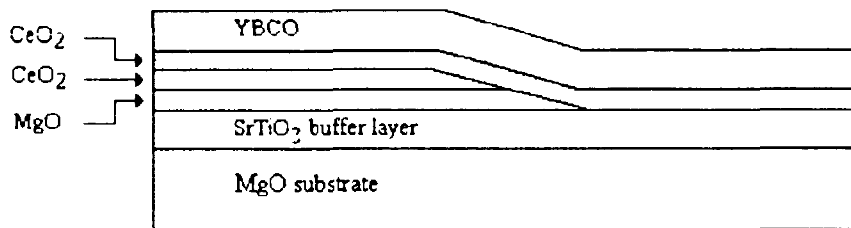

Figure 3.7 Sequence of epitaxial layers used to create the high-angle grain boundary.

We are thus led to the combination of layers shown in Figure 3.7. In this case $SrTiO_3$ is used as buffer layer for the MgO substrate, followed by MgO and CeO_2 films to create the rotation in the YBCO layer. The CeO_2 layer is always deposited before the patterning of the seed layers, although from the point of view of obtaining the in-plane rotation, it is possible to deposit only the MgO layer, pattern it, and then deposit CeO_2 and YBCO. We have tried this approach, but without success, most likely because the MgO layer is damaged by the exposure to the photoresist. After the patterning of the seed layers one can choose to deposit a second CeO_2 layer (shown shaded in the figure) before the YBCO layer, or one can put down the YBCO layer immediately, since both procedures will result in the creation of a 45° grain boundary. Both schemes work in practice, although we find that the inclusion of a second CeO_2 layer gives more reliable results.

The successful growth of 5 epitaxial layers requires careful tuning and control of the deposition parameters. Several factors, such as substrate temperature T_s, oxygen ambient pressure P_{O2}, laser fluence and target to substrate distance, influence the growth of a laser ablated film and thus the deposition of 5 layers opens up a parameter space of more than 20 dimensions when also the patterning step is included. However, the temperature T_s and the oxygen pressure P_{O2} are more crucial than the other parameters and this fact greatly simplifies the optimization process.
The Berkeley group has previously grown $SrTiO_3$ films for insulating crossovers[39], but at a relatively low temperature in order to minimize the interdiffusion between the insulator and the base superconductor. In Figure 3.8 we show θ-2θ scans for two $SrTiO_3$ films grown on MgO substrates. Each film was grown at 150 mTorr oxygen ambient to a thickness of about 3000 Å. The scan on the left is from a film grown at a substrate temperature T_s=760 °C, while the scan on the right is from a film deposited at 710 °C. Clearly, the film deposited at low temperature grows partly (110) oriented (the intensity of the (110) peak is about 3.7 % relative to the (200) peak, indicating that 1.85 % of the film is (110) oriented), while the film grown at high temperature appears to be fully c-axis oriented within the experimental error. We have adopted T_s=760 °C and P_{O2}=150 mTorr as the standard conditions for the deposition of $SrTiO_3$ on MgO.

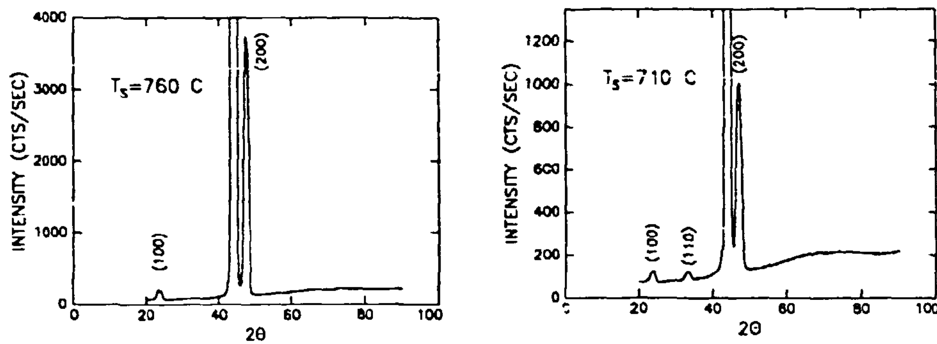

Figure 3.8 Left: $SrTiO_3$ film grown fully c-axis oriented at T_s=760 °C. Right: $SrTiO_3$ film grown at T_s=710 °C displays partly (110) oriented growth.

We have not conducted any systematic studies of how to deposit MgO films on $SrTiO_3$. It is known from the literature[40] that MgO films can be grown epitaxially on Si by laser ablation at very low oxygen pressures (a few μTorr) and at temperatures ranging from 400 °C to 600 °C. We have somewhat arbitrarily adopted the parameters T_s=600 °C and P_{O2}=2 mTorr for the MgO deposition. We have verified that these parameters lead to epitaxial growth of the MgO by X-ray characterization of multilayers incorporating an MgO layer (see later in this chapter).

Next we turn to the question of the deposition of CeO_2 on MgO. One way to examine this would be to grow a relatively thick CeO_2 film (~1000 Å or so) on MgO and then examine it directly by X-ray diffraction. However, for the purpose of making bi-epitaxial junctions we are more interested in thin CeO_2 films. They need only be thick enough to cover the MgO films completely and any excess thickness will merely increase the step height created during the patterning of the seed layer. Also, it might be that the optimum conditions for very thin films (~100 Å) differ from those of thicker films. We have therefore chosen to optimize the CeO_2 deposition by growing very thin films of CeO_2 followed by ~3000 Å of YBCO and then examined the YBCO film. This scheme requires of course that we know how to grow YBCO on CeO_2 . We have adopted the parameters used for YBCO on $SrTiO_3$ and, as we shall see, this approach has given good results.
Since the all important property to control is the in-plane epitaxy, we have evaluated the CeO_2 films by doing φ-scans on the YBCO (103) reflection. In Figure 3.9 we show φ-scans for four films, where the CeO_2 was grown in 100 mTorr oxygen ambient to a thickness of about 100 Å, followed by ~3000 Å YBCO at T_s=760 °C and 200 mTorr oxygen. The temperature during the CeO_2 deposition was 820 °C, 800 °C, 780 °C and 760 °C, respectively, in scans a), b), c) and d). Given the epitaxial relations between MgO, CeO_2 and YBCO mentioned earlier, we expect the peak from YBCO (103) to occur close to φ=45° + n×90° (n integer), since the sample was mounted such that the MgO (202) reflections occurred close to φ=n×90°. The two samples deposited at 820 °C and 800 °C have a substantial part of the film misaligned. The two films

deposited at 780 °C and 760 °C look much better; the film at 780 °C has a narrower and more intense peak than the film deposited at 760 °C. We have therefore fixed the deposition temperature of CeO_2 at 780 °C.

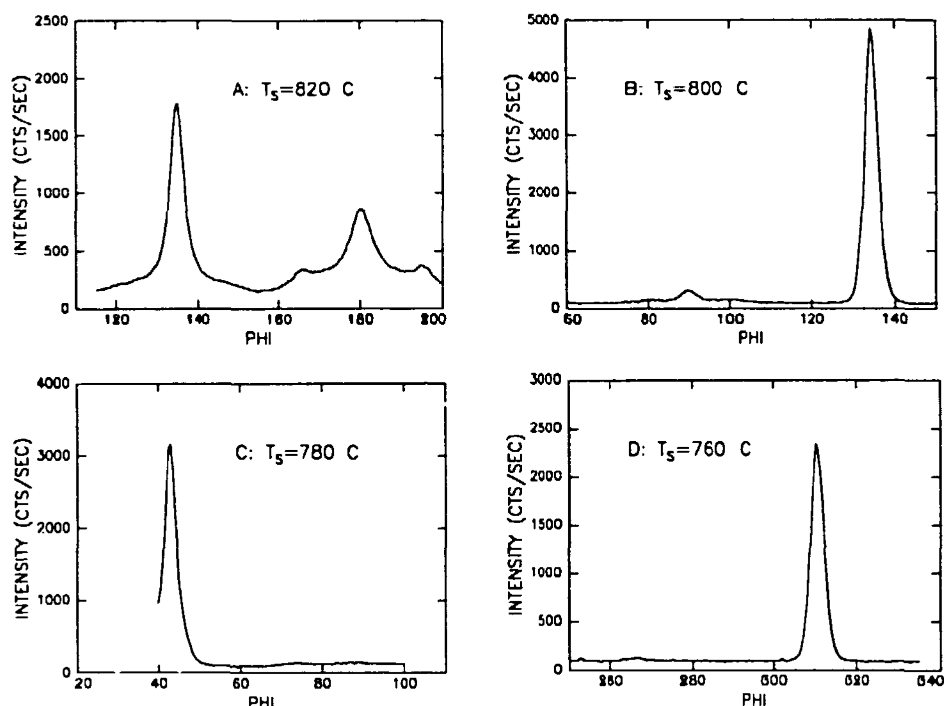

Figure 3.9 These φ-scans on the YBCO (103) reflection demonstrate how the in-plane epitaxy of YBCO on CeO_2 buffered MgO depends on the substrate temperature during deposition of CeO_2. We have chosen T_s=780°C as the optimum temperature.

It is interesting to note in Figure 3.9 a) that there appears to be two sidelobes displaced approximately 14.5° from the main misaligned peak at φ≈180° (or ≈30.5° from the aligned peak). We have noticed these sidelobes in several φ-scans of YBCO on CeO_2 buffered MgO, most notably in a sample where the CeO_2 was grown to a thickness of ~200 Å at 795 °C in 100 mTorr oxygen (data not shown). In that case the φ-scan on YBCO consisted only of the main peak at φ≈135° and the two sidelobes, whereas the main misaligned peak at φ≈90° was completely absent. This behavior can be explained in terms of a coincident site lattice model for CeO_2 on MgO (we are assuming that YBCO always grows with the [110] parallel to the CeO_2 [100], regardless of the relative orientation of MgO and CeO_2). The basic postulate of this theory is that if two interpenetrating lattices rotate with respect to each other, they will choose the rotation angle such that points in one lattice coincide with points in the other lattice. In practice, the lattice points do not coincide exactly. The deviation from exact coincidence is measured by means of a misfit parameter δ, which is the relative difference in length between the two lattice vectors defining the coincident site lattice. Specifically, for two c-axis oriented cubic

lattices with lattice parameters a_1 and a_2 the misfit between lattice points with in-plane Miller indices (h_1,k_1) and (h_2,k_2) is:

$$\delta = \frac{2\,(a_1\sqrt{h_1^2+k_1^2} - a_2\sqrt{h_2^2+k_2^2})}{a_1\sqrt{h_1^2+k_1^2} + a_2\sqrt{h_2^2+k_2^2})}$$

The main misaligned peaks at $\varphi \approx n \times 90°$ are then explained simply by rotating the CeO_2 45° on MgO. The sidelobes arise because parts of the CeO_2 film grows with its [610] direction parallel to the [650] direction of the MgO substrate, giving rise to a rotation of 30.34° away from the aligned direction with a misfit of only 0.03%. This configuration is illustrated in Figure 3.10, where it is easily seen that the three white circles represent nearly coincident lattice points. It would be useful if the deposition parameters could somehow be adjusted such that the whole CeO_2 film would be fully aligned in this particular direction, since this would allow the creation of grain boundaries with misorientation angles of about 30°. Such a grain boundary would presumably have better properties than the 45° grain boundary. We will return to this point later.

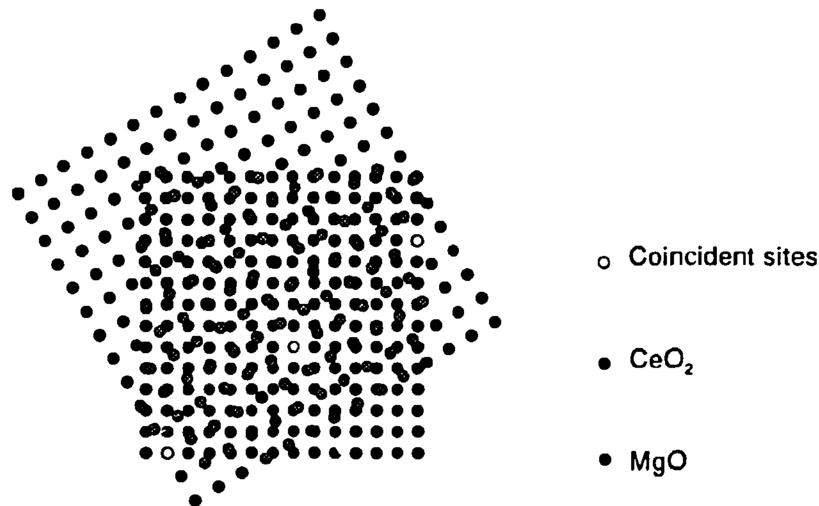

Figure 3.10 This figure shows the MgO and CeO_2 lattices rotated 30.34° with respect to each other. Lattice points along the [610] direction in CeO_2 coincide with points along the [650] direction in MgO with a misfit of only 0.03 %.

With the deposition temperature of CeO_2 fixed at 780 °C we continue our optimization by varying the oxygen pressure. In Figure 3.11 we show φ-scans for YBCO films deposited on top of 100 Å thick CeO_2 films. The CeO_2 was deposited in 150 mTorr and 200 mTorr oxygen, respectively, in the scans on the left and the right. Both these scans are essentially clean and they have much more intensity in the main peaks than the scans in Figure 3.9, deposited in 100 mTorr. It seems that the quality of the CeO_2 is strongly sensitive to the oxygen pressure during deposition. The scan on the left has a slightly narrower

peak and we have therefore adopted T_s=780°C and P_{O_2}=150 mTorr as standard conditions for the deposition of CeO_2 on MgO.
We have also tried to change the thickness of the CeO2 layer both to larger and smaller values, but we did not improve the resulting YBCO film compared to a CeO_2 thickness of 100 Å.

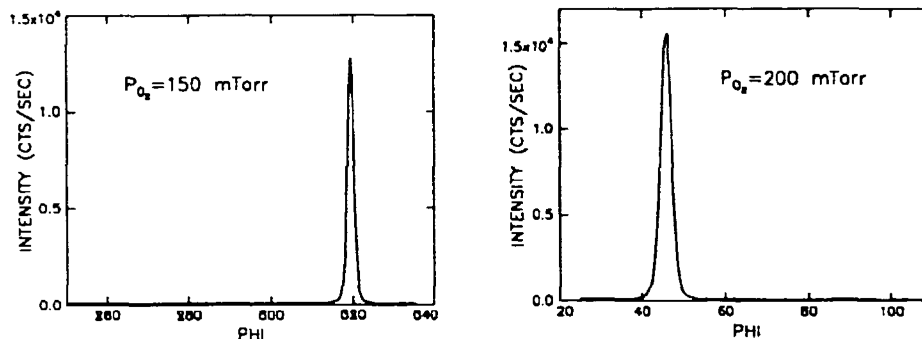

Figure 3.11 These two φ-scans on YBCO (103) demonstrate how the in-plane epitaxy of YBCO on CeO_2 buffered MgO depends on the oxygen pressure during deposition of CeO_2. We have chosen P_{O_2}=150 mTorr as the optimum pressure because it results in the smallest mosaic spread.

As mentioned earlier, we find that the conditions for YBCO deposition on $SrTiO_3$ (T_s=760°C, P_{O_2}=200 mTorr) also work well for YBCO deposition on CeO_2. We have therefore not made any attempts to optimize them further. Before proceeding to make actual SQUIDs, it is useful to check that the extra processing required to pattern the seed layers does not destroy the in-plane epitaxy of the subsequent layers. In Figure 3.12 we show two φ-scans for samples processed as an actual SQUID sample would be. In both cases we use the (102) reflection rather than the stronger (103) reflection, because the YBCO (103) reflection occurs at almost the same 2θ and χ angles as the $SrTiO_3$ (101) reflection, but shifted 45° in φ. Thus any intensity from misaligned YBCO would be buried in the $SrTiO_3$ (101) peak. The scan on the left is from a sample which has been treated as the SQUID would be on the left side of the grain boundary in Figure 3.7. $SrTiO_3$, MgO and CeO_2 is deposited, photoresist is spun, baked and removed, and the second CeO_2 and the YBCO layers are deposited. The scan on the right is from a sample where $SrTiO_3$ is deposited initially, the sample is then ion milled at 500 V, 0.8 mA/cm^2 for 1 minute, before the CeO_2 and YBCO layers are deposited. In both scans we see that the main peak appears broadened compared to the best scan in Figure 3.11, but there is no obvious signs of misaligned YBCO. Note that the main peaks differ by 45° as expected. We thus conclude, that it should be possible to obtain a high-angle grain boundary with the process described above. This process is summarized in the Table 3.2 below.

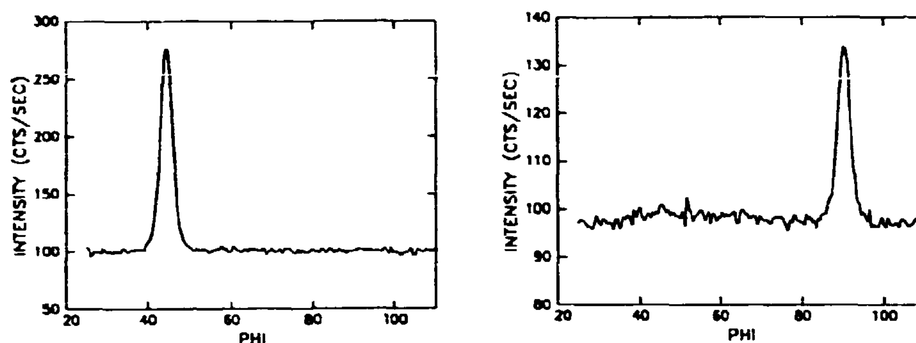

Figure 3.12 These two φ-scans on YBCO (102) are recorded from samples processed as an actual SQUID sample would be on either side of the grain boundary. Note that the two peaks are shifted 45° in φ as expected.

Material	Temp. (°C)	Pressure (mTorr)	Thickness (Å)	Patterning
$SrTiO_3$	760	150	800	None
MgO	600	2	100	Ion milled at 500 V, 0.8 mA/cm^2, 60° to the normal for 2½ minutes
CeO_2	780	150	100	
CeO_2	780	150	100	None
YBCO	760	200	3000	Acid etched in 0.05% HNO_3
Ag	20	1	1000	Shadow masked

Table 3.2 Summary of the fabrication process for bi-epitaxial SQUIDs on MgO substrates. The second, third and fourth columns give the substrate temperature in °C, oxygen ambient pressure in mTorr and thickness in Å, respectively.

Regarding the ion milling of the seed layers, it is intuitively clear that we should not mill longer than necessary to remove the CeO_2 and MgO layers. The sample can be mounted in the ion mill in two orientations, one with a 60° angle between the beam and the substrate normal and one with a 75° angle. The mill rates are about the same for all the dielectric films and have been measured to be ~200 Å/s and ~100 Å/s for the two angles, respectively, under the standard conditions 500 V beam voltage and 0.8 mA/cm^2 beam current density. With a total thickness of 200 Å for the CeO_2 and MgO layers, a milling time of 2½ minutes at 60° to the normal (corresponding to the removal of ~500 Å) appears a bit on the high side. However, we have noted that the mill rates can fluctuate as much as 25% under apparently identical conditions and we have therefore chosen to be on the safe side, since there is no way to tell whether all of the MgO has been removed, other than to complete the sample and test it. The thickness of the $SrTiO_3$ buffer layer is chosen such that we can be sure that we do not mill through it.

In some of the SQUID samples the seed layers have been patterned by ion milling at 75° to the normal for 4½ minutes, corresponding to the removal of ~450 Å. Presumably, this leaves a more shallow edge which should make it easier for the subsequent layer to climb over it while maintaining the in-plane epitaxy. However, we have not noted any differences in the SQUIDs, which could be traced to the angle of incidence during ion milling.
After the YBCO layer has been patterned into the SQUID pattern by acid etching, the sample is completed by depositing ~1000 Å of Ag in 1 mTorr oxygen ambient at room temperature through a shadow mask to form contacts. After this step the sample is ready for testing. Each SQUID sample has four SQUIDs on it with junction widths 10,20,30 and 40μm.

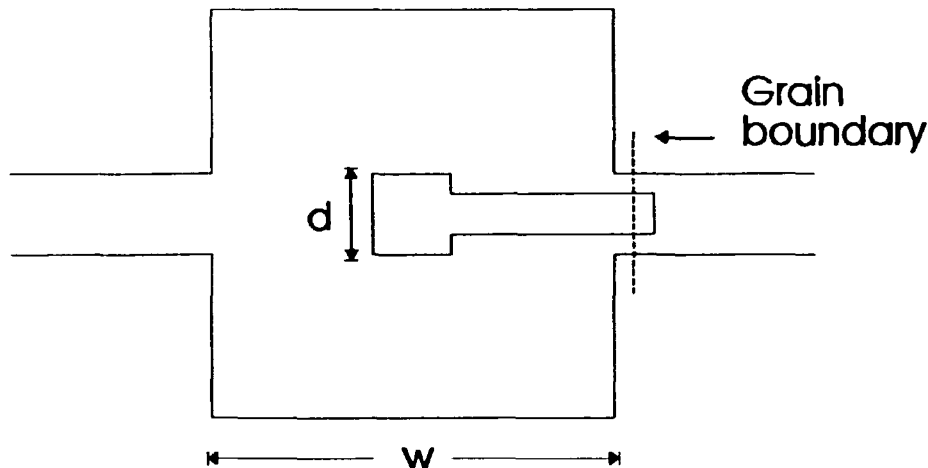

Figure 3.13 The square washer SQUID design. The pattern is aligned such that the edge of the seed layers coincides with the dotted line.

We have used the square washer design developed by Jaycox and Ketchen[41] for all our SQUIDs. This design is shown in Figure 3.13. The washer with outer dimension w has a square hole in it with dimension d. The junctions sit at the end of a slit on the outside of the washer, away from the high field region around the center hole. The inductance for a square washer with no slit has been calculated numerically to be $1.25\mu_0 d$ for w>2d. In many cases, the inductance associated with the slit is the dominating contribution to the total inductance of the SQUID. The slit presents the junctions with a co-planar structure of inductance $\frac{1}{2}\mu_0 l$, where l is the length of the slit. In our case d=25 μm, w=250 μm and l=113 μm. This gives an inductance of 40 pH for the washer and 71 pH for the slit. A lower boundary on the inductance of the junctions can be estimated from the small signal value of the Josephson inductance L_j for bias currents below I_0. In that case $L_j=\hbar/(2eI_0\cos\delta_0)$. Taking the minimum value for $\delta_0=0°$ and using $I_0=20$ μA, we find $L_j=16.5$ pH per junction, giving a total SQUID inductance of 144 pH.
In Figure 3.14 we show I-V characteristics in the form of photographs taken from the oscilloscope for one of the best samples we have made. The I-V

characteristic on the left was recorded at 4.2 K and shows a critical current of 140 μA and a normal state resistance of 1 Ω. The characteristic on the right was recorded at 51 K and shows I_0=35 μA and R_n=1 Ω. Note that this characteristic already shows clear signs of noise rounding, i.e. the tangent of the characteristic has a finite slope at $I=I_0$. The noise parameter Γ is 0.0013 and 0.06 in the two cases, respectively. The SQUID exhibits modulation in the V-ϕ characteristic for temperatures up to 80 K, but it is impossible to detect any critical current in the I-V characteristic at these high temperatures. This is understandable, since the noise parameter is 0.81 at 77 K, a number far higher than the value of 0.2, which by computer simulations has been found to be an upper limit for the observation of quantum interference. The number Γ=0.81 is calculated from the fact that the peak-to-peak voltage in the V-ϕ characteristic is maximum for I_B=4.0 μA and thus the critical current is about 2.5 μA. As a final comment on the I-V characteristics we note that they show signs of excess current, i.e. the tangent of the I-V characteristic at high voltages intersects the I-axis at a finite current rather than passing through the origin, as expected for a SIS junction. The excess current is due to elastic Andreev reflections[42] of quasiparticles, as they try to pass from the normal metal like interior of the junction into the superconducting electrodes. This phenomenon is not observed for perfect SIS junctions because quasiparticles can not exist in the insulating layer. Our junctions must therefore be of the SNS type or, most likely, they consist of a mixture of SNS and SIS regions (S, I and N refer to superconductor, insulator and normal metal, respectively).

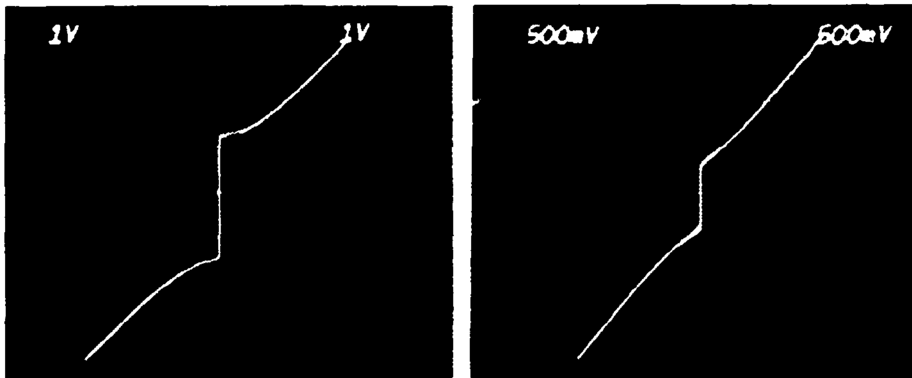

Figure 3.14 Left: I-V characteristic at 4.2 K. X-axis: 100 μV/cm. Y-axis: 100 μA/cm. Right: I-V characteristic at 51 K. X-axis: 50 μV/cm. Y-axis: 50 μA/cm.

In Figure 3.15 we show V-ϕ traces from the plotter for temperatures close to 77 K. In each trace the bias current was adjusted to give maximum peak-to-peak voltage. The modulation is visible for temperatures up to 80 K. From the spacing ΔB of the maxima it is possible to determine the effective area A_{eff} of the SQUID through the relation $\Delta B A_{eff}=\phi_0$. We find $\Delta B=2.5\times10^{-7}$ T and thus $A_{eff}=8.2\times10^{-9}$ m^2. The physical size of the hole in the washer is 2.6×10^{-9} m^2, giving a flux focussing factor (the effective area relative to the physical area) of 3.15. The flux focussing capability of the SQUID is a manifestation of the

Meissner effect. This number is somewhat lower than what we usually see in our SQUID samples. The lower value is due to the fact that this particular SQUID is part of a magnetometer with a defunct flux transformer and thus part of the area is screened by the windings in the coil.

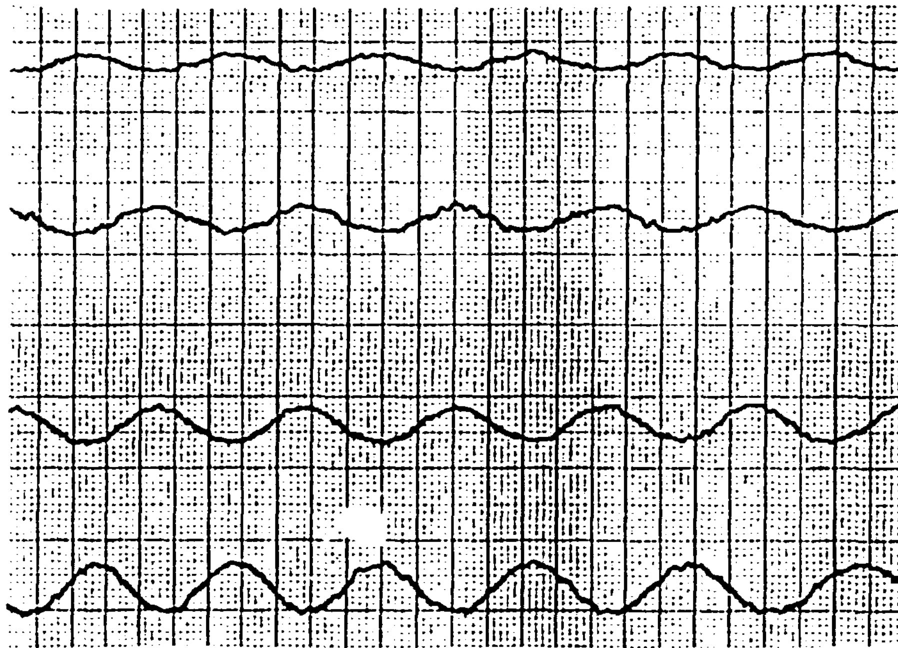

Figure 3.15 V-ϕ characteristic for temperatures close to 77 K. The four traces are recorded at (from the bottom) 76 K, 77.5 K, 79 K and 80 K with bias currents I_B=4.8 μA, 4.0 μA, 3.6 μA, and 3.0 μA, respectively. X-axis: 1.1×10^{-7} T/cm. Y-axis: 1μV/cm.

In Figure 3.16 we show the result of a noise measurement performed at 4.2 K on a sample similar to that shown in Figures 3.14 and 3.15. The figure shows the RMS value of the flux noise, both when the SQUID is operated in the ordinary flux locked loop and when the double modulation technique is employed. In the flux locked loop the noise displays a 1/f behavior for frequencies up to 1000 Hz. When the double modulation is employed, the flux noise is reduced by a factor of about 3 at low frequencies, and the cross-over to the white noise level seems to take place around 100 Hz. This reduction is equivalent to a reduction by one order of magnitude in the noise energy and demonstrates that critical current fluctuations dominate the 1/f noise in this type of SQUIDs, at least at 4.2 K. From the measurement in the double modulation mode the white noise level is found to be $2\times10^{-5}\ \phi_0/\mathrm{Hz}^{1/2}$. With a SQUID inductance of 144 pH this corresponds to a white noise energy $\varepsilon_w=5.9\times10^{-30}$ J/Hz. This particular sample has $I_0=100\ \mu$A and $R_n=1\ \Omega$ at 4.2 K and thus $k_BTL/R=8.3\times10^{-33}$ J/Hz, a factor of 700 less than ε_w. However, the SQUID is far from optimized for white noise, since $\beta=2LI_0/\phi_0=13.9$ at 4.2 K.

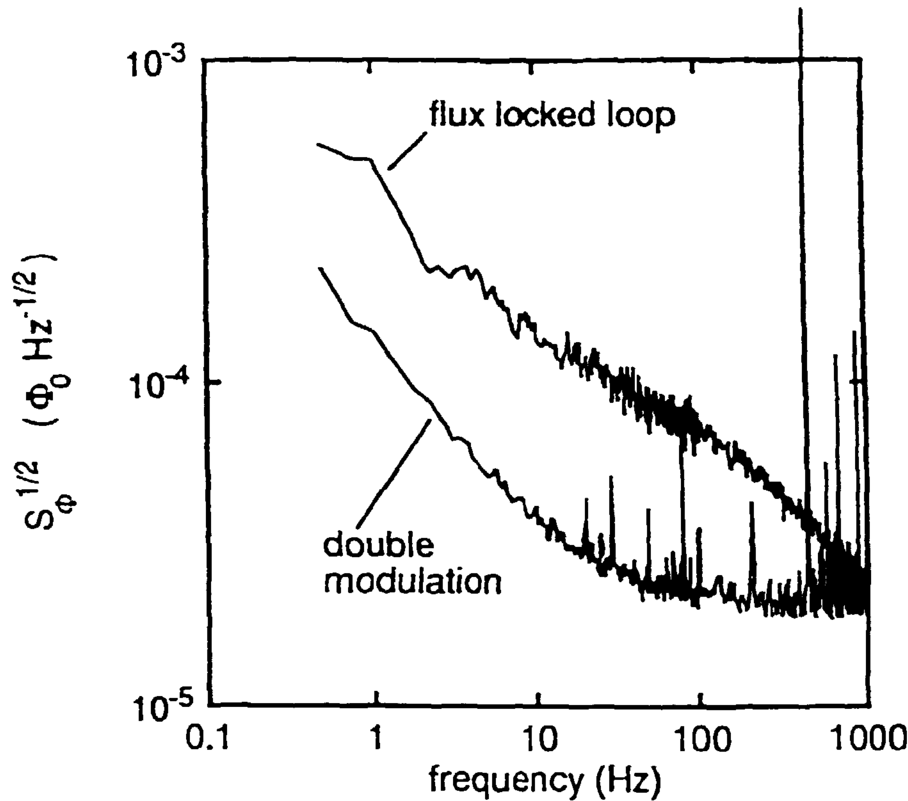

Figure 3.16 RMS value of the flux noise at 4.2 K from a bi-epitaxial SQUID measured in the flux-locked loop mode of operation and with the double modulation technique using a bias current reversal frequency of 2 kHz.

To put things in perspective, we compare in Figure 3.17 the RMS value of the noise in our SQUID to the bi-crystal SQUID fabricated by the IBM group reported in Ref. 32. For our own SQUID we have used the data for the measurement in the flux locked loop, while for the IBM SQUID we have used $\varepsilon_w=3\times10^{-31}$ J/Hz and cross-over frequency 78 kHz. Note that the data for the IBM SQUID are recorded at 77 K. Also shown for comparison are the noise levels in commercial and state of the art DC low T_c SQUIDs. Unfortunately, we do not have data for the IBM SQUID at 4.2 K (or for our SQUID at 77 K), but the 1/f noise is undoubtedly significantly lower at this temperature. The dotted line indicates the expected white noise level in our SQUID at 77 K, assuming that the noise energy scales with temperature as discussed in section 3.1.3. The reason for the better performance of the IBM SQUID it most likely due to the different nature of the grain boundaries created in the bi-epitaxial and bi-crystal processes. Kawasaki[43] et al have performed noise measurements on bi-crystal junctions and found that the magnitude of the relative critical current fluctuations $\delta I_0/I_0$ and the relative resistance fluctuations $\delta R/R$ are about the same. This is expected for a homogeneous tunnel junction, since in that case the probability of tunneling is the same for quasiparticles and Cooper pairs. Miklich[19] et al have performed the same kind of measurement on bi-

epitaxial junctions and found that $\delta I_0/I_0 >> \delta R/R$. They explain the data with a model of the junction consisting of a large number of filaments, all having the same conductance σ_0, but only one of which (or a few) support a critical current.

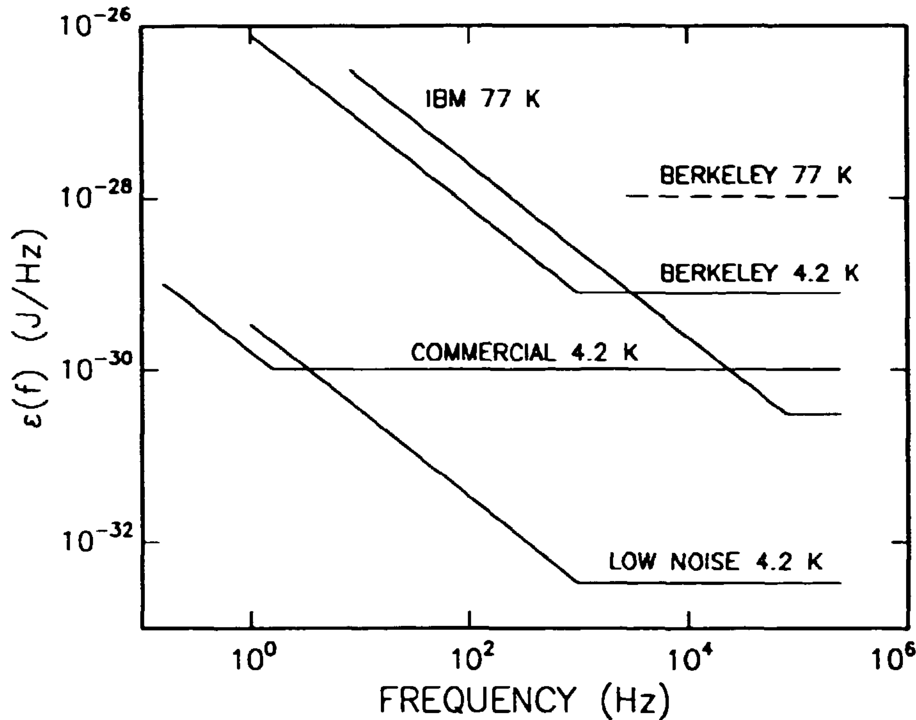

Figure 3.17 Comparison of the noise level in our bi-epitaxial SQUIDs with a SQUID from the IBM group based on bi-crystal junctions, measured at 77 K and having the lowest level of white noise reported to date at this temperature. The broken line indicates the expected white noise level of our SQUID at 77 K. Also shown for reference is the noise in commercial DC SQUIDs (based on low T_c materials) and in a state of the art low T_c DC SQUID[44] having a white noise energy of only 5h.

This picture of the junctions arises if one considers what happens as the angle of the grain boundary is increased from 0° to 45°. The creation of the boundary leads to the formation of dislocations along the boundary. This is illustrated in Figure 3.18. Initially, as the angle is very small, the distance between the dislocations is large and thus they have negligible effect on the current carrying capability of the boundary. However, when the angle approaches 45°, the spacing between the dislocations becomes comparable to the coherence length, and the junction properties will then be determined by the nature of the dislocations. If their spatial extension in the direction perpendicular to the grain boundary is comparable to the coherence length, then most of the dislocation cores will still support a super current. However, if one imagines that the extension of the cores is increased further, then the probability that they will still carry a supercurrent decreases rapidly, as they

become larger than the coherence length. The difference in homogeneity between bi-crystal and bi-epitaxial junctions can be explained by assuming that the former scenario is true for the bi-crystal junctions, while the latter is true for the bi-epitaxial junctions.

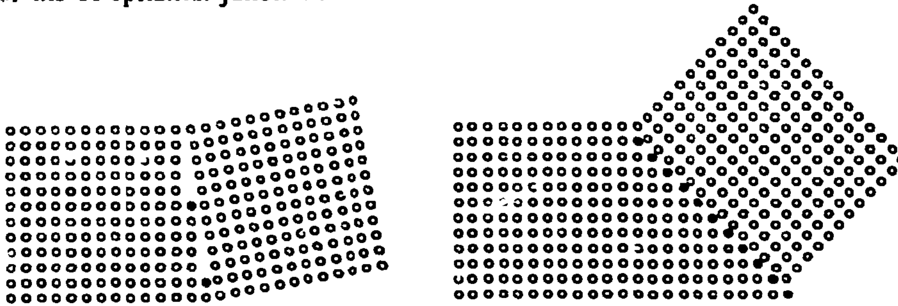

Figure 3.18 This figure shows the arrangement of the atoms in the a-b plane on either side of the grain boundary in the two cases where the angle of the boundary is 10° (left) and 45° (right). Clearly, the density of dislocations (black dots) is higher for large angles than for small angles.

The discussion above should make it clear why it is desirable to be able to fabricate grain boundary junctions with angles less than 45°. If, for instance, the angle is only 30°, as mentioned in the discussion of the optimization of the CeO_2 deposition, the spacing between the dislocations would be larger, and the coupling between the two sides of the junction would not be completely dominated by them.
Another possible explanation for the relatively poor performance of our SQUIDs is that our films have higher levels of flux noise. During the optimization of the deposition parameters this property of the films has not been taken into account, partly because it is a very tedious task if one wishes to do it systematically. However, from measurements performed at UC Berkeley on films fabricated by other groups, we know that the flux noise in our films on MgO buffered with $SrTiO_3$ is relatively high[45]. This fact was the primary motivation for taking up SQUID fabrication on YSZ substrates, as we shall describe in the next section.

3.3.2 SQUIDs on YSZ substrates

There are other important reasons for developing a SQUID process on YSZ substrates besides the wish for lower flux noise in the YBCO films. It is known from studies of the in-plane epitaxy of YBCO on MgO (like those described in Chapter 2) that often a significant fraction of the superconductor grows misaligned with respect to the substrate, thereby reducing the critical current density. This unfortunate feature is generally attributed to defects in the substrate surface. These defects are in some cases present already at the time when the substrates are delivered from the supplier, or they develop over time as a result of MgO being hygroscopic, even if the substrates are stored in a desiccator. We have also observed these misalignments in some of our films

deposited directly onto MgO. We have tried to anneal the substrates for several hours at 1100°C before the deposition, but this approach did not solve the problem. Neither did an attempt to deposit YBCO at higher temperatures than 760°C.

For some applications, such as flux transformers, a modest level of defects is tolerable, since the critical current density of the superconductor in this case is limited by the disorder introduced by the patterning of the layers, rather than by defects in the film itself. However, for bi-epitaxial SQUIDs, where the requirements of the in-plane epitaxy are much more stringent, it becomes of paramount importance to eliminate defects as much as possible. Since the defects originate in the substrate rather than as a result of the processing, it becomes necessary to look for some other suitable substrate.

The obvious choice would be to use $SrTiO_3$, since this substrate displays almost perfect lattice matching to YBCO. However, it is also one of the most expensive substrate materials. We have therefore chosen to use YSZ in combination with suitable buffer layers. The need for buffer layers is obvious, considering that the in-plane orientation of YBCO on YSZ depends on the deposition temperature, as already mentioned. The first candidate that comes to mind is again $SrTiO_3$. We have not used this material, however, for fear that it might also display a temperature dependent in-plane orientation. Instead we have followed an approach first described by a group at Los Alamos (Ref. 38) and used CeO_2 as the primary buffer layer. Since we want to use the same materials for the seed layers as before, we have to be able to deposit $SrTiO_3$ epitaxially at some point. As mentioned earlier, $SrTiO_3$ on CeO_2 grows (110) oriented, but by using $PrBa_2Cu_3O_7$ (PBCO) as an intermediate buffer layer, $SrTiO_3$ can be made to grow (100) oriented. The basic design of the process then becomes as in Figure 3.7 with the MgO substrate replaced by a YSZ substrate with CeO_2 and PBCO buffer layers.

We are now faced with an optimization problem similar to that encountered in the fabrication of SQUIDs on MgO substrates, but this time with even more parameters because of the increased number of layers. Luckily, for some of the parameters it is possible to make good guesses, at least as a first approximation. For instance, since the YBCO and PBCO differ by only one atom in the unit cell, it makes sense to use the same parameters for these two materials.

Initially, we investigated the growth of CeO_2 on YSZ simply by growing it to a thickness of ab[illegible] Å in 150 mTorr and at the three temperatures 780 °C, 810 °C and 840 °C. The films were examined by X-ray θ-2θ scans (data not shown). In all three cases the film grew (100) oriented, with no signs of the (111) reflection, which is the most powerful powder diffraction peak. The full width at half maximum for the (002) reflection was significantly smaller for the sample deposited at 810 °C than for the other two. We have therefore fixed the parameters for the first CeO_2 layer at T_s=810 °C and P_{O_2}=150 mTorr. Note that this is 30 °C higher than for CeO_2 grown on MgO.

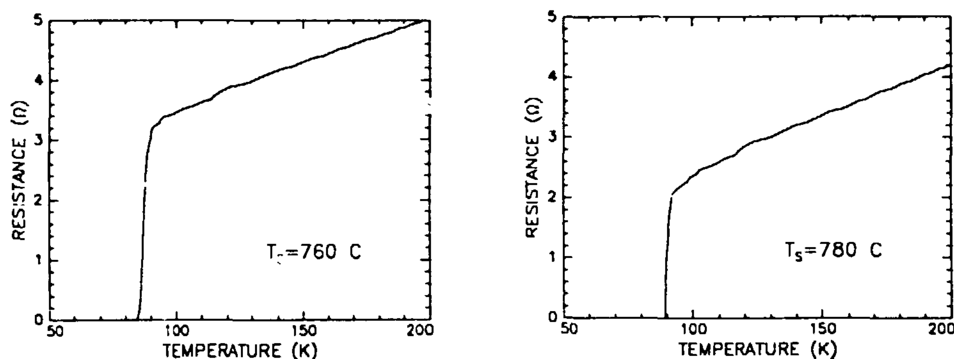

Figure 3.19 R(T) for two samples of YBCO on a YSZ substrate with CeO_2, PBCO and $SrTiO_3$ as buffer layers. The YBCO, PBCO and $SrTiO_3$ were deposited at T_s=760°C (left) and at T_s=780°C (right).

We now turn to the question of the next two buffer layers, PBCO and $SrTiO_3$. In both cases we have used the parameters from the deposition on MgO as initial guesses, i.e. T_s=760 °C and P_{O2}=200 mTorr for PBCO (same as YBCO) and T_s=760 °C and P_{O2}=150 mTorr for $SrTiO_3$. Since we want to grow these two layers relatively thin, we have evaluated them by growing a YBCO layer on top and characterized it. In Figure 3.19 we show R(T) for two samples. On the left the PBCO, $SrTiO_3$ and YBCO were grown at 760 °C; on the right they were grown at 780 °C. In both cases the oxygen pressures were 200 mTorr, 150 mTorr and 200 mTorr for the three layers, respectively. Clearly, the sample on the right has the higher T_c (89 K versus 85 K) and the narrower transition. In Figure 3.20 we show θ-2θ and φ-scans for this sample. The θ-2θ scan is consistent with the YBCO film being c-axis oriented, although the strong (103) reflection from YBCO coincides with the CeO_2 (200) peak. These two reflections are 0.40° apart in 2θ, but as mentioned earlier, the resolution of the spectrometer is only 0.80° in θ-2θ scans. The φ-scan on the YBCO (102) has only one peak in the 90° range shown, indicating that the film is fully aligned in the a-b plane. The φ-scan is performed on the YBCO (102) rather than the YBCO (103) to avoid coincidence with the $SrTiO_3$ (101) and the PBCO (103). The relative orientation of the YBCO film with respect to the substrate was determined by locating the YSZ (202) reflection. It was found at φ=142°, indicating that the YBCO is rotated 45° with respect to the substrate because the YBCO (102) reflection occurs at φ=97°. This means that CeO_2 aligns with YSZ and the PBCO in turn rotates 45° on CeO_2. $SrTiO_3$ and YBCO align with PBCO because of the lattice match. We have thus demonstrated that good quality YBCO can be grown on YSZ with CeO_2, PBCO and $SrTiO_3$ as buffer layers.

Next we discuss the deposition of the seed layers MgO and CeO_2 on top of the buffer layers. For the MgO deposition we have simply adopted the same parameters as in the previous section, because MgO does not appear to be particularly sensitive to T_s or P_{O2}. For instance, we have deposited MgO at T_s=600 °C and T_s=650 °C and at P_{O2}=2 mTorr and P_{O2}=5 mTorr with no discernible difference in the outcome.

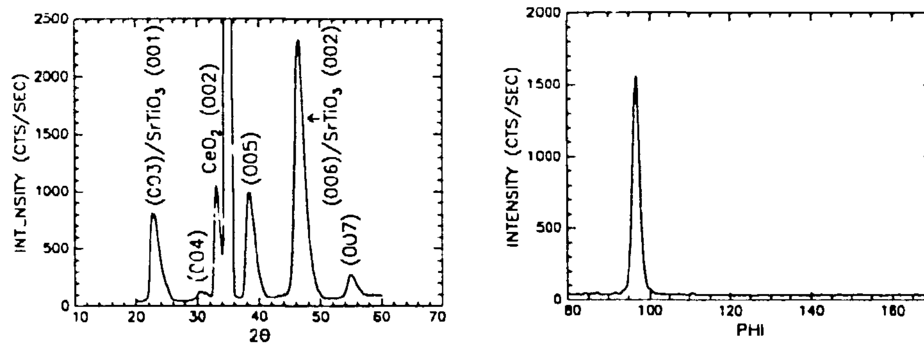

Figure 3.20 θ-2θ scan and φ-scan on YBCO (102) for the sample whose R(T) curve is shown in Figure 3.19, right. These scans demonstrate that the film grows c-axis oriented and with good in-plane epitaxy.

For the CeO_2 deposition we have kept the oxygen pressure constant at P_{O2}=150 mTorr and varied the temperature in the range 770 °C to 810 °C. Again, because we want to grow the seed layers thin, we have evaluated them by growing YBCO on top and measuring the R(T) curve and the φ-scan. Because of the poor resolution of the X-ray spectrometer we have noticed that sometimes the YSZ (111) shows up in the φ-scan on YBCO (102), even though they are about 0.8° apart in 2θ. The distance in χ-angle is about 1°, but as usual the resolution in this direction is even worse. At this point it is useful to recall that when we grow all six layers on top of each other (CeO_2, PBCO, $SrTiO_3$, MgO, CeO_2 and YBCO) we expect the YBCO to be aligned with the YSZ substrate and to be rotated 45° with respect to the PBCO and $SrTiO_3$ layers. Any 45° misaligned YBCO will therefore coincide with the YSZ (111) if we do the φ-scan on YBCO (102). However, if we do the φ-scan on YBCO (103), the misaligned YBCO will coincide with PBCO (103) and $SrTiO_3$ (101). There are no other options, because the YBCO (102) is the only reflection which does not coincide with a $SrTiO_3$ reflection and at the same time has sufficient intensity. We have chosen to use YBCO (103) for the φ-scan, since the intensity of the YSZ (111) depends on the alignment of the sample during mounting and thus varies from run to run, making any comparisons impossible. The approach then is to do the φ-scan on YBCO (103) and compare the two peaks that show up, in the hope that it is possible to see a change in their relative intensities as the deposition parameters are varied. In Figure 3.21 we show φ-scans for two samples where the upper CeO_2 layer was deposited at 770 °C and 810 °C, respectively, together with the R(T) curve for the YBCO. The YSZ (202) occurred at φ=91° and φ=273°, respectively, in the two scans. The two peaks at φ=46° and φ=317° can therefore be identified as coming from the $SrTiO_3$ and PBCO layers, or possibly from misaligned YBCO. Clearly, the peak is relatively much smaller for the sample where the CeO_2 was deposited at 810 °C. This trend is confirmed by the measurements on a sample with T_s=790 °C during the CeO_2 deposition (data not shown). In that case the relative size of the peak was in between the two cases shown in Figure 3.21. Since also the R(T) curve is better for the sample deposited at T_s=810 °C, we chose this temperature for the deposition of the upper CeO_2 layers.

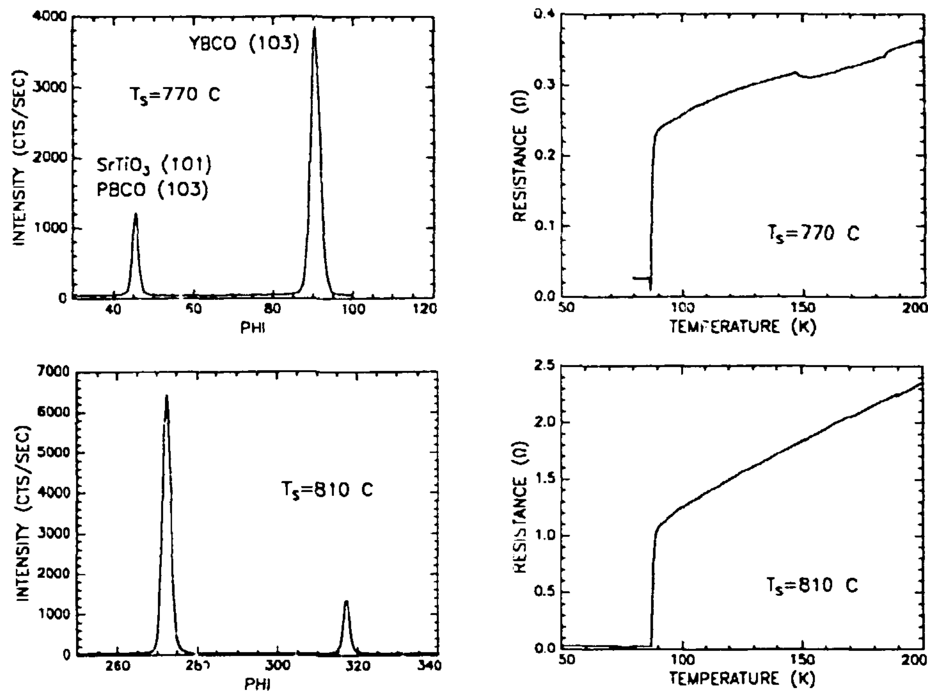

Figure 3.21 φ-scan on YBCO (102) and R(T) for two samples consisting of all six layers (CeO_2, PBCO, $SrTiO_3$, MgO, CeO_2 and YBCO on YSZ). The upper CeO_2 layer was deposited at 770 °C in the two top graphs and at 810 °C in the two bottom graphs.

We have not changed the way the patterning of the seed layers is performed and the SQUID process on YSZ can thus be summed up as in Table 3.3 below. It is interesting to note that the layers are deposited 20 °C to 30 °C hotter in this case compared to the MgO substrates. One possible explanation is that the emissivity of YSZ is higher than that of MgO, and thus the actual surface temperature for a given temperature of the substrate holder is lower for YSZ than for MgO.

In Figure 3.22 we show V-ϕ traces for one of the best SQUID samples we have made on YSZ. This particular trace was recorded with the sample immersed in liquid nitrogen. The curve was recorded with I_B=7.4 μA, which gives a maximum peak-to-peak voltage of 0.85 μV. This number is comparable to the result from the SQUIDs on MgO at this temperature. We can determine the effective area of the SQUID in the same way as before and we find $A_{eff}=1.98\times10^{-8}$ m^2. The physical size of the hole is the same as for the SQUID on MgO. The flux focusing factor is thus 7.6.

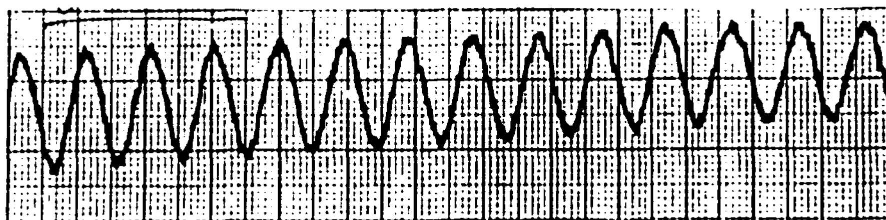

Figure 3.22 V-ϕ characteristic for a SQUID sample on a YSZ substrate recorded with I_B=7.4 μA at 77 K. X-axis: 1.1×10^{-7} T/cm. Y-axis: 0.5 μV/cm.

Material	Temp. (°C)	Pressure (mbar)	Thickness (Å)	Patterning
CeO_2	810	150	100	None
PBCO	780	200	100	None
$SrTiO_3$	780	150	800	None
MgO	600	2	100	Ion milled at 500 V, 0.8 mA/cm^2 at 60° to the normal for 2½ min.
CeO_2	810	150	100	
CeO_2	810	150	100	None
YBCO	780	200	3000	Acid etched in 0.05% HNO_3
Ag	20	1	1000	Shadow masked

Table 3.3 Summary of the fabrication process for bi-epitaxial SQUIDs on YSZ substrates. The second, third and fourth columns give the substrate temperature in °C, oxygen ambient pressure in mTorr and thickness in Å, respectively.

In Figure 3.23 we show the spectral density of the flux noise for a bi-epitaxial SQUID on a YSZ substrate measured at 4.2 K using the flux locked loop mode of operation. This measurement was performed at Physics Laboratory I at the Technical University of Denmark using an experimental setup which is essentially identical to the equipment at UC Berkeley. Note that the Y-axis is calibrated in volts with 1 V corresponding to ϕ_0. We have indicated the noise level at 10 Hz and 500 Hz in the figure; since the cross-over frequency between the 1/f noise and the white noise appears to be located between 300 Hz and 400 Hz, the noise at 10 Hz and 500 Hz is indicative of the 1/f and white noise levels, respectively. By comparing to Figure 3.16 we find, somewhat to our surprise, that the 1/f noise in the SQUID on the YSZ substrate is higher than the 1/f noise in the SQUID on MgO by a factor of about 3.5 ($S_\phi^{½}$ (10 Hz) = 5.9 x 10^{-4} ϕ_0 / $Hz^{½}$ on YSZ versus 1.7 x 10^{-4} ϕ_0 / $Hz^{½}$ on MgO). Since the measurement was performed using the flux locked loop technique, it is reasonable to assume that the dominant contribution to the 1/f noise comes from critical current fluctuations, just as in the case of the SQUID fabricated on MgO, where we found that the noise could be reduced by a factor of three by using the double modulation technique. If we assume that the

critical current fluctuations are of the same magnitude in the two cases (this is the best we can do since we do not at present have access to the double modulation technique at the Technical University) then these results suggest that the flux noise is actually higher in films deposited on buffered YSZ than in films deposited on buffered MgO. Finally, regarding the white noise level we find that $S_\phi^{1/2}$ (500 Hz) = 1.6×10^{-4} $\phi_0/Hz^{1/2}$ in the YSZ sample versus 2.0×10^{-5} $\phi_0/Hz^{1/2}$ in the MgO sample, i.e. the noise is 8 times higher in the YSZ sample. This difference is partially explained by the fact that the normal state resistance is 3 times lower in the YSZ sample (the white noise level is inversely proportional to the normal state resistance).

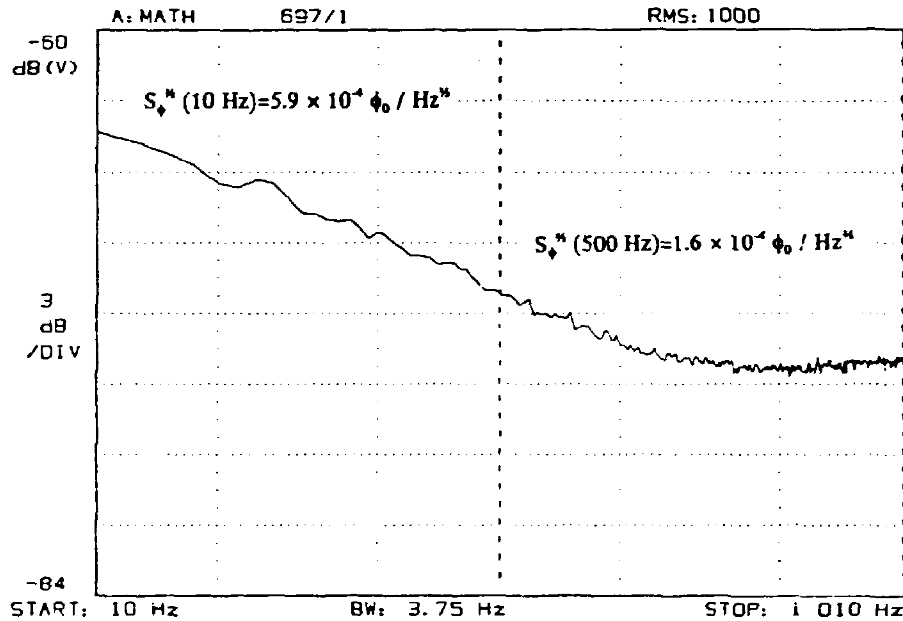

Figure 3.23 The spectral density of the flux in the SQUID sample on YSZ. The Y-axis is calibrated in volts with -60 dBV corresponding to 10^{-3} ϕ_0 / $Hz^{1/2}$.

After the noise in the YSZ SQUID was measured we have been informed that the Berkeley group has measured the flux noise in YBCO films deposited on buffered YSZ substrates. They find that at 77 K the noise is typically 10^{-3} ϕ_0 / $Hz^{1/2}$. This is to be compared with flux noise measurements on films on buffered MgO, where they previously have found values in the range 10^{-4} to 10^{-3} ϕ_0 / $Hz^{1/2}$ in several films measured at temperatures around 60 K. Although the temperature dependence of the flux noise is very sample dependent (the noise can go either way with increasing temperature), these numbers suggest that the flux noise is not smaller in films on YSZ than in films on MgO. Thus, we have to conclude that buffered YSZ is not better suited than buffered MgO for the fabrication of quiet SQUIDs.

It is reasonable to assume that the flux noise is related to the strength of the flux pinning in the films. Since also the critical current density is related to the flux pinning, it might be useful in future work to investigate how J_c changes when various buffer layers are deposited on a given substrate material, before one sets out to develop a bi-epitaxial process for this particular substrate.

3.4 Magnetometers

In this section we will describe our work on the fabrication of an integrated magnetometer, i.e. a SQUID and a flux transformer combined on the same substrate. Before going into the details of the fabrication process, we will briefly justify the need for flux transformers.

If one compares the magnitude of the biomagnetic signals with the field sensitivity of a bare SQUID, it becomes apparent that even the most quiet SQUIDs can not detect the weakest of these signals. The most sensitive SQUIDs made to date have equivalent flux noises on the order of $10^{-6}\ \phi_0/\mathrm{Hz}^{1/2}$ in the white noise region with an effective area of a few times $10^{-9}\ \mathrm{m}^2$. This places their field sensitivity around 1 $\mathrm{pT/Hz}^{1/2}$, corresponding to the level of the magnetic signal from a fetal heart, but about one order of magnitude above even the strongest signals from the human brain[46]. The field sensitivity can not be increased by increasing the area of the SQUID, since this will lead to higher loop inductance, reduced transfer coefficient and higher equivalent flux noise. One is thus led to the idea of using an external device to focus more flux into the SQUID loop.

The flux transformer consists of a pick-up coil with inductance L_p in series with an input coil L_i. The input coil is placed in close vicinity to the SQUID, which has inductance L_s. Flux is then coupled to the SQUID via the mutual inductance $M=\alpha(L_sL_i)^{1/2}$, where α is the coupling constant. Assume that a flux ϕ_a is applied to the pick-up loop. This will induce a current $I=\phi_a/(L_p+L_i)$ in the flux transformer. Consequently, the flux coupled to the SQUID will then be $\phi_s=MI=\alpha\phi_a(L_sL_i)^{1/2}/(L_p+L_i)$. For a given L_p, the maximum flux transfer ϕ_s/ϕ_a will be $\alpha(L_sL_p)^{1/2} / 2L_p$ for $L_i=L_p$. In practice the pick-up coil has a very large area compared to the input coil, and it is necessary to let the input coil have several turns to satisfy $L_i=L_p$. The inductance of the input coil L_i depends on the coupling to the SQUID. The tightly coupled case has been treated by Ketchen[47]. He finds that $L_i=n^2L_s$, where n is the number of turns on the input coil. With $L_i=L_p=n^2L_s$ the maximum flux transfer is $\phi_s/\phi_a=\alpha/2n$. For a five turn input coil (as we have used) one then finds that at most 10% of the flux applied to the pick-up loop is coupled into the SQUID loop. However, if one considers the field density by putting $\phi_s=B_sA_{eff}$ and $\phi_a=B_aA_p$, one finds $B_s/B_a=(A_p/A_{eff})\ (\alpha/2n)$. With typical numbers $A_p=1\ \mathrm{cm}^2$ and $A_{eff}=10^{-8}\ \mathrm{m}^2$, this suggests that it should be possible to increase the field sensitivity compared to a bare SQUID with a factor of up to 1000 (for $\alpha=1$). This opens up the possibility to detect the full range of biomagnetic signals, including the weakest signals from the brain.

In practice it is necessary to screen the magnetometer from outside sources such as fluctuations in the earth's magnetic field, power lines etc., since they easily exceed the biomagnetic signals by several orders of magnitude. One way to make the magnetometer less sensitive to outside sources is to change the geometry of the pick-up loop, such that it consists of two equal area loops wound in opposite directions. The resulting device is called a gradiometer, since it is sensitive to gradients of the magnetic field, but not to spatially

homogeneous fields. The magnetic field from any source varies more rapidly with distance close to the source than far away from it. The gradiometer will thus be much more sensitive to the signal source close to it than to the noise source far away from it. This is one more good reason to consider coupling a superconducting flux transformer to the SQUID, since a dc gradiometer can only be fabricated in this way.
From a fabrication point of view, the easiest way to achieve a magnetometer is to fabricate the SQUID and the flux transformer on separate substrates and then couple them together as closely as possible. This flip-chip bonding technique is well known from the low T_c materials and it has also been demonstrated in the high T_c materials[48]. The main drawbacks of the technique are that the coupling is less than optimal because it is necessary to insert a sheet of mylar between the two components in order to isolate them from each other electrically and also, the input coil and the SQUID body have to be aligned to within a few microns; this can be a very tedious process indeed. Both of these drawbacks are eliminated if one chooses to fabricate both components on the same substrate, as we have done. The coupling is then limited only by the thickness of the insulating layer, which can be controlled in the fabrication process. The alignment problem is virtually eliminated, since it is transferred to the mask aligner, where it can be done very easily compared to the flip chip case. The price one has to pay for this convenience is the added complexity of the combined device, and thus a greater risk of malfunction due to the extra processing steps.
For topological reasons it is necessary in thin film technology to fabricate coils as spirals . This leads to the problem of how to make contact from the inner to the outer turn of the coil. It can be done by connecting them via a cross-over or a cross-under as shown in Figure 3.24 (gray shaded pattern), i.e. it is necessary to use two superconducting layers separated by an insulator. There are several requirements to be satisfied by the insulating material. The most important of these is that it has to be able to support epitaxial growth throughout the tri-layer; in particular, the top YBCO layer should be able to grow epitaxially on the insulator. Also, the insulator should be able to withstand the substrate temperature during the deposition without diffusing into or reacting chemically with the superconductor, and it should be possible to pattern it using standard photolithographic processes.
Potential candidates for the insulating layer include $SrTiO_3$, CeO_2 and MgO. However, as we have seen in the development of the SQUID processes, MgO requires a buffer layer to protect it from the photoresist during the patterning. Of the remaining two materials, CeO_2 is the most attractive, because $SrTiO_3$ with its high dielectric constant will add capacitance to the junctions in the SQUID and this might place them in the hysteretic regime. We have therefore tried to develop a process for crossovers and interconnects using CeO_2 as the insulator. It is known from earlier work that $SrTiO_3$ will work as insulator for flux transformers for flip chip arrangements (Ref 39).

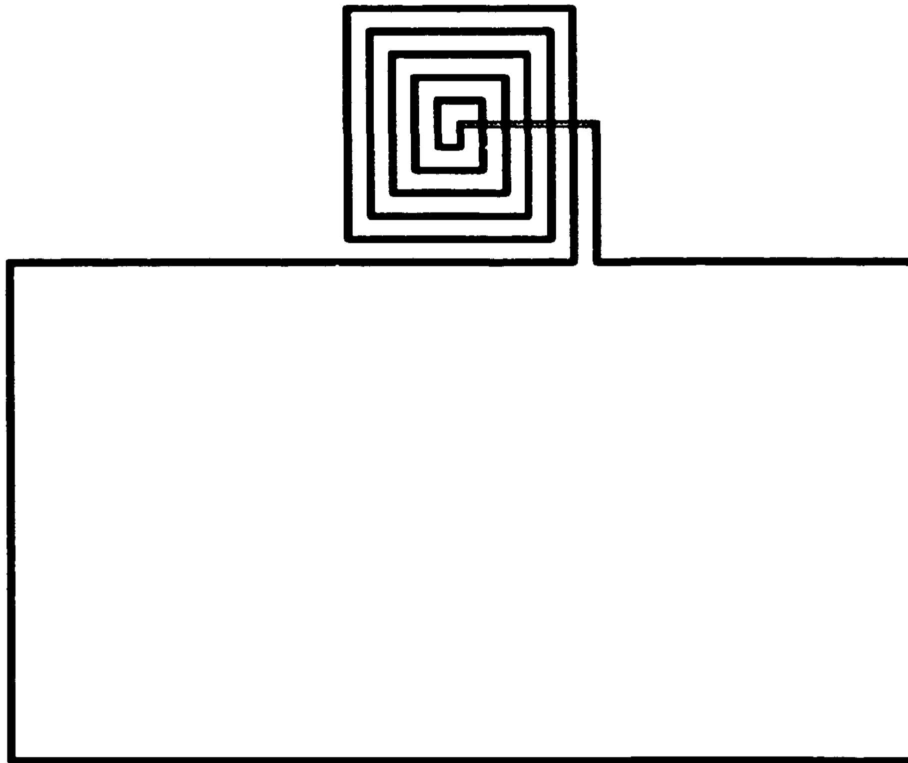

Figure 3.24 The flux transformer consists of a large area pick-up loop in series with a multi-turn input coil. The inner turn of the input coil is connected to the pick-up loop via the cross-under (shown gray shaded).

During the development of the process we fabricated samples consisting of three layers as shown in Figure 3.25. Initially, we deposited the bottom YBCO layer, which we patterned into a 100 μm wide stripe, with a pad at each end for contacts. Next, we deposited the insulating layer through a shadow mask so as not to cover the pads in the bottom layer. We then ion milled two holes (50×30 μm^2) through the insulator down to the bottom YBCO layer. The samples were completed by depositing the top YBCO layer and patterning it into four stripes with pads. Two of the stripes made contact to the bottom YBCO layer through the holes (windows) in the insulator, while the other two did not. In this way it is possible to check whether there really is contact between the two superconducting layers through the windows and insulation between them at the crossovers.

Initially, it is useful to check the growth of CeO_2 on YBCO. In Figure 3.26 we show a θ-2θ scan for a sample consisting of 3000 Å of YBCO on an MgO substrate, followed by 5000 Å of CeO_2. All the peaks can be identified as $(00l)$ peaks from either YBCO or CeO_2. In particular, there is no sign of the CeO_2 (111) reflection at $\theta = 28.6°$. Since we already know from the SQUID processes that YBCO grows c-axis oriented on CeO_2 we conclude that it should be possible to grow a YBCO/CeO_2/YBCO tri-layer with the c-axis perpendicular to the substrate for all three layers.

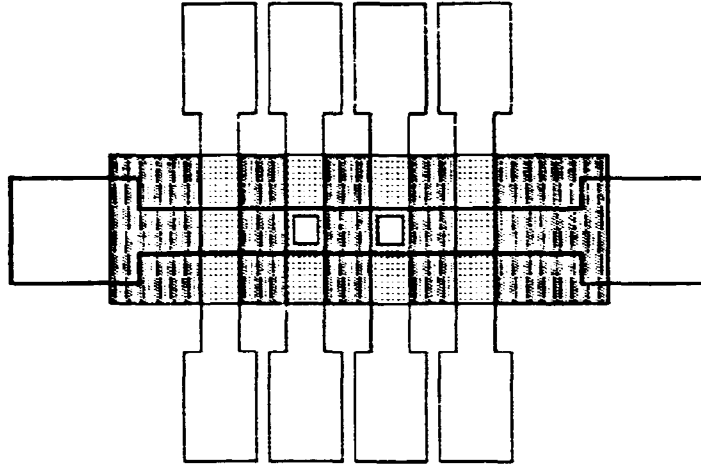

Figure 3.25 Schematic showing the layout of the interconnect samples used to develop the process for flux transformers. The horizontal stripe is deposited first. Next comes the insulating layer (shown dark shaded) with the two windows, and finally the four vertical top stripes. The top and bottom stripes make contact through the windows.

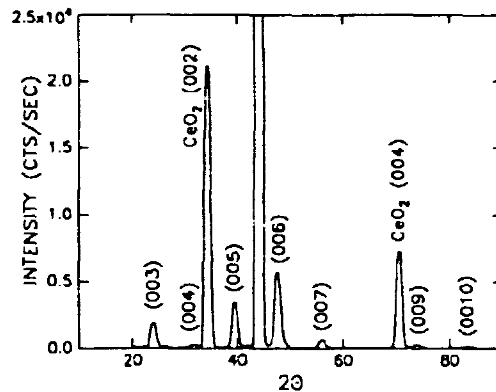

Figure 3.26 θ-2θ scan for a sample with CeO_2 on YBCO on a MgO substrate. The scan indicates c-axis oriented growth for both layers.

Next we turn to the question of how the patterning of the bottom YBCO layer affects the growth of the subsequent layers. The main concern here is what happens at the edge where the insulator and the top YBCO layers have to climb over a step in the bottom YBCO layer. It is known that if the deposition conditions are such that the YBCO grows c-axis oriented, it will tend to follow variations in the slope of the substrate[49]. This means that if it has to grow over a steep edge, the c-axis will locally be parallel to the substrate with the formation of high-angle grain boundaries as a result. To avoid this, it is necessary to perform the patterning such that the slope of the edges is gentle

enough to support c-axis oriented growth. We have tried several approaches to achieve a gentle slope. One of these schemes involve a double ion milling of the bottom YBCO under an angle of 60°. In the first ion milling step, the YBCO on one side of the stripe is removed. The photoresist stencil is then changed to allow the removal of the YBCO on the other side of the stripe. Since the resist stencil recedes slightly during the ion milling, this should result in the edges of the YBCO layer making an angle of less than 30° with the substrate. In practice, however, we always find that the top YBCO displays semiconducting behavior above T_c when we use this method.

The most reliable way to fabricate a working interconnect involves patterning the bottom YBCO by an acid etch (0.05 HNO_3) followed by a further etch in a 1 % solution of Br in methanol. The latter etching step serves a dual purpose. Because it takes place with the resist stencil removed, it will lead to a rounding of the edges. Furthermore, since the thickness of the layer decreases (by a factor of 2 or so), it will flatten the overall shape of the stripe. We have examined a few samples in a scanning electron microscope (SEM) to obtain more information about the effect of the Br etching. The SEM pictures confirmed that the edges of the YBCO stripe are indeed rounded compared to a sample that has not been Br etched. The Br etch leaves a very rough YBCO surface behind, but apparently the overall condition of the stripe is better suited to support the epitaxy of the subsequent layers when the Br etch is performed.

With the bottom YBCO stripe deposited and patterned as described, the next step is to deposit the insulating layer. We find that it is necessary to grow the insulator to a thickness of at least 4000 Å to achieve proper insulation between the two superconducting layers. The reason for this is that very often little particles on top of the bottom YBCO are left behind after the patterning (boulders). These particles can cause shorts between the two superconducting layers, either by themselves or by introducing defects in the form of holes in the insulator. By growing the insulator sufficiently thick, all the boulders will eventually be covered and the problem goes away. Also, we expect a thick insulating layer to be more effective than a thinner layer in rounding the edges created by the pattern in the bottom layer. As far as the patterning of the insulator is concerned, the same considerations apply as for the bottom layer. The most important requirement is that at least one of the sides of the windows has a gentle slope. We have tried acid etching with a 7 % HF solution and ion milling with an angle of 60° between the ion beam and the normal to the sample. Furthermore, we have tried to ion mill both with and without rotating the sample around the normal to the surface. We find that we get the best results when the patterning is done by ion milling without rotation. When the sample is patterned in this way and examined in an optical microscope, it is easy to observe that one of the sides in the window is beveled while the other three appear to be much more steep.

The last step in the fabrication of an interconnect sample involves the deposition and pattering of the top YBCO layer. This layer is grown to a thickness comparable to the thickness of the insulator to ensure good contact through the window. It is patterned by acid etching using 0.05 % HNO_3.

In Figure 3.27 we show data in the form of R(T) curves for an interconnect fabricated as described above using CeO_2 as the insulating material. The top left curve is for the bottom stripe and shows a T_c of 85 K. The top right curve is measured on a stripe in the top layer that does not make contact to the bottom layer. It shows a T_c of 82 K. The bottom left curve is measured from the top layer through the window to the bottom layer and has a similar T_c. Finally, the bottom right curve is measured on the insulating layer only and shows a resistance of about 50 MΩ at room temperature and it increases as the temperature is decreased.

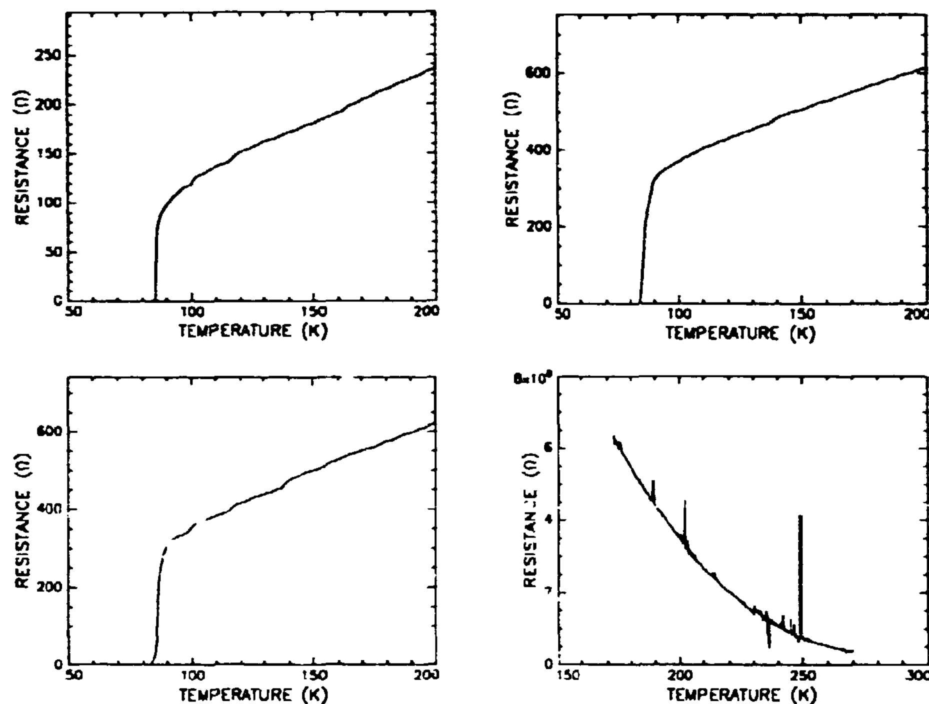

Figure 3.27 R(T) curves for an interconnect using CeO_2 insulating material. Top left: Bottom YBCO stripe. Top right: Crossover stripe. Bottom left: Window contact. Bottom right: Insulator.

While the R(T) curves in Figure 3.27 demonstrate that it is possible to fabricate an interconnect using CeO_2 as the insulator, we have to admit that the yield of the process is very low. Considering that the fabrication of a magnetometer is significantly more complicated than an interconnect, we have chosen not to rely on CeO_2 as the insulator for the magnetometer. Instead we have used either a combination of $SrTiO_3$ and CeO_2 (with $SrTiO_3$ deposited first) or only $SrTiO_3$. It is not possible from the work we have done to say why $SrTiO_3$ works better than CeO_2 for this purpose, but it seems plausible that the explanation is related to the lattice match. On the other hand, it is not clear that a close lattice match is advantageous when the layers are sloped.

It is possible to fabricate the magnetometer in two ways, either by making the SQUID first and putting the flux transformer on top of it, or vice versa. The

advantage of putting the SQUID on the bottom is that it will then be closer to the substrate, and presumably the in-plane epitaxy will be better under control than if it has to be grown on top of a several thousand Å thick insulator. The disadvantage is that the SQUID has to go through the extra processing steps required to complete the flux transformer, in particular the heating and cooling cycles during the depositions. We have tried both possibilities and we find that in general the samples work better when the SQUID is made first.
Placing the SQUID closest to the substrate and putting the flux transformer on top introduces a slight complication. Recall from the SQUID process that after the seed layers have been patterned, a CeO_2 buffer layer is deposited before the YBCO layer. Since the HNO_3 acid used to pattern the YBCO does not affect this buffer layer, we are left with CeO_2 everywhere outside the YBCO pattern and consequently, we can not deposit c-axis oriented $SrTiO_3$. This problem is overcome by introducing an extra step in the SQUID process. After the CeO_2 buffer layer has been deposited, the sample is removed from the deposition chamber and the CeO_2 is removed from most areas of the sample by ion milling, leaving it to cover the edge of the seed layers and extending only 15-20 μm towards the SQUID body (see Figure 3.28). This means that there will be no CeO_2 in the areas which subsequently will be occupied by the flux transformer.

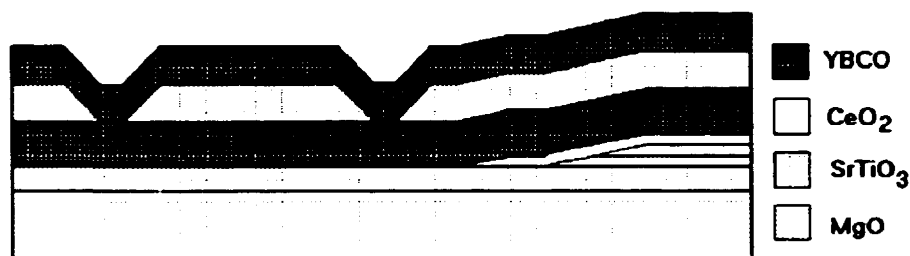

Figure 3.28 Sequence of layers in the magnetometer. The light shaded layers are $SrTiO_3$ while the dark shaded layers are YBCO. Note that the SQUID YBCO layer serves as cross-under for the flux transformer and that the CeO_2 buffer layer has been removed from most parts of the substrate.

In Figure 3.28 we show the sequence of layers that go into the fabrication of a magnetometer. The SQUID is made as described in section 3.3.1, with the addition of the extra step mentioned above. Note that we have used part of the SQUID body as the cross-under, thereby eliminating the need for a third superconducting layer. The layout can be seen in detail in Figure 3.30, which is a photograph of the region around the SQUID of an actual magnetometer. The process is summarized in Table 3.4.

Material	Temp. (°C)	Pressure (mbar)	Thickness (Å)	Patterning
$SrTiO_3$	760	150	1500	None
MgO	600	2	150	Ion milled at 500 V, 0.8 mA/cm^2, 60° to the normal for 2½ minutes
CeO_2	780	150	100	
CeO_2	780	150	100	Ion milled as above for 1 minute
YBCO	760	200	3000	HNO_3 etched and Br etched
$SrTiO_3$	760	150	5000	Ion milled as above for app. 25 minutes
YBCO	760	200	4500	Ion milled as above for app. 20 minutes
Ag	20	1	1000	Shadow masked

Table 3.4 Summary of the magnetometer process. The second, third and fourth columns give the substrate temperature in °C, oxygen ambient pressure in mTorr and thickness in Å, respectively.

In Figure 3.29 we show V-ϕ curves for our best magnetometer sample. It has R_N=0.32 Ω and and I_c=0.80 mA at 4.2 K. The two traces shown are for T=67 K (bottom) and T=73 K. At 67 K the maximum peak-to-peak voltage is about 0.35 μV with a bias current of about 24 μA. From the V-ϕ curve we find that it requires a flux density change of $\Delta B_m=1.94\times10^{-9}$ T to apply one flux quantum to the magnetometer, giving an effective area of 1.06×10^{-6} m^2. This corresponds to a gain of 54 (defined as the effective area of the magnetometer relative to the effective area of the SQUID) compared to the SQUID shown in Figure 3.22. From this measurement it is also possible to estimate the coupling coefficient α. Since it would be interesting to compare α for our integrated magnetometer with the value one finds for a comparable flip-chip arrangement as in Ref 48 (a five turn input coil is used in both cases), we use a value for the pick-up coil which scales with the square root of the area (since the inductance of a closed loop is proportional to the linear dimension). In Ref. 48 an inductance of 20 nH is estimated for a loop with area 81 mm^2. Our pick-up loop has an area A_p=48 mm^2 and consequently we estimate $L_p\approx16$ nH. We take L_s=144 pH, $L_i=n^2L_s$=3.6 nH and $A_{eff}=2\times10^{-8}$ m^2 for the SQUID. In the general case, when L_i and L_p are not matched, the gain g in field sensitivity is given by $g = \alpha\,(A_p/A_{eff}) \times (L_sL_i)^{1/2}/(L_p+L_i)$. With the numbers quoted above and g=54 we find α=0.62. This number is comparable to the flip-chip magnetometer, where α is found to be 0.6.

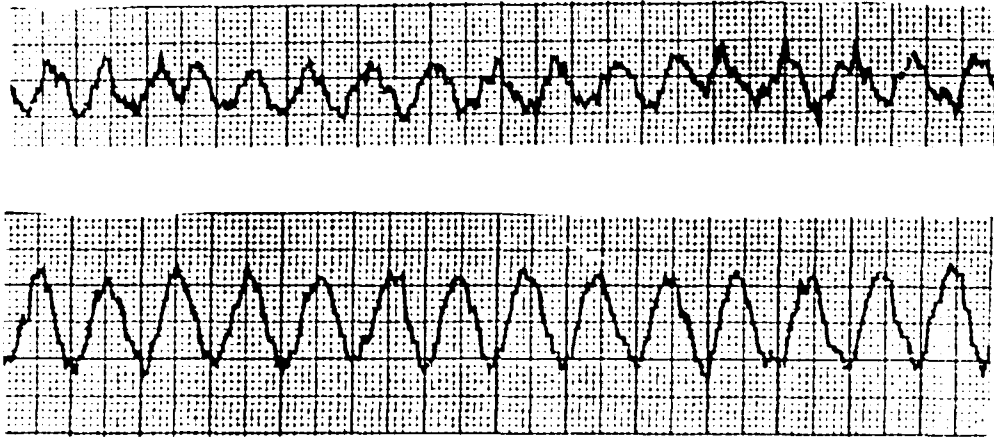

Figure 3.29 V-ϕ characteristic for a magnetometer sample. The two traces are recorded at 67 K (bottom) and at 73 K. X-axis: 2.02×10^{-9} T/cm. Y-axis: 0.25 μV/cm.

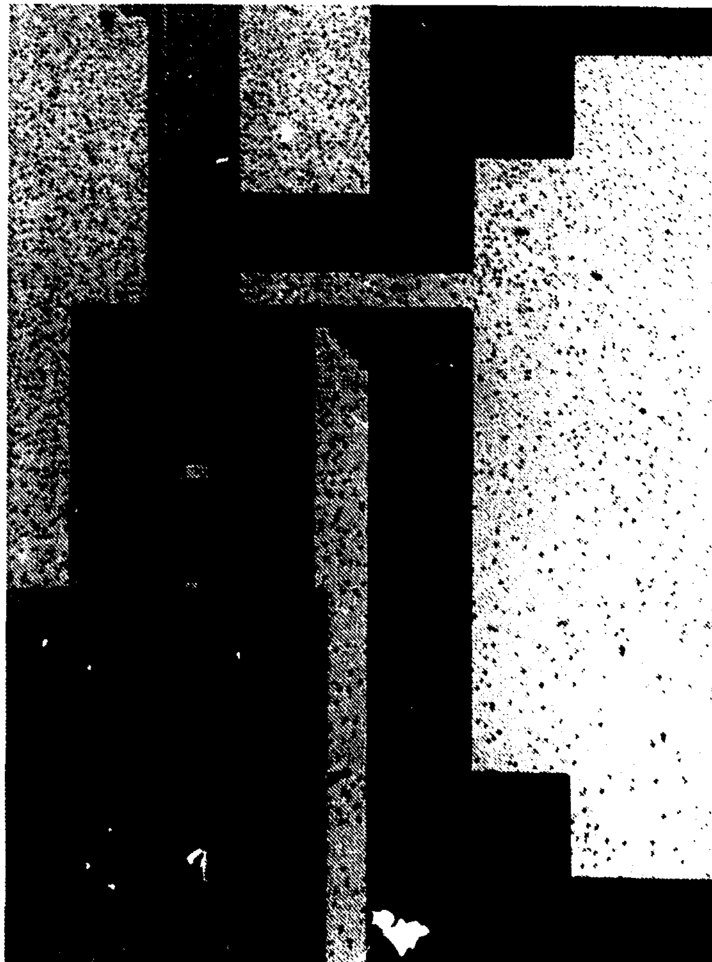

Figure 3.30 This figure shows a photograph of the region around the SQUID in an actual magnetometer sample. The square washer is almost completely covered by the five turn input coil lying on top of it.

3.5 Conclusions

In this chapter we have described our work on the fabrication of SQUIDs by laser ablation using a bi-epitaxial process on MgO and YSZ substrates. In the last part of the chapter we have demonstrated how the SQUIDs can be combined with a flux transformer fabricated on the same chip to form an integrated magnetometer.

Regarding the SQUIDs on MgO substrates we have discussed various ways to achieve an artificial grain boundary of 45° given the epitaxial relationships between the substrate and the buffer and seed layers $SrTiO_3$, MgO and CeO_2. We have shown that, mostly because of the poor quality of the MgO substrates, it is necessary to use a process involving a total of five layers to achieve a reasonable reliability. The correlation between the main parameters describing the laser ablation process (substrate temperature and oxygen ambient pressure) and the epitaxy of the deposited layers has been investigated systematically. In this way we have optimized the deposition parameters such that the two desired in-plane orientations of the YBCO layer can be reproduced routinely. When the depositions are combined with suitable patterning techniques, it is possible to fabricate SQUIDs with artificially created grain boundary junctions as active elements. We have demonstrated that the I-V characteristics of the SQUIDs are in accordance with the RSJ model with an R_nI_0 product of up to 140 μV at 4.2 K. The SQUIDs exhibit critical current modulations for temperatures up to 80 K. At 77 K the peak-to-peak value of the voltage modulation is 0.5 μV. Next, we have shown that when the SQUIDs are operated in the flux locked loop they exhibit large amounts of 1/f noise ($S_\phi = 1.7 \times 10^{-4}\ \phi_0/Hz^{1/2}$ at 10 Hz and 4.2 K). The noise can be reduced by a factor of 3 by employing the double modulation technique, indicating that the dominant contribution to the 1/f noise comes from critical current fluctuations. In an attempt to improve the noise properties we have subsequently developed a process for the fabrication of bi-epitaxial SQUIDs on YSZ substrates. We have shown how PBCO can be used as an intermediate buffer layer between the CeO_2 primary buffer layer and $SrTiO_3$, resulting in a process with seven epitaxial layers. After the process has been optimized we can fabricate SQUIDs that exhibit critical current modulation at 77 K, with a resulting peak-to-peak voltage of up to 0.85 μV at this temperature. Unfortunately, the noise properties for these SQUIDs are not better than those for the SQUIDs on MgO. Finally, we have developed a process for the fabrication of an integrated magnetometer on MgO substrates. Initially, it is shown how the flux transformer process can be developed by fabricating interconnect samples consisting of a YBCO base layer, an insulating layer with two windows, and a second YBCO layer. We have succeeded in fabricating an interconnect using CeO_2 (which has a low dielectric constant) as the insulating material. However, the yield of this process is found to be too low for practical purposes. In the actual magnetometer devices we have used $SrTiO_3$ instead, since this material results in a more reliable process. We have obtained critical current modulations at temperatures up to 73 K in these devices. At 67 K we have

measured a peak-to-peak value of 0.35 μV for the voltage modulation. The effective area of these devices is about 50 times larger than that of a bare SQUID, resulting in an enhancement of the sensitivity for magnetic flux density by the same factor.

In future work aiming at the fabrication of useful devices, the noise properties of the bi-epitaxial SQUIDs should be improved. In the devices described here, the 1/f noise is dominated by critical current fluctuations. We believe these fluctuations are related to the fact that the angle of the grain boundary is 45°, resulting in an inhomogeneous interface with a high density of dislocations. If the angle of the grain boundary could be made smaller, it would presumably be possible to obtain a more homogeneous interface with a reduction of the critical current fluctuations as a consequence. A bi-epitaxial process resulting in grain boundary angles other than 45° would require a search for a new set of materials with specific relations between the lattice parameters. For instance, if an orthorhombic material with a ratio between the a- and b-axes of 1:2 could be made to grow c-axis oriented with its [110] direction parallel to the [100] direction in a cubic or tetragonal material, the possibility to create grain boundaries with an angle of Arctan (½) = 26.5° would open up, provided that the YBCO grows epitaxially on these two materials.

Also, the issue of the flux noise in the films needs to be addressed. As we have seen, the flux noise in YBCO films grown on YSZ substrates with CeO_2, PBCO and $SrTiO_3$ buffer layers is not smaller than in films grown on MgO substrates with a $SrTiO_3$ buffer layer. Since the phenomema of flux pinning and flux motion is not fully understood at present in the high T_c materials, a trial and error approach is necessary at this point. Consequently, a measurement of the flux noise in films grown on potentially useful substrate and buffer layer combinations will give useful information about the noise properties of SQUIDs based on this particular combination of materials.

References

[1] B.D. Josephson. Phys. Lett. **1** (1962), 251.

[2] P.W. Anderson and J.M. Rowell. Phys. Rev. Lett. **10** (1963), 230.

[3] J.M. Rowell, M. Gurvitch and J. Geerk. Phys. Rev B **24** (1981), 2278.

[4] M. Gurvitch, M.A. Washington and H.A. Huggins. Appl. Phys. Lett. **42** (1983), 472.

[5] H. Hayakawa. In: *Superconducting Electronics*, NATO ASI Series F, ed: H. Weinstock and M. Nisenoff (Springer Verlag, Berlin, 1989).

[6] A. Barone and G. Paterno: "Physics and applications of the Josephson effect", (Wiley, New York, 1982).

[7] W.C. Stewart. Appl. Phys. Lett. **12** (1968), 277.

[8] D.E. McCumber. J. Appl. Phys. **39** (1968), 3113.

[9] T. Van Duzer and C.W. Turner: "Principles of superconductive devices and circuits", (Elsevier North Holland, New York, 1981).

[10] F. London: "Superfluids", (Wiley, New York, 1950).

[11] R.C. Jaclevic, J. Lambe, A.H. Silver and J.E. Mercereau. Phys. Rev. Lett. **12** (1964), 159.

[12] V. Ambegaokar and B.I. Halperin. Phys. Rev. Lett. **22** (1969), 1364.

[13] J. Clarke and R.H. Koch. Science **242**, (1988), 217.

[14] C.D. Tesche and J. Clarke. J. Low Temp. Phys., **27** (1977), 301.

[15] R.H. Koch, J. Clarke, W.M. Goubau, J.M. Martinis, C.M. Pegrum and D.J. van Harlingen. J. Low Temp. Phys. **51** (1983), 207.

[16] C.T. Roger and R.A. Buhrman. Phys. Rev. Lett. **53** (1984), 1272.

[17] P. Dutta and P.M. Horn. Rev. Mod. Phys. **53** (1981), 497.

[18] R.H. Koch, W. Eidelloth, B. Oh, R.P. Robertazzi, S.A. Amdrek and W.J. Gallagher. Appl. Phys. Lett. **60**, (1992) 507.

[19] A.H. Miklich, J. Clarke, M.S. Colclough and K. Char. Appl. Phys. Lett. **60**, (1992) 1899.

[20] G.A. Samara. J. Appl. Phys. **68**, (1990) 4214.

[21] R.H. Koch, C.P. Umbach, G.J. Clark, P. Chaudari and R.B. Laibowitz. Appl. Phys. Lett. **51**, (1987) 200.

[22] T.K. Worthington, W.J. Gallagher and T.R. Dinger. Phys. Rev. Lett. **59**, (1987) 1160.

[23] B. Oh, K. Char, A.D. Kent, M. Naito, M.R. Beasley, T.H. Geballe, R.H. Hammond and A. Kapitulnik. Phys. Rev. B **37**, (1988) 7861.

[24] G. Koren, E. Aharoni, E. Polturak and D. Cohen. Appl. Phys. Lett. **58**, (1991) 634.

[25] G. Koren, E. Polturak, E. Aharoni and D. Cohen. Appl. Phys. Lett. **59** (1991), 2745.

[26] J. Gao, W.A.M. Aarnink, G.J. Gerritsma and H. Rogalla. Physica C **171**, (1990) 126.

[27] J. Gao, Yu. Boguslavskij, B.B.G. Klopman, D. Terpstra, G.J. Gerritsma and H. Rogalla. Appl. Phys. Lett. **59**, (1991) 2754.

[28] B.D. Hunt, M.C. Foote and L.J. Bajuk. Appl. Phys. Lett. **59**, (1991) 982.

[29] D. Dimos, P. Chaudari, J. Mannhart and F.K. LeGoues. Phys. Rev. Lett. **61**, (1988) 219.

[30] D. Dimos, P. Chaudari and J. Mannhart. Phys. Rev. B **41**, (1990) 4038.

[31] R. Gross, P. Chaudari, M. Kawasaki, M.B. Ketchen and A. Gupta. Appl. Phys. Lett. **57**, (1990) 727.

[32] M. Kawasaki, P. Chaudari, T.H. Newman and A. Gupta. Appl. Phys. Lett. **58**, (1991) 2555.

[33] Z.G. Ivanov, P.Å. Nilsson, D. Winkler, J.A. Alarco, T. Claeson, E.A. Stefantsov and A.Ya. Tzalenchuk. Appl. Phys. Lett. **59**, (1991) 3030.

[34] Z.G. Ivanov, P.Å. Nilsson, D. Winkler, J.A. Alarco, G. Brorson, T. Claeson, E.A. Stefantsov and A.Ya. Tzalenchuk. Supercond. Sci. Technol. **4**, (1991) 439.

[35] S.M. Garrison, N. Newman, B.F. Cole, K. Char and R.W. Barton. Appl. Phys. Lett. **58**, (1991) 2168.

[36] K. Char, M.S. Colclough, S.M. Garrison, N. Newman and G. Zaharchuk. Appl. Phys. Lett. **59**, (1991) 733.

[37] K. Char, M.S. Colclough, L.P. Lee and G. Zaharchuk. Appl. Phys. Lett. **59**, (1991) 2177.

[38] X.D. Wu, R.C. Dye, R.E. Muenchausen, S.R. Foltyn, M. Maley, A.D. Rollett, A.R. Garcia and N.S. Nogar. Appl. Phys. Lett. **58**, (1991) 2165.

[39] J.J. Kingston, F.C. Wellstood, P. Lerch, A.H. Miklich and J. Clarke. Appl. Phys. Lett. **56**, (1990) 189.

[40] D.K. Fork, F.A. Ponce, J.C. Tramontana and T.H. Geballe. Appl. Phys. Lett. **58**, (1991) 2294.

[41] J.M. Jaycox and M.B. Ketchen. IEEE Trans. Mag, MAG-17 (1981), 400.

[42] G.E. Blonder and M. Tinkham. Phys. Rev. B, **27** (1983), 112.

[43] M. Kawasaki, P. Chaudari and A. Gupta. Phys. Rev. Lett., **68** (1992) 1065.

[44] M.B. Ketchen and R.F. Voss. Appl. Phys. Lett., **35** (1979), 812.

[45] T. Shaw. Private communication.

[46] G.L Romani. In: *Superconducting electronics*, NATO ASI Series F, ed: H. Weinstock and M. Nisenoff (Springer Verlag, Berlin, 1989).

[47] M.B. Ketchen. IEEE Trans. Mag., MAG-17 (1981), 387.

[48] A.H. Miklich, J.J. Kingston, F.C. Wellstood, J. Clarke, M.S. Colclough, K. Char and G. Zaharchuk. Appl. Phys. Lett., **59** (1991), 988.

[49] G. Friedl, B.Roas, M. Römheld, L. Schultz and W. Jutzi. Appl. Phys.Lett., **59** (1991), 2751.

4 Acknowledgements

It is impossible to carry out a project like this without the help of a large number of people. At this point I would like to express my appreciation for the assistance these people have provided over the last 3 years.
First and foremost I would like to thank my supervisors Niels Hessel Andersen at Risø National Laboratory and Jørn Bindslev Hansen at the Technical University of Denmark for their guidance and for sharing their knowledge and experience in experimental solid state physics. Also thanks to Claus Schelde Jacobsen for stepping in as supervisor at the Technical University during Jørn Bindslev Hansens leave of absence.
During my time at Risø my closest collaborator has been Roger de Reus and I would like to thank him for his participation in the work on sputter deposition and structural characterization. Also, his never failing enthusiasm for Genplot, which eventually converted me to his point of view, is much appreciated, as can be seen in several places throughout this report.
The thin film deposition work by RF sputtering would not have been possible without the skilled technical assistance of Werner Kofod, who designed and built the inverted cylindrical magnetron gun and the heated substrate table. I would also like to thank his staff of laboratory apprentices, Jens Schoustrup Thomsen, Helle Ottosen, Tina Jensen and Tenna Larsen for manufacturing the sputter targets and for assisting with the characterization of the sputtered films by X-ray diffraction. After Werner Kofod retired Arne Nordskov kindly stepped in and helped install the sputter system at the Physics Department after it was moved from the Materials Department.
I would like to thank Per Vase and Torsten Freltoft at NKT Research Center for providing the samples for the work on the structural characterization and also for passing along useful information at various stages in the project. During my time in the X-ray basement at Risø I have benefitted from discussions with Mourits Nielsen about X-ray diffraction. Steen Bang and Torben Kjær were always at hand whenever there was a problem with the spectrometer. Also Keld Theodor helped me with various odd jobs; in particular, I would like to thank him for producing figure 2.4. The TEM pictures in Chapter 2 were provided by Jørgen Bilde-Sørensen at the Materials Department after the samples were prepared for the TEM by Jørgen Lindbo. Their contribution is much appreciated.
The device work was carried out at the Physics Department of the University of California at Berkeley under the supervision of Professor John Clarke, and I would like to express my gratitude for his hospitality during my 13 months stay at his lab. During this time I had the pleasure of working with Jack Kingston, who taught me everything I know about laser ablation (almost) and Andy Miklich, who shared his insight into noise measurements on SQUIDs. Also the assistance from Lise Sagdahl, who helped characterize the devices by measuring the I-V and V-ϕ characteristics, is appreciated. Many other members of the Clarke group, although not directly involved in high T_c SQUID work, have provided useful information and contributed to the recollection of my

time at UC Berkeley as an enjoyable one. The assistance of George Weber in the machine shop with various practical problems regarding the laser deposition system is much appreciated. Also thanks to Tom Peterson, who did a very good job of building the target holder from a set of not exactly flawless drawings. A significant part of my work at UC Berkeley was carried out outside the Physics Department. I would like to thank the staff at the Microfabrication Laboratory in Cory Hall for operating the lab in a very efficient manner. All of us, not least the users, benefit from that. I would also like to thank Professor Hans-Rudolph Wenk at the Department of Geology for giving me almost unlimited access to the four-circle X-ray spectrometers in his lab. Without it, it would not have been possible to develop any bi-epitaxial process. After my return from Berkeley it became apparent that a noise measurement of one of the SQUIDs on YSZ substrates would be very informative. I thank Anders Kühle at the Technical University of Denmark for doing this at a very short notice.

The assistance of the secretaries Lajla Frederiksen and Margit Kloster at Risø and Barbara Salisbury at UC Berkeley in various administrative matters is much appreciated. Also the financial support from the Danish Ministry of Energy, the Materials Development Program for High T_c Superconductivity and from the Danish Research Academy (in connection with my stay in Berkeley) is gratefully acknowledged.

Finally, I would like to thank my family for their support. Especially my girlfriend, Helle Ottosen, deserves honorable mention for accepting my long working hours in general and during the preparation of this thesis in particular. I am sure she looks forward to the completion of this work just as much as I do.

Bibliographic Data Sheet **Risø-R-642(EN)**

Title and author(s)

Deposition, Characterization, and Electronic Applications of $YBa_2Cu_3O_7$ Thin Films

Rasmus Kromann

ISBN	ISSN
87-550-1827-0	0106-2840

Dept. or group	Date
Department of Solid State Physics	September 1992

Groups own reg. number(s)	Project/contract No(s)
	EM-1443/88-8 ENS-1443/90-0006

Pages	Tables	Illustrations	References
102	8	58	97

Abstract (Max. 2000 characters)

$YBa_2Cu_3O_7$ thin films were deposited by rf sputtering and laser ablation. In the case of rf sputtering the presence of negative oxygen ions was found to give rise to severe re-sputtering effects. Various ways of overcoming this problem are described. In contrast, laser ablation is found to be a much simpler and more reliable deposition method. Structural characterization in the form of an X-ray diffraction study of the structure of laser ablated YBCO thin films is reported. Two films on MgO differing by 75% in the critical current density were examined. The difference was ascribed to the fact that about 5% of the grains in the low J_c film grow 45° misoriented with respect to the dominant orientation in the a-b plane. Two other films on $SrTiO_3$ differing by 70% in J_c were examined. The difference was ascribed to the presence of 8.3% a-axis oriented material in the low J_c film as compared to only 0.6% in the high J_c film. Various ways of achieving a 45° grain boundary by a bi-epitaxial process on MgO substrates are described. A detailed account of the optimization of the deposition of the chosen sequence of thin film layers is given. The grain boundary junctions are used to fabricate DC SQUIDs. It is demonstrated that the SQUIDs exhibit critical current modulation in a magnetic field at temperatures up to 80 K. It is shown that the 1/f noise can be reduced by a factor of 3 by the double modulation technique, indicating that the dominant contribution to the 1/f noise comes from critical current fluctuations. The high level of 1/f noise from critical current fluctuations is ascribed to the nature of the 45° grain boundary and it is argued that it is necessary to develop a bi-epitaxial process for grain boundaries with angles less than 45°. Finally, it is demonstrated that a SQUID and a flux transformer can be fabricated on the same substrate to form an integrated magnetometer.

Descriptors INIS/EDB

ABLATION; BARIUM OXIDES; COPPER OXIDES; CRITICAL CURRENT; DEPOSITION; EPITAXY; GRAIN BOUNDARIES; GRAIN ORIENTATION; HIGH-TC SUPERCONDUCTORS; LASERS; MAGNETOMETERS; RF SYSTEMS; SPUTTERING; SQUID DEVICES; THIN FILMS; YTTRIUM OXIDES; X-RAY DIFFRACTION

Available on request from Risø Library, Risø National Laboratory, (Risø Bibliotek, Forskningscenter Risø), P.O. Box 49, DK-4000 Roskilde, Denmark.
Telephone +45 42 37 12 12, ext. 2268/2269
Telex 43 116. Telefax +45 42 36 06 09.

Available on request from:
Risø Library
Risø National Laboratory,
P.O. Box 49, DK-4000 Roskilde, Denmark
Phone +45 42 37 12 12, ext. 2268/2269
Telex 43116, Telefax +45 46 75 56 27

ISBN 87-550-1827-0
ISSN 0106-2840